

Theoretical and Numerical Analysis of a Novel Electrically Small and Directive Antenna

A Thesis Submitted to the Faculty of the
WORCESTER POLYTECHNIC INSTITUTE
in partial fulfillment of the requirements for the

Degree of Master of Science

in

Electrical and Computer Engineering

By:

Jeffrey Elloian

January 2014

APPROVED:

Dr. Sergey Makarov, Major Advisor

Dr. Ara Nazarian, Committee Member

Dr. Vishwanath Iyer, Committee Member

Dr. Yehia Massoud, Head of Department

ABSTRACT

Small antennas have attracted significant attention due to their prolific use in consumer electronics. Such antennas are highly desirable in the healthcare industry for imaging and implants. However, most small antennas are not highly directive and are detuned when in the presence of a dielectric. The human body can be compared to a series of lossy dielectric media.

A novel antenna design, the orthogonal coil, is proposed to counter both of these shortcomings. As loop antennas radiate primarily in the magnetic field, their far field pattern is less influenced by nearby lossy dielectrics. By exciting two orthogonal coil antennas in quadrature, their beams in the H-plane constructively add in one direction and cancel in the other. The result is a small, yet directive antenna, when placed near a dielectric interface.

In addition to present a review of the current literature relating to small antennas and dipoles near lossy interfaces, the far field of the orthogonal coil antenna is derived. The directivity is then plotted for various conditions to observe the effect of changing dielectric constants, separation from the interface, etc.

Numeric simulations were performed using both Finite Difference Time Domain (FDTD) in MATLAB and Finite Element Method (FEM) in Ansys HFSS using an anatomically accurate high-fidelity head mesh that was generated from the Visible Human Project[®] data. The following problem has been addressed: find the best radio-frequency path through the brain for a given receiver position – on the top of the sinus cavity. Two parameters: transmitter position and radiating frequency should be optimized simultaneously such that (i) the propagation path through the brain is the longest; and (ii) the received power is maximized. To solve this problem, we have performed a systematic and comprehensive study of the electromagnetic fields excited in the head by the aforementioned orthogonal dipoles. Similar analyses were performed using pulses to detect Alzheimer's disease, and on the femur to detect osteoporosis.

TABLE OF CONTENTS

Abstract.....	i
Table of Figures	iv
Table of Tables	vii
Introduction.....	1
A.) Problem Statement	1
B.) Small antennas	2
Literature Review.....	5
A.) Antenna selection.....	5
B.) Orthogonal Coil Antennas:	8
C.) Field Propagation	9
D.) Human Body Meshes	12
Material Properties.....	15
Orthogonal Coil Antennas: Theory.....	19
A.) An Antenna above a Dielectric Interface: Prevailing Theories	19
B.) Sommerfeld's Theory	22
C.) Banos' Theory.....	26
D.) Wait's Theory	28
E.) An Antenna above a Dielectric Interface: Angular Spectra.....	29
F.) Horizontally Oriented Magnetic Dipole	33
G.) Vertically Oriented Magnetic Dipole.....	34
H.) Special Cases	41
I.) Orthogonal Magnetic Dipoles.....	45
J.) Directivity	46
Arbitrary Orientation of Magnetic Dipoles.....	49
A.) Polarization	49
B.) Arbitrary Orientation of the Magnetic Dipoles.....	53
Orthogonal Coil Antennas: Analytical Results.....	55
A.) Directivity Patterns	55
B.) Parametric Analysis: Sensitivity to Changes in the Dielectric Constant	57
C.) Parametric Analysis: Sensitivity to Changes in the Conductivity	63
D.) Parametric Analysis: Sensitivity to Changes in Height	66
E.) Parametric Analysis: Sensitivity to Changes in Excitation Phase	71
Applications of the Orthogonal Coil Antenna	75
A.) Poynting Vector for the Sagittal Plane.....	77
B.) Establishing a Propagation Channel Through the Brain.....	83

C.) Validation Using Pulses and FDTD.....	88
D.) RF Simulations on a Human Femur Model: Preliminary Results.....	94
Frequency Selection.....	96
RX Array.....	100
Nominal Case.....	101
Increased Fat Dielectric Constant Case.....	104
Highly Conductive Muscle Case.....	106
Conclusion	108
A.) Human Body Results	108
B.) Future Extensions and Applications	109
References.....	111
Acknowledgements.....	116
Appendix A. Orthogonal Magnetic Dipoles in Free Space.....	117
A.) Vertical and Horizontal magnetic dipoles in free space.....	117
B.) Orthogonal Magnetic Dipoles in Free-Space.....	119
Appendix B. Mesh and Model Sensitivity	121
Appendix C. MATLAB Code for the Orthogonal Coil Radiation Pattern Graphical User Interface	126

TABLE OF FIGURES

Fig. 1. Arbitrary antenna enclosed in a Chu Sphere.....	4
Fig. 2. Problem geometry for two orthogonal coils with respect to the H plane. The coils were modeled as loops with equivalent magnetic moments m	6
Fig. 3. Analytical electric field pattern with respect to the H plane for two orthogonal coils close to the human head. The coils are excited 90° out of phase to null one beam (right) and to amplify the other (left).....	8
Fig. 4. Cross section of the sagittal (YZ) plane of the human head model. a.) Locations of included organs, b.) Examples of antenna locations with respect to θ . The phase of the excitation was adjusted such that the 45° beam transverses the head, as indicated.....	13
Fig. 5. Example of material properties provided by IT'IS with labeled dispersion regions	17
Fig. 6. Orientation of magnetic dipoles above a dielectric interface. a) the proposed orthogonal orientation b) arbitrary orientation	49
Fig. 7. Example of the Directivity Pattern of Two Orthogonal Magnetic Dipoles	56
Fig. 8. Analytical Maximum Directivity as a Function of ϵ	58
Fig. 9. Power Radiated into the Dielectric as a Function of ϵ	59
Fig. 10. Directivity Patterns for $\epsilon=1, 2$, and 5	61
Fig. 11. Directivity Patterns for $\epsilon=10, 20$, and 100	62
Fig. 12. Analytical Maximum Directivity as a Function of σ	63
Fig. 13. Power Radiated into the Dielectric Medium as a Function of σ	64
Fig. 14. Directivity Patterns for $\sigma=0, 0.25$, and 1	65
Fig. 15. Analytical Maximum Directivity as a Function of Height above the Interface	67
Fig. 16. Analytical Maximum Directivity as a Function of Height above the Interface for small distances	68
Fig. 17. Power Radiated into the Dielectric as a Function of Height above the Interface	69
Fig. 18. Directivity Patterns for $h=0, 0.01\lambda$, and 0.1λ	70
Fig. 19. Analytical Maximum Directivity as a Function of the Phase Offset	72
Fig. 20. Directivity Patterns for the Combined Cross Coil Antenna with Different Phase Shifts.....	73
Fig. 21. Close-up view of the two orthogonal loop antennas used in the following simulations. Only the skin, skull, CSF, and brain meshes are shown for clarity.....	76
Fig. 22. Section of the surface mesh used in Ansys HFSS simulations of the head. The blue spheres indicate possible TX positions, whereas the black sphere is the location of the receiver.	76
Fig. 23. Magnitude and direction of the Poynting vector for selected antenna positions at 100 MHz. The red crosses show the locations of the transmitter (the size is exaggerated for clarity).....	78

Fig. 24. Magnitude and direction of the Poynting vector for selected antenna positions at 500 MHz.	80
Fig. 25. Magnitude and direction of the Poynting vector for selected antenna positions at 1 GHz.	82
Fig. 26. a) Magnitude of the Poynting vector evaluated at the test point above the sinus cavity as shown in Fig. 27 for different excitation positions and frequencies. b) The length of the path of power propagation through the brain. The star indicates the selected optimal compromise in maximising the received power and propagation distance through the brain (at $\theta = +15^\circ$ and $f = 400 \text{ MHz}$).	85
Fig. 27. Magnitude and direction of the Poynting vector for an antenna placed at $\theta = +15^\circ$ at selected frequencies.....	87
Fig. 28. Combined low-resolution mesh for the Visible Human Body Project (female)	88
Fig. 29. Orthogonal-coil antenna used at the simulations: a) concept; b) Operation at the top of a lossy dielectric half-space, c) Magnetic field at the probe location in Fig. 1b.	89
Fig. 30. Evolution of the pulse signal (dominant co-polar electric-field component is shown) within the human head at 400MHz, 800MHz, and 1600MHz center frequency. Only the outer shape of the human head is shown.	92
Fig. 31. a) - Orthogonal-coil antenna on top of the head excited at 400MHz and two small orthogonal receiving dipoles (or field probes; b) - The copolar electric field at one receiver location (on the back of the head). The received voltage signal for a small.....	93
Fig. 32 Leg and hip from the Ansys Human Body Model.....	94
Fig. 33. Comparison of an a) osteoporotic femur and b) a normal femur	95
Fig. 34. Signal path through the leg for an 800 MHz excitation. a) the osteoporotic case and b) the normal femur	96
Fig. 35. Frequency dependence of the dielectric constant on selected tissues	97
Fig. 36. Percentage difference in Dielectric Constant between the Cancellous Bone and Yellow Bone Marrow	98
Fig. 37 Frequency dependence of the conductivity of selected tissues	99
Fig. 38. Percentage difference in Conductivity between the Cancellous Bone and Yellow Bone Marrow	100
Fig. 39. Transmitter and receiver array positions on the leg	101
Fig. 40 Simulated, Normalized RSS along the Femur for the Nominal Case	103
Fig. 41 Simulated, Normalized RSS along the Femur with an Increased Fat Dielectric Constant	105
Fig. 42 Simulated, Normalized RSS along the Femur with highly conductive muscle tissue	107
Fig. 43. Prototype orthogonal coil antennas. a) Power splitter connected to two cables offset by $\lambda/4$ b) Close-up view of the antenna	110

Fig. 44. Normalized magnitude of the simulated electric field along the surface of the head at a.)800MHz, b.) 1600MHz, and c.) 2400MHz.	121
Fig. 45. Locations of transmitting antennas and field measurement points. The receiver on the forehead is in the direct path of the surface wave. Conversely, the receiver on the tongue is mainly influenced by the volumetric wave.	124

TABLE OF TABLES

Table 1-Comparison of commercially available human body meshes	14
Table 2- Dispersion regions of biological tissue [57]	16
Table 3. Banos' results for the field components of a horizontal electric dipole above a conductive interface.....	27
Table 4. General reflection and transmission coefficients at a dielectric interface.....	31
Table 5. Components of the electric field for an arbitrary antenna above a dielectric interface in the far field.....	32
Table 6. General reflection and transmission coefficients at a dielectric interface in terms of K_{si}	32
Table 7. Far field of an infinitesimally small, horizontally oriented magnetic dipole above a dielectric interface.....	34
Table 8. Far field components for an arbitrary array of horizontal loops above a dielectric interface	35
Table 9. Far field components of a vertical magnetic dipole above a dielectric interface.....	37
Table 10. Fresnel coefficients with no boundaries.....	38
Table 11. Compact expression for the far-field of a horizontal magnetic dipole above a dielectric interface	40
Table 12. Compact expression for the far-field of a vertical magnetic dipole above a dielectric interface	41
Table 13. Far field components for a horizontal magnetic dipole very close to a dielectric interface.....	42
Table 14. Far field components for a Vertical magnetic dipole very close to a dielectric interface	42
Table 15. Far field components for a horizontal magnetic dipole very close to a high contrast dielectric interface.....	44
Table 16. Far field components for a Vertical magnetic dipole very close to a high contrast dielectric interface.....	45
Table 17. Field components for combined orthogonal dipoles with a 90 degree phase offset very close to a high contrast dielectric interface	46
Table 18. Vertical and horizontal components of two arbitrary magnetic moments	54
Table 19. Electrical data of biological tissues at 400 MHz, [41] used at the simulations as nominal values.	90
Table 20. Change in RSS between two femur models for selected CW frequencies.....	96
Table 21. Relevant Material Properties for the Nominal Femur.....	101
The majority of this femur from the Ansys body model consists primarily of fat. To be a useful medical diagnosis tool, this method would need to have little variation between the quantity and material properties of the fat layer (which could vary from patient to patient). Generating a new FEM mesh is very difficult, thus we instead elected to increase the dielectric constant of the fat layer by 10%. Note	

that all material properties are still frequency dependent, thus the ϵ_r of fat was increased across the entire frequency sweep, not a specific point. A sample of these frequencies is displayed in Table 22.

.....	104
Table 23. Relevant Material Properties for the Femur with an Increased Fat Dielectric Constant.....	104
Considering the high volume of muscle surrounding the femur, it is logical to examine the variation of its material properties on the received signal. The conductivity of the muscle tissue is raised to match its dielectric constant. Table 24 summarizes these new values in comparison to the other material properties at 400MHz.	106
Table 25. Relevant Material Properties for the Femur with Highly Conductive Muscles.....	106
Table 26. Electric and magnetic field components for a vertical magnetic dipole in free-space.....	118
Table 27- Electric and magnetic field components for a horizontal magnetic dipole in free-space	119
Table 28- Electric and magnetic field components for a horizontal magnetic dipole that is delayed by 90 degrees.....	120
Table 29- Electric and magnetic field components for two orthogonal magnetic dipoles in free-space ..	120
Table 30. Root mean square error of each fit of the E field.....	122
Table 31. Phase difference in the electric field in a given direction on the tongue with respect to changes in the dielectric constant of the brain.	123

INTRODUCTION

Electromagnetic imaging has become an important field in recent years. Although radar has been used to find objects since World War II, medical professionals are searching for noninvasive techniques to find tumors in the human body. As opposed to large HF arrays trying to find targets that are several meters across, we turn our attention to searching for small tumors or other abnormalities that are on the millimeter scale [1].

This project was inspired by our joint work with Beth Israel Deaconess Medical Center at Harvard Medical School. They perform several traditional and experimental imaging procedures such as electric impedance tomography (EIT), magnetic induction tomography (MIT), and microwave tomography (MWT). EIT operates at DC or low frequencies (DC-20Hz) by applying electrodes to the body and trying to restore the conductivity of each of the internal materials [2]. MIT uses higher frequencies (200kHz-10MHz) and excites eddy currents using magnetic fields in a similar manner as a traditional metal detector [3]. MWT uses RF frequencies (400MHz-10GHz) and senses reflections of a transmitted wave in a similar manner as RADAR [4], [5]. This paper focuses on MWT with a novel directional antenna.

A.) PROBLEM STATEMENT

We have established the need for a small, directional antenna that radiates into a nearby dielectric. If antenna is to be worn on the body, it must be small. Ideally, the antenna would be located on the surface of the skin as to avoid being invasive, yet minimizing the losses in the air between the antenna and the body. Furthermore, the human body is a lossy dielectric. Each tissue and organ has a different dielectric permittivity (ϵ_r) and conductivity (σ), both of which affect the radiation properties of the antenna. As will be discussed in later sections, surrounding an antenna with a dielectric can detune it. Moreover, dispersion from a poorly concentrated wave may render the signal unrecoverable.

This paper will focus on the design of a small, directional antenna from a theoretical standpoint. We consider existing designs and discuss their merits and shortcomings. A new antenna design, the

orthogonal coil antenna, is proposed and its far-field pattern is derived. With the theory established, a custom human body model is used to simulate the performance of the antenna on both the brain and femur.

No restrictions are placed on the exact size and position of the antenna, as these are problem dependent. We are only interested in finding a general antenna design that can create a directed beam, while still remaining electrically small, that is, the antenna should have no dimension greater than $\frac{\lambda}{2\pi}$, where λ is the wavelength [6]. One may scale dimensions with the desired wavelength, but the power loss from having a small antenna (and a low radiation resistance) is deemed to be irrelevant, as the antenna is outside the body and presumably from utility power (as opposed to a battery with limited life).

B.) SMALL ANTENNAS

One could argue that the consumer electronics industry has driven the market to search for smaller and smaller antennas to fit in more complicated portable devices. These include cell-phones, tablets, radio frequency identification devices (RFIDs), etc. The medical field is also interested in miniaturization, as they look for methods of powering and communicating with internal implants. Naturally, these have acted as a driving force to find small antennas.

Unfortunately, small antennas generally have a uniform radiation pattern, that is, they radiate in all directions equally [6]. A uniform radiation pattern would result in a very wide beam, and the antenna would be unable to focus at an area of interest (reducing resolution). Some small antennas can have directive properties when placed in a close proximity of a dielectric, such as the loop antenna [7], [8]. These cases are examined in more depth in the literature review.

Chu, McLean, and Wheeler pioneered the field of theoretical small antenna design. Antennas generally operate close to or at a fraction of their wavelength. For example, classical dipoles and monopoles resonate at $\frac{\lambda}{2}$ and $\frac{\lambda}{4}$, respectively. Below the resonance, the radiation resistance is very low, making impedance matching difficult (adding additional resistance will reduce reflections, but the resistor will absorb the power instead of the antenna) [1]. Chu and Mclean derived a lower limit for the quality

factor, Q , for any given antenna [6]. The quality factor is a unitless metric that indicates how well a resonator stores energy. It is given as:

$$Q = \frac{2\omega_0 \cdot \max(W_E, W_M)}{P_A} \approx \frac{1}{BW}, \quad (1)$$

where ω_0 is the resonant frequency, W_E and W_M are the energy stored in the electric and magnetic field, respectively, and P_A is the power accepted by the antenna. A high quality factor antenna releases most of its energy over a narrowband of frequencies, whereas an antenna with a lower Q will spread the same amount of energy over a wider bandwidth. The quality factor is then approximately the reciprocal of the 3dB bandwidth (the range of frequencies that at least half of the power is released) [6].

Let us assume we have an arbitrary antenna that is physically bound by a sphere with radius a , such that a is the maximum dimension of the antenna, as shown in Fig. 1 for a conical dipole. Wheeler explored the quality factor of an antenna by developing lumped circuit models. Chu and Harrington advanced this theory by approximating on the lower bound of Q , that is, the theoretical maximum bandwidth an antenna of a given size could possibly achieve. McLean then found the exact Chu Limit, which is lower bound for Q for small antennas [6]:

$$Q_{min} = \frac{1}{ka} + \frac{1}{(ka)^3}, \quad (2)$$

where k is the wavenumber ($\frac{2\pi}{\lambda}$).

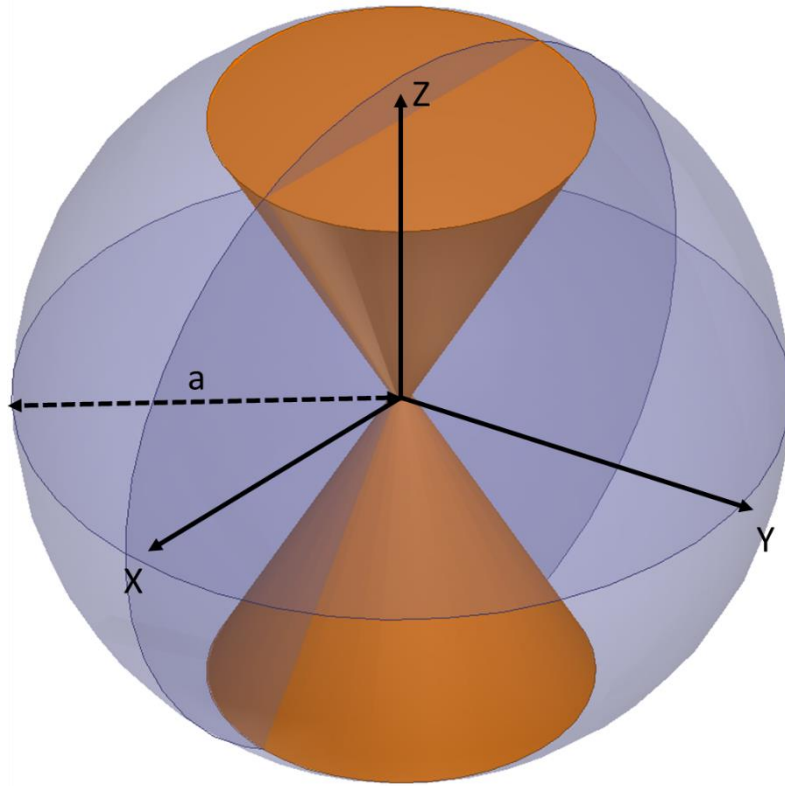


Fig. 1. Arbitrary antenna enclosed in a Chu Sphere

Hundreds of small antenna designs are currently used in industry. One of the most popular techniques to increase the electric length of an antenna is by building meandering lines. As opposed to etching a straight trace, one can lengthen the path of current with a “zigzag” pattern. This does not increase the maximum dimension of the antenna, but more efficiently uses the volume within the sphere [6]. One can also perform impedance matching by placing capacitive loading (i.e. a metal plate) on the top of an antenna, effectively widening its bandwidth at the cost of less uniform radiation characteristics. Antennas can also be surrounded by dielectrics, which decrease the effective wavelength, electrically lengthening the antenna. Unfortunately, dielectrics are generally lossy and will reduce the efficiency of the antenna.

LITERATURE REVIEW

In the past several years, there has been significant development in the field of wireless body area networks (BANs) with numerous applications involving sensing or transmission of data from different points around or through the body [9], [10]. Clearly, there are multiple health-care advantages to being able to obtain information around the body remotely without dangerous and expensive, invasive procedures. A notable application is reviewed in [11], as the potential for the early diagnosis of Alzheimer's disease through the detection of internal changes of material properties is discussed. These problems require a signal path through the brain [9].

As previously mentioned, the human body is a lossy transmission medium, which presents several challenges in itself. Prior to the introduction of powerful simulation tools, researches relied on theoretical derivations to guide experimentation. This is especially true for electromagnetic fields due to the difficulty involved in acquiring empirical results. Unfortunately, it is very difficult (and potentially dangerous) to perform experiments directly on the human body, thus it is important to develop accurate theoretical models to guide and prove the validity of simulations before conducting tests.

A.) ANTENNA SELECTION

The selection of antenna for the purpose of investigating propagation channels within the human body is not a trivial task. If one were to select a traditional dipole, the multipath caused by the boundaries between organs would cause the (initially uniform, omnidirectional) dispersed wave to be completely untraceable at the receiver, limiting the information that can be gathered about the channel. Furthermore, a dipole primarily radiates in the electric field, which is significantly affected by the permittivity of the human body. Although this can be mitigated by selecting a magnetic dipole or a loop, one would still need to find a way to "steer" the beam to a receiver on the head, providing information about a single, desired path.

There are several possible designs for "wearable" antennas (which typically are members of the patch family, as these can be made very conformal), but this project requires the antenna to be able to

transmit through the body. The objective of most wearable antennas is to transmit to a base station away from the body.

Selection of an antenna for the purpose of investigating propagation channels within the human body is not a trivial task. If one were to select a traditional dipole, the multipath caused by the boundaries between organs would cause the dispersed wave to be completely untraceable at the receiver, limiting the information that can be gathered about the channel. Furthermore, a dipole primarily radiates in the electric field, which is significantly affected by the permittivity of the human body. Although this can be mitigated by selecting a magnetic dipole or a loop, one would still need to find a way to “steer” the beam to a receiver on the head, providing information about a single, desired path.

There are several possible designs for wearable antennas, which typically are members of the patch family, as these can be made conformal [12]. The objective of most wearable antennas is to transmit to a base station away from the body [12], [13]. Conversely, this project requires the antenna to be able to transmit through the body.

The loop is a very simple option for selecting an antenna that can propagate through the body. A small loop or coil is very similar to a small dipole; however, it is horizontally polarized as opposed to vertically polarized [1]. This implies that a dipole would be radiating in E_θ , whereas a loop is radiating in H_θ . Fig. 2

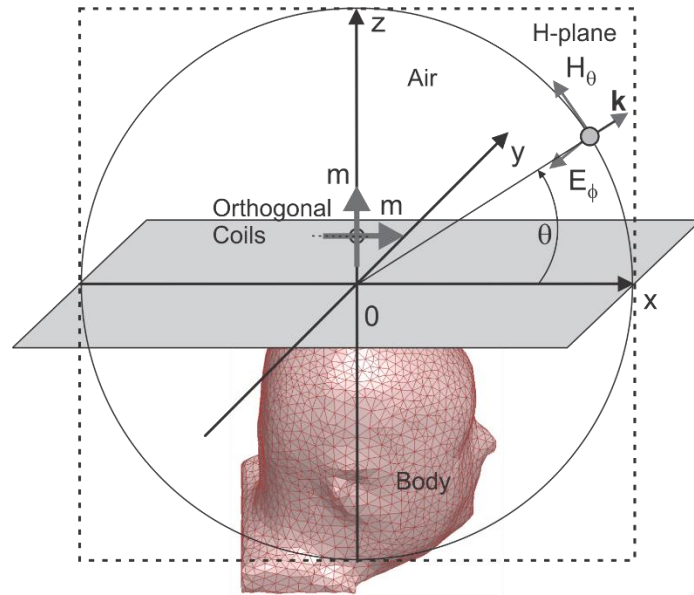


Fig. 2. Problem geometry for two orthogonal coils with respect to the H plane. The coils were modeled as loops with equivalent magnetic moments m .

illustrates the orientation of the H_θ with respect to two orthogonal coils (described in the following section). Therefore, the loop antenna should be less affected by dielectric loading. Unfortunately, the radiation pattern remains nearly the same as a dipole, thus it can be difficult to properly distinguish the

angle of arrival for internal channels [1]. Several examples of electric dipoles in various configurations can be found in [14], [15], [16], and [17]

Of course, there is substantial literature available regarding a dipole (either electric or magnetic) above a dielectric medium. Lindell presents a series of derivations in [18], [19], and [20], for the vertical case. Lukosz and Kunz perform a similar analysis on orthogonal electric dipoles using optics in [21] and [22].

An interesting variation of the classic loop is presented in [23]. The authors created segmented loop antennas to generate a uniform current distribution throughout the length of the antenna. Without segmentation (and the addition of the corresponding matching capacitance), there were regions with large specific absorption rate (SAR) values. Once these so called “hot-spots” appear, one must reduce the transmit power in order to avoid possible tissue damage [23]. This was of particular interest because the goal of the study was to improve the efficiency of the coupling that would power an implant.

Another variation is the fat arm spiral antenna, designed as means of wirelessly streaming images from an endoscopic capsule to a technician in real time, while providing more bandwidth (from 460 MHz to 535 MHz) than traditional spiral or helix antennas. This additional bandwidth was provided by thickening the spiral. The antenna produces an omnidirectional radiation pattern vital to the particular case study, as the orientation of the capsule in the digestive tract relative to a fixed receiver is arbitrary [24].

A more complex approach is offered by Karathanasis and Karanasiou, who have developed a phased array based reflector system to do beamforming within the human body. As opposed to a single radiating element, this system employs a 1.25m by 1.2m ellipsoidal cavity and changes the excitation phase to cause a local maximum in a given area, capable of inducing localized brain hyperthermia or treating hypothermia [25]. Additional references on antennas located near dielectric interfaces can be found in: [26], [27], [28], [29], [30], [31], [32], [33], [34], [35], [36], [37], and [38].

B.) ORTHOGONAL COIL ANTENNAS:

A possible solution to this problem was proposed in [11], where two orthogonal coil antennas were excited with a 90° phase difference to produce a single concentrated beam at 45° , without the need for a large or complicated array. This configuration, shown in Fig. 3, provides a maximum directivity of more than 10dB, allowing one to use less transmitted power, while reducing interference caused by undesired reflections.

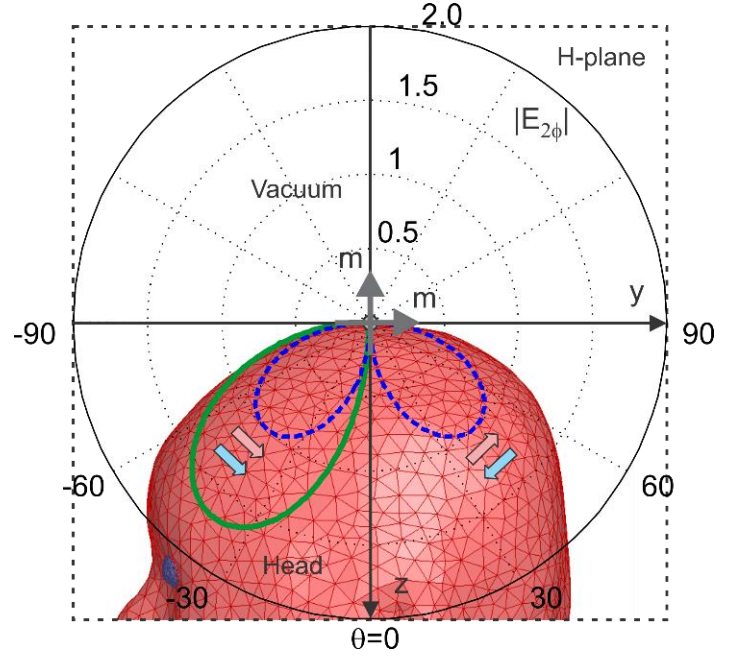


Fig. 3. Analytical electric field pattern with respect to the H plane for two orthogonal coils close to the human head. The coils are excited 90° out of phase to null one beam (right) and to amplify the other (left).

This special beamforming property only holds true when the loops are close to an air-dielectric interface that satisfies the quasi-static limit of $\sigma > \varepsilon\omega$ [39]. It is possible for a loop or dipole to generate a directive beam under the condition that the ratio of permittivities of the transmission media is large (greater than 4). With ε_r of air being 1 and ε_r of body tissues being on the order of 17-70, this is clearly applicable [40], [41]. Under this condition, and provided that the loops are excited close to the dielectric interface (i.e., the surface of the human body), the electric fields in the second medium (the body) in the H-plane (for horizontal and vertical loops respectively) reduce to [39]:

$$E_{1x} = j\omega\mu_0 k_1 n m \left\{ \frac{|\sin(2\theta)|}{|\cos(\theta)| + j|\sin(\theta)|} \right\} \quad (1)$$

$$E_{2x} = \omega\mu_0 k_1 n m \left\{ \frac{\text{sign}(y)|\sin(2\theta)|}{|\cos(\theta)| + j|\sin(\theta)|} \right\} \quad (2)$$

where k_1 is the wavenumber through medium 1, $n = \sqrt{\epsilon_2/\epsilon_1}$ is the refractive index, y is the distance along the dielectric interface, and m is the magnetic dipole moment. These predict two main lobes for each dipole, centered at $\theta = 45^\circ$, and $\phi = \pm 90^\circ$ (the H-plane) [39]. By exciting the orthogonal coils 90° out of phase, it is possible to cause destructive interference in one lobe and constructive interference in the other, as seen in Fig. 3. The small size and highly directive pattern of this antenna make it an excellent candidate for this study.

C.) FIELD PROPAGATION

Electromagnetic field propagation is a classical topic for which the theory is well developed. In the general sense, fields propagate from a source in a manner that satisfies the Maxwell equations and appropriate boundary conditions. The latter part provides interesting affects as a wave comes in contact with different media, sometimes giving rise to different modes.

The most basic case of a time-varying harmonic field is the concept of the plane-wave. As seen in any classical electromagnetic textbook, this is a valid approximation of a propagating field as long as one is significantly far enough from the antenna, such that the wave front appears to be uniform. These can then be characterized by a wavenumber, k , and the wave equations [42]:

$$\nabla^2 \tilde{E} - \gamma^2 \tilde{E} = 0 \quad (3)$$

$$\nabla^2 \tilde{H} - \gamma^2 \tilde{H} = 0, \quad (4)$$

where \tilde{E} , and \tilde{H} , are the electric and magnetic vector phasors (respectively), and γ is the propagation constant. Note that this plane wave does not necessarily need to be uniform across the entire wave front. Indeed, the wavenumber can be a complex value, which is vital for the definition of the surface wave, as we can define a transverse wave impedance as seen in [43].

However, waves often come into contact with different media, and the appropriate boundary conditions must be respected. This is a classic field that it is closely tied with optics via Snel's law, which clearly can be applied in these cases. This then gives rise to different types of modes. The most fundamental is the transverse electromagnetic mode (TEM), but waveguides operate on the principle of

transverse electric (TE), or transverse magnetic (TM) modes depending whether the electric or the magnetic field is perpendicular to the interface between the materials [42].

One of the first investigators in the field was Sommerfeld, who analytically characterized surface waves along a cylindrical wire. This showed both the skin effect (with regards to the concentration of current within the wire) as well as the elliptical polarization of the electric field in the direction of propagation [44]. Less than a decade later, Zenneck introduced his controversial explanation of the surface waves observed in Sommerfeld's result [45]. Traditionally, it is accepted that radiation decays proportional to $\frac{1}{r}$ in the far field; however, Zenneck believed radios could transmit further by propagating through the ground via a so-called "Zenneck wave," which decays at a slower rate of $\frac{1}{\sqrt{r}}$. Although it was later determined that the ionosphere was acting as a reflector, permitting the transmission of electromagnetic waves over long distance, the existence of the Zenneck wave has been a topic of debate [46].

The human body may be modeled as a planar set of layered, homogenous boundaries with the appropriate permittivities and conductivities [47]. By using a spatial transmission line propagation model, the transverse wave impedance of the i^{th} boundary in the x direction can be expressed by [43]:

$$Z_i = \frac{k_{x,i}}{\left(\frac{\omega\epsilon_i - j\sigma_i}{\epsilon_0}\right)k_0}, (TM) \quad (5)$$

$$Z_i = \frac{\omega\mu_0}{k_{x,i}}, (TE) \quad (6)$$

In general, the input impedance (from the perspective of the boundary) must cancel to produce a surface wave on that boundary [43], [47]. The major two types of surface waves that are discussed are the Norton wave and the Zenneck wave. Although an approximation intended for engineering purposes, the Norton wave equations describe the rate of decay [46]. It is effectively the geometrical optics field subtracted from the radiating field. Assuming medium 2 is air, The Norton wave is given by [48]

$$E_{2z}^s(p, 0) = \frac{j\omega\mu_0}{2\pi} \left(\frac{e^{jk_2 p}}{p} \right) F_e \quad (7)$$

$$F_e = 1 + j\sqrt{\pi p}e^{-p}[1 - \text{erf}(j\sqrt{p})] \quad (8)$$

Note that p is the so-called “numeric distance,” is given by $p = jk_2\rho\left(\frac{k_2^2}{2k_1^2}\right)$. Norton provides tables of F_e for various values of p in [49]. It is important to note that the rate of decay is approximately e^{-p} , similar to the traditional far-field results, but the wave will be coupled to the surface as opposed to radiating into space.

On the other hand, the Zenneck wave can be expressed along the length of a boundary (again, medium 1 is the dielectric and medium 2 is air) as [48]:

$$E_{1z} = \frac{j\omega\mu_0 k_2}{k_1^2} A e^{jk_1 z} H_0^{(1)}(k_2 \rho) \quad (9)$$

$$E_{2z} = \frac{j\omega\mu_0}{k_2} A e^{j\left(\frac{k_2^2}{k_1}\right)z} H_0^{(1)}(k_2 \rho), \quad (10)$$

where $H_0^{(1)}$ are Hankel functions, which can be approximated by [48]:

$$H_0^{(1)}(k_2 \rho) \approx \sqrt{\frac{2}{\pi k_2 \rho}} e^{j\left(k_2 \rho - \frac{\pi}{4}\right)} \quad (11)$$

The most important part to note in this result is that the Zenneck decays at a much slower rate of $\frac{1}{\sqrt{r}}$; however, the appropriate material parameters of the boundary must be selected for a Zenneck wave solution to exist. A more detailed discussion on these waves can be found in [48] and [46].

Based on the transverse impedances simulated by Lea in [43], it is unlikely that a Zenneck wave can be excited on the body with a short electric dipole. Considering that the body model used in [43] is inductive at lower frequencies, the conditions for the Norton or Zenneck surface waves could not be met, thus no TE surface waves could be observed below 5 GHz. Conversely, the fundamental TM mode produced surface waves, as the component of the electric field that is perpendicular to the surface is less affected by dielectric losses (severely attenuating any TE waves). Similarly, the presence of Norton waves was confirmed via simulation [43].

D.)HUMAN BODY MESHES

In recent years, significant interest has been placed in the development of accurate human body meshes. Although it is easier to develop an analytical model for planar interfaces, such as the one seen in [43], the accuracy of such models is limited. The human body is far from a simple planar interface and the relatively high conductivity and permittivity of the lossy organs has a profound effect on the transmission characteristics [11]. Once one refines a model to include internal organs (which is clearly even more difficult than a non-planar homogeneous medium), it is impractical to develop a full analytical model.

Fortunately, computational advances over the past several decades have resulted in detailed and reliable electromagnetic solution techniques such as finite difference time domain (FDTD), method of moments (MoM), and finite element analysis (FEM). In order to use these powerful tools for medical analysis, one requires a mesh of the test subject. A mesh is a series points that connect triangles and tetrahedral to form a three-dimensional structure that closely approximates the object of question. As one would expect, the finer the resolution of the mesh (ie. the more triangles used to approximate it), the larger the mesh, and the longer the computation time. With accurate, computationally feasible meshes of the human body, it would be possible to run a variety of EM simulations to advance science and medicine (minimizing the number of dangerous tests that need to be done to live subjects). Table 1 presents a list of human body models that are commercially available.

Custom meshes were constructed for this project from the raw cryoslice data provided by the Visible Human Body Project® [50]. The images were produced by photographing slices of the axial plane of a female subject at a resolution of 2048×1216 pixels, with each pixel having an area of 0.33mm^2 .

Organs, including the brain, skull, jaw, tongue, and spine, were identified in pertinent cryoslices and hand-segmented using ITK-Snap [51], meshed, and imported into MATLAB. This time-consuming process described in [11] results in large, fine resolution triangular surface meshes. Each of these was further simplified using surface-preserving Laplacian smoothing [52] to enable fast, yet accurate simulations. Resulting models have 1,000-12,000 triangles per structure and mesh description via the

NASTRAN file format [53], [54] allows users to import into custom and commercial simulation software packages. In this way, all meshes were imported into Ansys' High Frequency Structural Simulator (HFSS) v. 14, a commercially available FEM electromagnetic simulation suite, and the mesh checking tools resident in this package were utilized to check each model for manifoldness, intersection, and other relevant properties.

Creation of the Cerebrospinal Fluid (CSF), a highly conductive liquid that entirely encompasses

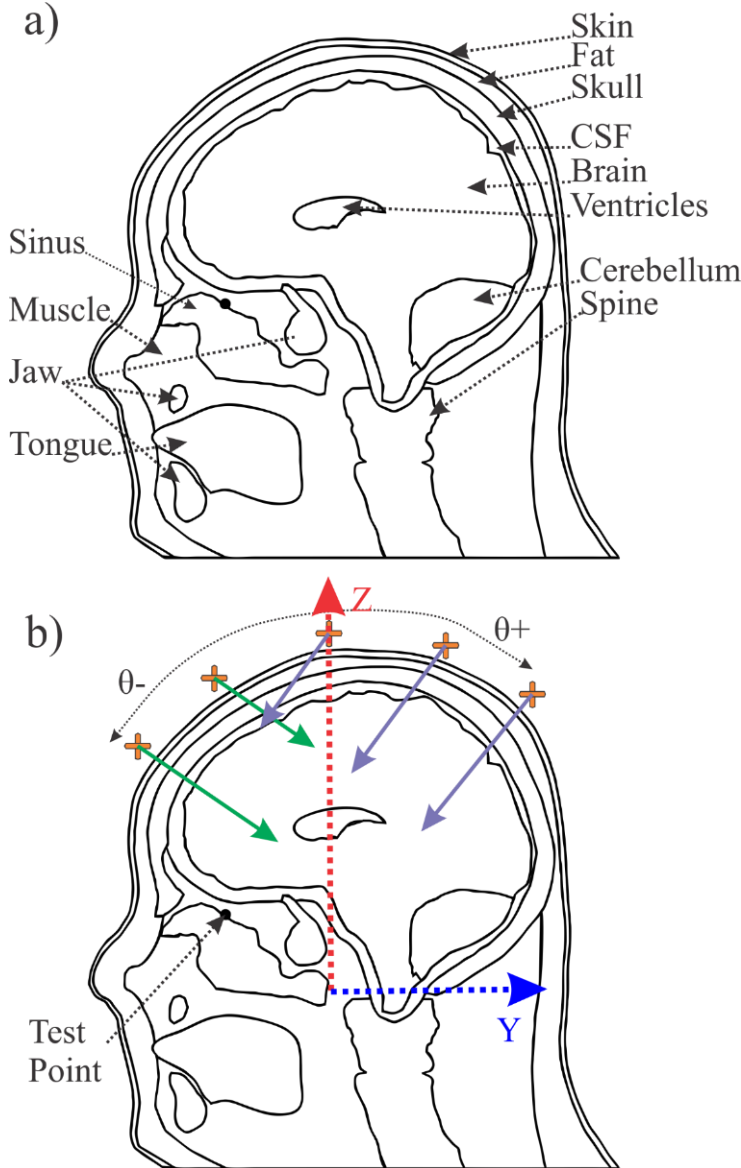


Fig. 4. Cross section of the sagittal (YZ) plane of the human head model. a.) Locations of included organs, b.) Examples of antenna locations with respect to θ . The phase of the excitation was adjusted such that the 45° beam transveres the head, as indicated

the brain and is vital to the accuracy of any electromagnetic simulation involving the head, followed a slightly different process. Since the brain can move about in the CSF, certain cryoslices depicted the brain directly adjacent to the skull with no space allocated for the CSF. Therefore, the brain mesh model was converted via 3D Delaunay tessellation to a strictly convex shape. Such an operation will allow for all non-convex cavities on the brain surface to be filled with the CSF. This boundary triangular mesh may be extracted from the tetrahedral mesh and scaled to match an expected 2.5

mm-thick CSF layer.

The final mesh used in these simulations is a refined version of the one presented in [11] with additional organs and tissues shown in Fig. 4 to provide a more accurate model of the human head. Although not directly intersecting the YZ plane in Fig. 4, the eyes are also included in the simulations. The brain is considered a single combined mass, whose permittivity is also given by [55]. The ventricles in the brain are assumed to be filled with CSF.

Table 1-Comparison of commercially available human body meshes

Company/Product name	Human body model
ANSYS HFSS and Maxwell3D Product of the United States	<u>Outdated human body model</u> from Aarkid Limited, Scotland 2005. The model has a number of flaws; actively looking for better models [79]
CST Microwave Studio/EM Studio Product of Germany	<u>Dated European human body models</u> from 80s and 90s including the HUGO human body model, SAM phantom heads, and SAM phantom hands [76]
SEMCAD X Product of Switzerland	<u>World leader</u> : Virtual Swiss family with about 80 tissues per person, supported by Swiss Government . V3.x to be released in early 2013. Not suitable for FEM modeling. Must use SEMCAD X. [77]
XFDTD of REMCOM Product of the United States	Repositionable Visible Human Project Male (1989-1995) including low-resolution internal anatomical structures, lacking some internal anatomical structures. [78]
FEKO Product of South Africa	Visible Human Project Male model (1989-1995) of limited resolution [75]

MATERIAL PROPERTIES

The accurate portrayal of the material properties of the organs is vital to the success of these simulations. All of the materials were assigned their appropriate material properties such that the simulation software could interpret which boundary conditions to use and how to calculate the attenuation constant inside each lossy volume. All of the data for the material properties used in this project were obtained from the Foundation for Research on Information Technologies in Society (IT'IS) [56]. IT'IS is an internationally recognized organization in Switzerland, organized by the Swiss Government and academia. They specialize in electromagnetic research and their list of supporters include [56]:

- Centre for Technology Assessment (TA-SWISS) – Switzerland
- Federal Institute for Occupational Safety and Health (BAuA) – Germany
- National Institute of Environmental Health Sciences (NIEHS) – USA

Electric permittivity describes how easily an electric field can polarize the molecules in a medium [57]. Naturally, this is a property of the material in question. Complex permittivity can be broken up into a real and imaginary component:

$$\varepsilon = \varepsilon' - j\varepsilon'' \quad (1)$$

This loss factor can be defined:

$$\varepsilon'' = \frac{\sigma}{\varepsilon_0 \omega} \quad (2)$$

One should note that permittivity is frequency dependent and is often given as a function of the angular frequency, ω . The permittivity of free-space, ε_0 , is a constant. Furthermore, it is dependent on another, more tangible property, conductivity, σ . Conductivity is determined by the ease of which the ionic transfer of electrons occurs within the medium [57]. Fundamentally, this results in two material properties that define electrical characteristics of media: the dielectric constant ε' (often simply referred to as ε or, more correctly, ε_r) and the conductivity, σ .

This paper is not intended to go into significant detail into measurement of dielectric materials and the effects at the cellular level, but a brief synopsis of the methods used in [57], [58], [59], and [41] is provided here, as this is where our material data were obtained. Researchers often divide the dielectric properties of biological tissue into three dispersion regions. The boundaries between each region are debatable and gradual, but they illustrate three distinct phases in which the material properties change. These are summarized in Table 2 [57].

Table 2- Dispersion regions of biological tissue [57]

Name	Range	Cause	Characteristic
α	$< 10kHz$	Ionic diffusion of particles in and out of cell membrane	$\epsilon_r > 1000$ $\sigma < 1$
β	$\sim 100kHz$ $- 1GHz$	Polarization of membrane and proteins	Quick decrease in ϵ_r Gradual increase in σ
γ	$> 1GHz$	Polarization of water molecules	Low ϵ_r Sharp increase in σ

An example of the material properties provided by Gabriel and IT'IS is provided in Fig. 5. Although the dispersion regions are listed as mutually exclusive, discrete region in the figure, they are continuous regions that gradually transition from one to another. The majority of our studies are in the 100MHz to 1GHz range, which is governed by the β region and the polarization of cell membranes and proteins [57]. This clearly has a direct biological connection.

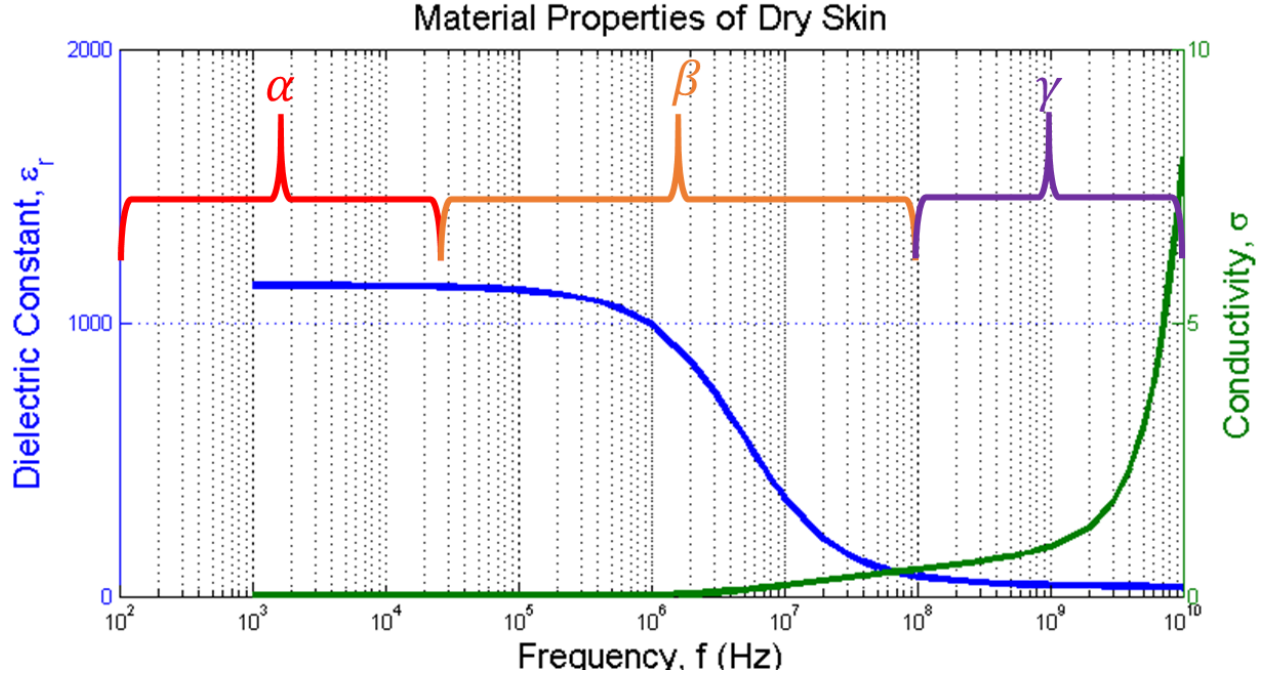


Fig. 5. Example of material properties provided by IT'IS with labeled dispersion regions

Gabriel used the well known co-axial probe technique to find the capacitance and conductance of the unknown samples to reverse engineer the dielectric constant and conductivity. Their measurements were taken using impedance analyzers in the 300kHz to 3GHz range and combined with those later taken from the 130MHz to 20GHz. The capacitance, C , and the conductance, G , of the probe in the material was compared with the capacitance in air, K , using the standard relationships [58]:

$$\epsilon'_r = \frac{C}{K}; \quad \sigma = \frac{G\epsilon_0}{K} \quad (3)$$

The comparison to air proved unreliable due to stray capacitance, lead inductance, and polarization of the electrodes. Gabriel corrected these inaccuracies by calibrating the test set up with known saline solutions and using sputtered platinum electrodes (the polarization effect was shifted lower than standard gold electrodes). For frequencies greater than 100MHz, the variations between samples were less than 10%, which was deemed to be within the expected range of natural variation between biological entities [58].

The aforementioned co-axial probe measurement technique requires a sample size of at least 5cm × 5cm, thus human samples were not always available. For skin and tongue tissue, Gabriel used *in*

vivo human samples. When available, human cadavers (24 hours to 48 hours post-mortem) were tested. Lacking either of the above, similar animals were killed and tested less than 2 hours post-mortem. Gabriel also showed a tight correlation between human and animal tissues for organs with samples from both species [58].

Although Gabriel's measurements covered discrete points from 10 Hz to 20 GHz, one must make an accurate model to interpolate and extrapolate points. By examining Fig. 5, one can see that a linear model is a very poor approximation to either the dielectric constant or the conductivity. Generally, one generates a parametric model based on dispersion regions to describe the change of material properties as frequency increases. One of the most common and straightforward methods is the Debye relaxation equation [59]:

$$\varepsilon(\omega) = \varepsilon_{\infty} + \frac{\varepsilon_s - \varepsilon_{\infty}}{1 + j\omega\tau} \quad (4)$$

Here, the relaxation time for the medium in question is defined by τ , which is the time (in seconds) for the polarization to reach equilibrium after a change in the electric field. The two terms ε_s and ε_{∞} describe the dielectric constant for $\omega\tau \ll 1$ and $\omega\tau \gg 1$, respectively [59]. This relaxation time is generally greater in water than it is in biological tissue because of organic interactions with the tissue [41]. Unfortunately, each dispersion region has multiple regions, thus a more general Cole-Cole dispersion model was selected [59]:

$$\varepsilon(\omega) = \varepsilon_{\infty} + \sum_{i=1}^n \frac{\varepsilon_{si} - \varepsilon_{\infty}}{1 + (j\omega\tau_i)^{(1-\alpha_i)}} + \frac{\sigma_i}{j\omega\varepsilon_0} \quad (5)$$

This model takes into account the conductivity, σ_i and the "broadening" of the dispersion, α_i for the i^{th} dispersion region. Instead of using a least squares fit, which would be heavily biased by the low frequency data, Gabriel et al used a customized, systematic method to recursively generate a parametric model for each individual tissue layer [59].

ORTHOGONAL COIL ANTENNAS: THEORY

The orthogonal coils were selected as the transmitters for their highly directive radiation pattern that is excited when they are placed close to a dielectric interface. Such a pattern is necessary for isolating and localizing the effects changes in the dielectric media as well the establishment of a discrete, clearly defined channel within the human head. Clearly, an omnidirectional antenna, such as the simple dipole, would lead to significant multipath and provide very little useable information on the path of propagation. Signal processing techniques could be used to separate these components, but these would be prohibitively complicated, and require a priori knowledge of the exact layout and composition of the head under test.

A.) AN ANTENNA ABOVE A DIELECTRIC INTERFACE: PREVAILING THEORIES

Most antennas are in close proximity to some foreign medium that has a dielectric constant greater than one (i.e. the antenna is near anything that is not air or a vacuum). As such, several approaches to finding the electromagnetic fields inside such a medium has been developed over the past several decades. I briefly outline three of the most common theories, those of Sommerfeld, Carson, and Banos [60]. The following sections provide a brief outline of the current literature. A more in depth summary can be found in [60], and the interested reader can view the full original documents in [61], [62], and [63].

As opposed to working directly with the electric and magnetic fields (\mathbf{E} and \mathbf{H} , respectively), all of the above authors use an artificial construct called the Hertzian vector potential [60]. Before examining each of their theories, one must first understand what this potential represents.

The Maxwell equations are a classic set of electromagnetic relations between material properties (dielectric permittivity, ϵ , magnetic permeability, μ , and conductivity, σ), current density (\mathbf{J}), and field quantities (electric field, $\vec{\mathbf{E}}$, electric displacement, $\vec{\mathbf{D}}$, magnetic field, $\vec{\mathbf{H}}$, magnetic flux density, $\vec{\mathbf{B}}$). Generally, solving these partial differential equations is complicated and nearly impossible for all but the simplest cases (unless evaluated numerically by simulation software). Introductory antenna or electromagnetics texts will introduce the vector Helmholtz equation (also known as the wave equation)

for time-invariant, linear, isotropic media. Applying these simplifying assumptions and vector identities to the original Maxwell equations, we arrive at the famous Helmholtz equation (for wavenumber, k , and an vector quantity, \vec{a} , which can be either the electric or magnetic field) [64]:

$$\nabla^2 \vec{a} - k^2 \vec{a} = 0 \quad (3)$$

By increasing the order of Maxwell's equations (which also increases the complexity) and applying boundary conditions, one can eliminate equations and form a determinate system that can be solved for the desired field quantity. However, many physicists have opted to use auxiliary variables to generate simplified and more compact expressions. One of the most commonly used variables is the magnetic vector potential, \vec{A} . Given a known current density (\vec{J}_0), there exists a magnetic vector potential that satisfies [64]:

$$\vec{H} = \frac{1}{\mu} \nabla \times \vec{A} \quad (4)$$

Furthermore, the magnetic vector potential can be related back to the electric field by an arbitrary scalar function, known as the scalar electric potential, φ [64]:

$$\vec{E} = j\omega \vec{A} - \nabla \varphi \quad (5)$$

The selection of this scalar electric potential function is referred to as a so-called “gauge.” The $\varphi = 0$ gauge is the simplest assumption, but can result in impractical complications if a source is present that does not have a divergence of 0. This can happen for electrically small antennas that are much shorter than a wavelength [64].

Alternatively, one can use the Coulomb gauge to select φ . Noticing how similar the preceding equation for the vector magnetic potential is to the electrostatics condition of $\vec{E} = -\nabla \varphi$, a natural choice for φ is the solution to the equation for electrostatic potential (the Poisson equation) [64]:

$$\nabla^2 \varphi = \frac{\nabla \cdot \vec{J}_0}{j\omega \epsilon_c} \quad (6)$$

The Coulomb gauge, by the above condition, forces the magnetic vector potential to be a solenoid. Therefore this particular gauge offers the simplification of $\nabla \cdot \vec{A} = 0$, yet adds the difficulty of

solving the Poisson equation. This additional complexity has made it less popular than the Lorentz gauge [64].

The final gauge we will discuss is the Lorentz gauge. Taking advantage of the $-\omega^2\mu\epsilon$ term (in the time domain), one can find a φ , such that the divergence of vector magnetic potential is [64]:

$$\nabla \cdot \vec{A} = j\omega\mu\epsilon\varphi \quad (7)$$

From here, it is straightforward to substitute this value into the equation \vec{A} , and rewrite it in terms material properties, the current density, and the vector magnetic potential (presumably the only unknown):

$$\nabla^2 \vec{A} - \omega^2\mu\epsilon\nabla\vec{A} = -\mu\vec{J}_0 \quad (8)$$

Before leaving the Lorentz gauge, one should note that it is very convenient if the divergence of the current in a field of interest is 0 ($\nabla \cdot \vec{J}_0 = 0$), as this causes $\varphi = 0$. This implies that the charges are either stationary or moving exclusively in closed loops over the region of interest [64].

Many antennas have charges that oscillate about a fixed position. To this end, it helps to introduce a new artificial variable call the Hertz vector potential, $\vec{\Pi}$. Note that this is not the same as the vector magnetic potential, \vec{A} , used above. The Hertz vector potential encodes the frequency in it, and has units of $V \cdot m$, as opposed to $\frac{Wb}{m}$ for \vec{A} . This new vector potential is defined as [64]:

$$\vec{\Pi} = \frac{j\omega}{k^2} \vec{A} \quad (9)$$

Applying the Laplace operator to the Hertz vector potential allows it to be expanded as a partial differential equation with respect to time [60]:

$$\nabla^2 \vec{\Pi} = \left(\epsilon\mu \frac{\partial^2}{\partial t^2} + \sigma\mu \frac{\partial}{\partial t} \right) \vec{\Pi} \quad (10)$$

The previous equality will be useful in exploiting symmetry. The Hertz vector potential allowed Sommerfeld to write the electric and magnetic fields more compactly [61]:

$$\vec{E} = k^2 \vec{\Pi} + \nabla \nabla \cdot \vec{\Pi} \quad (11)$$

$$\vec{\mathbf{H}} = \frac{k^2}{\mu_0 \mu_r j \omega} \nabla \times \vec{\Pi} \quad (12)$$

B.) SOMMERFELD'S THEORY

German physicist Arnold Sommerfeld was possibly the earliest investigator of EM field propagation in a medium. In 1899 he published a paper regarding the fields near wires, becoming one of the first to explore radiation through lossy media [44]. Sommerfeld was primarily interested in the radiation above ground (a conductive medium) [60]. He considers infinitesimally small dipole, the so-called “Hertzian dipole,” which is simply two wings of a dipole (two pieces of wire), small enough that the current distribution is uniform across them. He splits the Hertz potential into two separate components: Π_{prim} , which is the potential due to the dipole as if it were in free space, and Π_{sec} , which is the potential due solely to the reflections from the ground [60]. This is very similar to image theory in antenna design, where a dipole above a conductor creates a so-called “image” or reflection in a conductor; acting as though the reflection is another dipole [1].

For ease of notation, we will compress the frequency and angular properties into the angular wavenumber, which is given as:

$$k = \sqrt{\epsilon \mu \omega^2 + j \mu \sigma \omega} \quad (13)$$

Let us now consider a vertically oriented dipole above a conducting interface. Sommerfeld elected to use cylindrical coordinates, as the boundary could be defined in a piecewise fashion, purely in the z direction. Furthermore, due to symmetry in the ϕ direction, $\frac{\partial}{\partial \phi} = 0$. The z component of the Hertz potential then becomes [60]:

$$\left(\frac{\partial^2}{\partial r^2} + \frac{1}{r} \frac{\partial}{\partial r} + k^2 + \frac{\partial^2}{\partial z^2} \right) \Pi_z = 0 \quad (14)$$

This partial differential equation has eigenfunctions in the form of:

$$u = J_0(\lambda r) \cos(\mu z), k^2 = \lambda^2 + \mu^2, \quad (15)$$

where J_0 is no longer the current density, but rather the first order Bessel function. Although λ is still the wavelength, the μ above does not refer to the magnetic permeability, but is instead a placeholder variable:

$$\mu = \frac{m\pi}{h}, \quad (16)$$

where m is an integer, and h , is the height of our cylindrical coordinate system. By allowing the coordinate system to expand vertically to infinity, m becomes insignificant and we can treat this as a continuous distribution of eigenfunctions. We can integrate across these eigenfunctions (as a function of the wavelength) to find Π_z [60]:

$$\Pi_z = \int_0^\infty F(\lambda) J_0(\lambda r) e^{\pm \mu z} d\lambda, \mu = \sqrt{\lambda^2 - k^2}, \quad (17)$$

where $F(\lambda)$ is some unknown function of the wavelength. Note that μ acts as the propagation constant, and thus the sign of the positive real part only has physical significance. Sommerfeld considers the case where the source is located directly at the interface, that is, $z = 0$. This reduces the Hertz potential to:

$$\Pi_z = \frac{e^{jkR}}{R}, R^2 = r^2 + z^2, \quad (18)$$

This then leads to the unknown function $F(\lambda)$ to be defined by [60]:

$$F(\lambda) = \frac{\lambda}{\mu} \quad (19)$$

Substituting this expression for $F(\lambda)$ into the integral for the Hertz potential in the z direction, we arrive at:

$$\Pi_z = \frac{1}{2} \int_{-\infty}^\infty \frac{\lambda}{\mu} H_0^{(1)}(\lambda r) e^{-\mu|z|} d\lambda, \quad (20)$$

where $H_0^{(1)}$ is a Hankel function of the first kind [61]. This is the Hertz potential in the z direction for a dipole located in free space.

If the interface were a perfect electrical conductor, the boundary conditions produce an antenna image, as mentioned previously. This image of the vertically oriented dipole has the same polarity as the original, thus if excited directly on the interface ($z = 0$), the Hertz potentials add in phase. Conversely, a horizontal dipole cannot exploit this symmetry, and instead the Hertz potentials cancel because they are 180° out of phase. This notion can be expanded by giving the lower half-space (which is now considered only partially conductive) as having a permittivity and a complex conductivity. We can now take our expression for the dipole in the air (Primary) and add the effect from the induced currents from the lower half-space (secondary) for an antenna located at a height h above the medium [60]:

$$\Pi_z = \begin{cases} \int_0^\infty J_0(\lambda r) d\lambda \left(\frac{\lambda}{\mu} e^{-\mu(z-h)} + e^{-\mu(z+h)} F(\lambda) \right), & h < z \\ \int_0^\infty J_0(\lambda r) d\lambda \left(\frac{\lambda}{\mu} e^{\mu(z-h)} + e^{-\mu(z+h)} F(\lambda) \right), & 0 < z < h \\ \int_0^\infty J_0(\lambda r) d\lambda e^{\mu_E z - \mu h} F_E(\lambda), & -\infty < z < 0 \end{cases} \quad (21)$$

Note that the last region (the Hertz vector potential in the lower medium, or $z < 0$), μ_E is separately defined as:

$$\mu_E = \sqrt{\lambda^2 - k_E^2}, \quad (22)$$

which uses the wavenumber in the second medium as opposed to air. The subscript E originally stood for “Earth,” as Sommerfeld was interested in radio waves over a partially conductive ground [60]. However, the functions $F(\lambda)$ and $F_E(\lambda)$ remain unknown. To determine these, Sommerfeld applies the boundary condition that the tangential components of \vec{E} and \vec{H} must both be continuous across the interface. These translate into the following continuity conditions at the interface ($z = 0$) [60]:

$$\frac{\partial \Pi}{\partial z} = \frac{\partial \Pi_E}{\partial z}, \quad \Pi = \frac{k_E^2}{k^2} \Pi_E \quad (23)$$

The preceding relation produces the following system of equations when applied to our definition of Π_z :

$$\mu F + \mu_E F_E = \lambda, \quad \mu F - \frac{k_E^2}{k^2} \mu F_E = -\lambda \quad (24)$$

It is now straightforward to solve for these functions in terms of known quantities:

$$F(\lambda) = \frac{\lambda}{\mu} \left(1 - \frac{2\mu_E}{\mu \left(\frac{k_E}{k} \right)^2 + \mu_E} \right), \quad F_E(\lambda) = \frac{2\lambda}{\mu \left(\frac{k_E}{k} \right)^2 + \mu_E} \quad (25)$$

Unfortunately, the analysis of a horizontal dipole above a conductive interface is more complex, as we can no longer exploit symmetry in the ϕ direction (the dipole is now parallel to the surface). If the dipole is oriented along the x-axis, thus one must consider the parallel component (Π_x) and the perpendicular component (Π_z). This provides us with two analogous sets of boundary conditions for the electric and magnetic fields separately [60]. The boundary condition for the electric field become:

$$\nabla \cdot \vec{\Pi} = \nabla \cdot \vec{\Pi}_E, \quad k^2 \Pi_x = k_E^2 \Pi_E^2 \quad (26)$$

Similarly, Sommerfeld gives the boundary conditions for the magnetic field:

$$\Pi_z = \left(\frac{k_E}{k} \right)^2 \Pi_{Ez}, \quad \frac{\partial \Pi_x}{\partial z} = \left(\frac{k_E}{k} \right)^2 \frac{\partial \Pi_{Ex}}{\partial z} \quad (27)$$

We now have a relationship between the two components, which can be rewritten as:

$$\Pi_x = \left(\frac{k_E}{k} \right)^2 \Pi_{Ex}, \quad \frac{\partial \Pi_x}{\partial z} = \left(\frac{k_E}{k} \right)^2 \frac{\partial \Pi_{Ex}}{\partial z} \quad (28)$$

$$\Pi_z = \left(\frac{k_E}{k} \right)^2 \Pi_{Ez}, \quad \frac{\partial \Pi_z}{\partial z} - \frac{\partial \Pi_{Ez}}{\partial z} = \frac{\partial \Pi_{Ex}}{\partial x} - \frac{\partial \Pi_x}{\partial x} \quad (29)$$

The Hertz potential in the x direction for the horizontal dipole is very similar to that of the Hertz potential in the z direction for the vertical dipole. Sommerfeld shows that $F(\lambda)$ now becomes:

$$F(\lambda) = \frac{\lambda}{\mu} \left(\frac{2\mu}{\mu + \mu_E} - 1 \right), \quad F_E(\lambda) = \left(\frac{k}{k_E} \right)^2 \frac{2\lambda}{\mu + \mu_E} \quad (30)$$

From here, substitution reveals:

$$\Pi_x = \frac{e^{jkR}}{R} - \frac{e^{jkR'}}{R'} + 2 \int_0^\infty J_0(\lambda r) e^{-\mu(z+h)} \left(\frac{\lambda}{\mu + \mu_E} \right) d\lambda \quad (31)$$

$$\Pi_{Ex} = 2 \left(\frac{k}{k_E} \right)^2 \int_0^\infty J_0(\lambda r) e^{\mu_E z - \mu h} \left(\frac{\lambda}{\mu + \mu_E} \right) d\lambda, \quad (32)$$

where R is the distance from the antenna to the interface, and R' is the distance from the image of the antenna to the interface [60].

The horizontal dipole still has a z component, thus we must solve the wave equation:

$$(\nabla^2 + k^2)\Pi_z = 0 \quad (33)$$

Sommerfeld provides that the solution to this differential equation is:

$$\Pi_z = J_m(\lambda r) e^{-\mu z} e^{im\phi} \quad (34)$$

The boundary conditions that were previously established show that the azimuthal factor is $\cos(\phi)$, thus the eigenfunctions are instead based on first order Bessel functions (J_1 instead of J_0) [61]. Currents in the second medium induce currents in the x direction (noting the antenna is parallel to the x axis); however, this implies the primary field has no effect on Π_z . We now have enough information to solve for the remaining component of the Hertz vector potential [60]:

$$\Pi_z = -\frac{2 \cos(\phi)}{k^2} \int_0^\infty J_1(\lambda r) e^{-\mu(z+h)} \lambda^2 \left(\frac{\mu - \mu_E}{\mu \left(\frac{k_E}{k} \right)^2 + \mu_E} \right) d\lambda, \quad z > 0 \quad (35)$$

$$\Pi_z = -\frac{2 \cos(\phi)}{k_E^2} \int_0^\infty J_1(\lambda r) e^{-\mu_E z - \mu h} \lambda^2 \left(\frac{\mu - \mu_E}{\mu \left(\frac{k_E}{k} \right)^2 + \mu_E} \right) d\lambda, \quad z < 0 \quad (36)$$

C.) BANOS' THEORY

Alfredo Banos, a Mexican-American Professor, also used a Hertzian dipole and the Hertz vector potential; however, his approach makes use of the Green's function after using a triple Fourier transform (in the spatial domain). After generating differential relations between the Hertz potential and each spatial coordinate of the electric and magnetic fields, Banos focuses heavily on saddle point methods to solving specific situations on a case-by-case basis [62].

Banos applies the continuity charge to this problem, where the charge density, ρ , must be continuous across the interface [60]:

$$\nabla \cdot \vec{J} = j\omega\rho \quad (37)$$

Banos then presents the inhomogeneous Helmholtz equation for the horizontal electric dipole along the x-axis in terms of the impressed current density, \vec{J}^0 [60]:

$$(\nabla^2 + k^2)\vec{\Pi} = \frac{-j\vec{J}^0}{\omega\varepsilon + j\sigma} \quad (38)$$

He defines this impressed current density as in the x direction as:

$$\vec{J}^0 = \hat{e}_x p \delta(x) \delta(y) \delta(z - h), \quad (39)$$

where \hat{e}_x is the unit vector in the x direction, $\delta(x)$ is the Dirac delta function, and p is proportional to the dipole moment. It is given by $p = I\Delta\ell$, where I is the current through the dipole, and $\Delta\ell$ is the length [60]. Banos then uses the Green's function in the previous Helmholtz equation:

$$(\nabla^2 + k^2)G = -4\pi\delta(x)\delta(y)\delta(z) \quad (40)$$

The solution of which, for the electric dipole moment, is:

$$G = \frac{e^{jkR}}{R} \quad (41)$$

Banos then finds that the vector magnetic potential can be described as:

$$\vec{\Pi} = \hat{e}_r \Pi_x \cos(\phi) - \hat{e}_\phi \Pi_x \sin(\phi) + \hat{e}_z \Pi_z \quad (42)$$

The fields for the horizontal dipole are summarized in Table 3 [60]:

Table 3. Banos' results for the field components of a horizontal electric dipole above a conductive interface

	\vec{E}	\vec{H}
r	$\frac{\partial}{\partial r} (\nabla \cdot \vec{\Pi}) + k^2 \Pi_x \cos(\phi)$	$-\frac{jk^2}{\omega\mu_0} \left(\sin(\phi) \frac{\partial \Pi_x}{\partial z} + \frac{1}{r} \frac{\partial \Pi_z}{\partial \phi} \right)$
ϕ	$\frac{1}{r} \frac{\partial}{\partial \phi} (\nabla \cdot \vec{\Pi}) - k^2 \Pi_x \sin(\phi)$	$-\frac{jk^2}{\omega\mu_0} \left(\cos(\phi) \frac{\partial \Pi_x}{\partial z} - \frac{\partial \Pi_z}{\partial r} \right)$

z	$\frac{\partial}{\partial z}(\nabla \cdot \mathbf{\Pi}) + k^2 \Pi_z$	$\frac{jk^2}{\omega\mu_0} \left(\sin(\phi) \frac{\partial \Pi_x}{\partial r} \right)$
-----	--	--

D.) WAIT'S THEORY

James Wait, a Canadian electrical engineer and physicist again uses the Hertz vector potential, but his methods are slightly different than those of Sommerfeld and Banos. Wait instead uses a vector based approach, using both electric and magnetic current [63].

Wait begins his text with an overview of the Hertz vector potential and the claim that only the z component is necessary in free space, as the magnetic field is perpendicular to the radial and axial vectors, thus orbiting the z -axis [60]. He uses the fictitious magnetic current density, $\vec{\mathbf{M}}$, which is analogous to traditional electric current density, $\vec{\mathbf{J}}$:

$$\nabla \times \vec{\mathbf{E}} = -j\mu\mu_0\omega\vec{\mathbf{H}} - \vec{\mathbf{M}} \quad (43)$$

$$\nabla \times \vec{\mathbf{H}} = (\sigma + j\omega\epsilon\epsilon_0)\vec{\mathbf{E}} + \vec{\mathbf{J}} \quad (44)$$

Unlike Sommerfeld and Banos, Wait introduces a new abstract quantity, the magnetic Hertz vector, $\vec{\mathbf{\Pi}}^*$, which is the counterpart of the traditional Hertz vector potential ($\vec{\mathbf{\Pi}}$) [60].

$$\vec{\mathbf{\Pi}}^* = \frac{1}{4\pi j\mu\mu_0\omega} \int_V \frac{e^{-jkR}}{R} \vec{\mathbf{M}} dV \quad (45)$$

He then expends this theory to an infinitesimal loop of current, oriented parallel to the material interface (i.e. a vertical magnetic dipole). Wait integrates around said loop and applies the same method as performed with the electric dipole to derive the magnetic Hertz potential for the magnetic dipole [60]:

$$\Pi_z^* = \frac{m}{4\pi} \left(\frac{e^{-jkR}}{R} \right), \quad (46)$$

where m is the magnetic moment of the loop.

E.) AN ANTENNA ABOVE A DIELECTRIC INTERFACE: ANGULAR SPECTRA

Let us first consider the case of a simple loop, or horizontal magnetic dipole above a dielectric interface. One must consider the optical fields produced by this dipole, which are composed of the plane waves and evanescent waves that satisfy the Maxwell's equations. To describe these fields, we make use of the spatial Fourier transform, resulting in the so-called angular spectrum [65]. Let us assume the electric field at any given point is defined by $\mathbf{E}(\rho, \phi, z)$. The angular spectrum representation is then defined by:

$$\widehat{\mathbf{E}}(\rho, \phi, z) = \int_{-\infty}^{+\infty} \int_0^{2\pi} \mathbf{E}(\rho, \phi, z) e^{-j(k_\phi \phi + k_\rho \rho)} d\phi d\rho \quad (47)$$

Using the spectral density function, $\vec{A}(\vec{K})$, we shall define the fields in both regions as described by Smith in [7]. This function is divided into a linear combination of its parallel and perpendicular components with respect to the plane of incidence. Provided we know the incident electric field vector \vec{E}_i ,

$$\mathbf{A}_{||}^{\pm}(\vec{K}) = \frac{\pm k_1 \exp[j\gamma_1(K)]}{K\gamma_1} \int_{-\infty}^{+\infty} \int_{-\infty}^{+\infty} \vec{K} \cdot \vec{E}_i(x, y, z) e^{j\vec{K} \cdot \vec{r}} dx dy \quad (48)$$

$$\mathbf{A}_{\perp}^{\pm}(\vec{K}) = \frac{-\exp[j\gamma_1(K)]}{K} \int_{-\infty}^{+\infty} \int_{-\infty}^{+\infty} \vec{K} \cdot [\hat{z} \times \vec{E}_i(x, y, z)] e^{j\vec{K} \cdot \vec{r}} dx dy, \quad (49)$$

where \vec{r} , is the observation vector. As usual, the plane-wave propagation component is given by \vec{k}_1 , which is given in terms of the transverse component \vec{K} , such that [7]:

$$\vec{k}_1^{\pm} = \vec{K} \pm \gamma_1(K) \hat{z} \quad (50)$$

$$\vec{K} = k_x \hat{x} + k_y \hat{y} \quad (51)$$

$$K = \sqrt{k_x^2 + k_y^2} \quad (52)$$

From this, we can determine that γ_1 must be:

$$\gamma_1(K) = -j\sqrt{K^2 - k_1^2}; \quad \text{where } k_1 \in \mathbb{R} \text{ and } K^2 > k_1^2 \quad (53)$$

Similarly,

$$\gamma_2(K) = -j\sqrt{K^2 - k_2^2}; \quad \text{where } k_2 \in \mathbb{R} \text{ and } K^2 > k_2^2 \quad (1)$$

To simplify the derivation, field quantities will be referred to in terms of the unit vectors of the spectral density functions, combining the main vector quantities in two terms [7]:

$$\hat{\mathbf{a}}_{||}^{\pm} = \frac{-K^2 \hat{\mathbf{z}} \pm \gamma_1(K) \vec{\mathbf{K}}}{k_1 K} \quad (2)$$

$$\hat{\mathbf{a}}_{\perp}^{\pm} = \frac{\hat{\mathbf{z}} \times \vec{\mathbf{K}}}{K}, \quad (3)$$

Now, let us consider the interface. In free space, we have the incident field directly radiated by the antenna in addition to reflections from the surface. In the dielectric medium, only the transmitted portion of the field exists (i.e. the portion that penetrates from medium 1 to medium 2). The incident electric field is given by [7]:

$$\vec{\mathbf{E}}_i^{\pm}(x, y, z) = \frac{1}{4\pi^2} \int_{-\infty}^{+\infty} \int_{-\infty}^{+\infty} [\hat{\mathbf{a}}_{||}^{\pm} A_{||}^{\pm}(\vec{\mathbf{K}}) \exp(\mp j\gamma_1(k)h) + \hat{\mathbf{a}}_{\perp}^{\pm} \hat{\mathbf{A}}_{\perp}^{\pm}(\vec{\mathbf{K}}) \exp(\mp j\vec{\mathbf{k}}_1^{\pm} \cdot \vec{\mathbf{r}})] dk_x dk_y \quad (4)$$

Here, h is the height of the antenna from the interface. If the dipole is placed directly on or very close to the interface (i.e. $h \rightarrow 0$), the $\exp(\mp j\gamma_1(k)h)$ term simplifies to 1.

The field in the second region must be split into a reflected and transmitted field for above ($z \leq 0$) and below ($z > 0$) the interface respectively. This then leads to:

$$\vec{\mathbf{E}}_r(x, y, z) = \frac{1}{4\pi^2} \int_{-\infty}^{+\infty} \int_{-\infty}^{+\infty} [\hat{\mathbf{a}}_{||}^r R_{||}(K) A_{||}^+(\vec{\mathbf{K}}) + \hat{\mathbf{a}}_{\perp}^r R_{\perp}(K) A_{\perp}^+(\vec{\mathbf{K}})] \quad (5)$$

$$\cdot \exp(-j\gamma_1(K)h - j\vec{\mathbf{k}}_1^- \cdot \vec{\mathbf{r}})] dk_x dk_y$$

$$\vec{\mathbf{E}}_t(x, y, z) = \frac{1}{4\pi^2} \int_{-\infty}^{+\infty} \int_{-\infty}^{+\infty} [\hat{\mathbf{a}}_{||}^t T_{||}(K) A_{||}^+(\vec{\mathbf{K}}) + \hat{\mathbf{a}}_{\perp}^t T_{\perp}(K) A_{\perp}^+(\vec{\mathbf{K}})] \quad (6)$$

$$\cdot \exp(-j\gamma_1(K)h - j\vec{\mathbf{k}}_t \cdot \vec{\mathbf{r}})] dk_x dk_y,$$

Note that the propagation vector for the transmitted field, $\vec{\mathbf{k}}_t$, is defined by:

$$\vec{\mathbf{k}}_t = \vec{\mathbf{K}} + \gamma_2(K) \hat{\mathbf{z}} \quad (7)$$

Smith defines the reflection and transmission coefficients using the boundary conditions at the interface, which are given in Table 4 [7].

Table 4. General reflection and transmission coefficients at a dielectric interface

Reflection/Transmission Coefficient	Expression
$R_{\parallel}(K)$	$\frac{k_2^2\gamma_1 - k_1^2\gamma_2}{k_2^2\gamma_1 + k_1^2\gamma_2}$
$R_{\perp}(K)$	$\frac{\gamma_1 - \gamma_2}{\gamma_1 + \gamma_2}$
$T_{\parallel}(K)$	$\frac{2k_1k_2\gamma_1}{k_2^2\gamma_1 + k_1^2\gamma_2}$
$T_{\perp}(K)$	$2\gamma_1(\gamma_1 + \gamma_2)$

In the air above the interface, the total electric field is the sum of the incident and reflected fields by superposition, whereas the fields in the medium are due totally to transmission:

$$\begin{aligned} \vec{E}_1(x, y, z) = & \frac{1}{4\pi^2} \int_{-\infty}^{+\infty} \int_{-\infty}^{+\infty} \left[\hat{a}_{\parallel}^r [A_{\parallel}^-(\vec{K}) e^{j\gamma_1(K)h} + R_{\parallel}(K) A_{\parallel}^+(\vec{K}) e^{j\gamma_1(K)h}] \right. \\ & \left. + \hat{a}_{\perp}^r [A_{\perp}^-(\vec{K}) e^{j\gamma_1(K)h} + R_{\perp}(K) A_{\perp}^+(\vec{K}) e^{j\gamma_1(K)h}] e^{-j\vec{k}_1^- \cdot \vec{r}} \right] dk_x dk_y; z \\ & \leq -h - \delta_- \end{aligned} \quad (8)$$

$$\begin{aligned} \vec{E}_2(x, y, z) = & \frac{1}{4\pi^2} \int_{-\infty}^{+\infty} \int_{-\infty}^{+\infty} \left[[\hat{a}_{\parallel}^t T_{\parallel}(K) A_{\parallel}^+(\vec{K}) + \hat{a}_{\perp}^t T_{\perp}(K) A_{\perp}^+(\vec{K})] \right. \\ & \left. \cdot \exp(-j\gamma_1(K)h - j\vec{k}_t \cdot \vec{r}) \right] dk_x dk_y; z \geq 0, \end{aligned} \quad (9)$$

Note that up to this point, we still have not made any assumptions about the antenna exciting this field. This general equation for the fields holds for both the near and far-field for any antenna, provided we know the incident field of the specific antenna. However, as a simplification, let us examine the far-field in either region by selecting an observation point that is far away from the antenna (i.e. $k_i r \rightarrow +\infty$). Smith does this and provides us with the so-called “geometric optics” field, retaining only the dominating asymptotic term $\exp\left(-\frac{jk_i r}{k_i r}\right)$, which is valid as long as one is far from the antenna and not close to the

horizon ($\theta = 90^\circ$). The geometric optics fields are provided for each interface in spherical coordinates for simplicity [7]:

Table 5. Components of the electric field for an arbitrary antenna above a dielectric interface in the far field

Component	Medium 1 (Air) $\frac{\pi}{2} < \theta \leq \pi$	Medium 2 (dielectric) $0 < \theta \leq \frac{\pi}{2}$
$E_\theta(r, \theta, \phi)$	$\frac{j e^{-jk_1 r} k_1 \cos(\theta) }{2\pi r} \bullet$ $[A_{\parallel}^-(\vec{K}_{s1}) e^{jk_1 h \cos(\theta) } + A_{\parallel}^+(\vec{K}_{s1}) R_{\parallel}(K_{s1}) e^{-jk_1 h \cos(\theta) }]$	$\frac{j k_2 \cos(\theta) }{2\pi r} \exp \left[-j \left(k_2 r + h \sqrt{k_1^2 - k_2^2 \sin^2(\theta)} \right) \right] \bullet$ $A_{\parallel}^+(\vec{K}_{s2}) T_{\parallel}(K_{s2})$
$E_\phi(r, \theta, \phi)$	$\frac{j e^{-jk_1 r} k_1 \cos(\theta) }{2\pi r} \bullet$ $[A_{\perp}^-(\vec{K}_{s1}) e^{jk_1 h \cos(\theta) } + A_{\perp}^+(\vec{K}_{s1}) R_{\perp}(K_{s1}) e^{-jk_1 h \cos(\theta) }]$	$\frac{j k_2 \cos(\theta) }{2\pi r} \exp \left[-j \left(k_2 r + h \sqrt{k_1^2 - k_2^2 \sin^2(\theta)} \right) \right] \bullet$ $A_{\perp}^+(\vec{K}_{s2}) T_{\perp}(K_{s2})$

The Fresnel coefficients and spectral density functions were rewritten as functions of the transverse propagation numbers for the i^{th} medium, K_{si} . This is a geometric transformation to simplify the expressions for the fields and demonstrate the symmetry in each region. These transverse propagation numbers are defined as:

$$\vec{K}_{si} = k_i \sin(\theta) [\hat{x} \cos(\phi) + \hat{y} \sin(\phi)] \quad (10)$$

$$K_{si} = k_i \sin(\theta) \quad (11)$$

Similarly, the Fresnel coefficients are rewritten as:

Table 6. General reflection and transmission coefficients at a dielectric interface in terms of K_{si}

Reflection/Transmission Coefficient	Expression
$R_{\parallel}(K_{si})$	$\frac{\left(\frac{k_2}{k_1}\right)^2 \cos(\theta) - \sqrt{\left(\frac{k_2}{k_1}\right)^2 - \sin^2(\theta)}}{\left(\frac{k_2}{k_1}\right)^2 \cos(\theta) + \sqrt{\left(\frac{k_2}{k_1}\right)^2 - \sin^2(\theta)}}$

$R_{\perp}(K_{si})$	$\frac{ \cos(\theta) - \sqrt{\left(\frac{k_2}{k_1}\right)^2 - \sin^2(\theta)}}{ \cos(\theta) + \sqrt{\left(\frac{k_2}{k_1}\right)^2 - \sin^2(\theta)}}$
$T_{\parallel}(K_{si})$	$\frac{2\left(\frac{k_1}{k_2}\right)\sqrt{\left(\frac{k_1}{k_2}\right)^2 - \sin^2(\theta)}}{\left(\frac{k_1}{k_2}\right)^2 \cos(\theta) + \sqrt{\left(\frac{k_1}{k_2}\right)^2 - \sin^2(\theta)}}$
$T_{\perp}(K_{si})$	$\frac{2\sqrt{\left(\frac{k_1}{k_2}\right)^2 - \sin^2(\theta)}}{ \cos(\theta) + \sqrt{\left(\frac{k_1}{k_2}\right)^2 - \sin^2(\theta)}}$

F.) HORIZONTALLY ORIENTED MAGNETIC DIPOLE

The previous section provided a general format for finding the far field of an arbitrary antenna above a dielectric interface. Let us consider a horizontally oriented infinitesimal magnetic dipole with dipole moment $\vec{m} = m\hat{y}$. The parallel and perpendicular components of the spectral density function are given as [7]:

$$A_{\parallel}^{\pm}(\vec{K}) = -\frac{j\omega\mu_0 k_1 k_x m}{2K\gamma_1(K)} \quad (12)$$

$$A_{\perp}^{\pm}(\vec{K}) = \pm \frac{j\omega\mu_0 k_y m}{2K}, \quad (13)$$

Where $k_1 = \sqrt{k_x^2 + k_y^2}$ in medium 1 and k_x and k_y are simply the respective x and y components of the wavenumber in the first medium. One can think of this as the magnitude of the propagation vector in a plane, which clearly does not have a z component. One can substitute these into the expression for

the far field obtained in Table 5 to find the far field solution for a small horizontally oriented magnetic dipole above a dielectric interface.

Table 7. Far field of an infinitesimally small, horizontally oriented magnetic dipole above a dielectric interface

	Medium 1 (Air) $\frac{\pi}{2} < \theta \leq \pi$	Medium 2 (dielectric) $0 < \theta \leq \frac{\pi}{2}$
E_θ	$\zeta_1 m k_1^2 \cos(\phi) e^{jk_1 h \cos(\theta) } \bullet$ $\frac{e^{-jk_1 r}}{4\pi r} [1 + R_\parallel(K_{s1}) e^{-j2k_1 h \cos(\theta) }]$	$\zeta_2 m k_2^2 \cos(\phi) \cos(\theta) \exp\left(-jk_1 h \sqrt{1 - \left(\frac{k_2}{k_1}\right)^2 \sin^2(\theta)}\right)$ $\bullet \frac{T_\parallel(K_{s2}) e^{-jk_2 r}}{4\pi r \sqrt{1 - \left(\frac{k_2}{k_1}\right)^2 \sin^2(\theta)}}$
E_ϕ	$\zeta_1 m k_1^2 \sin(\phi) \cos(\theta) e^{jk_1 h \cos(\theta) } \bullet$ $\frac{e^{-jk_1 r}}{4\pi r} [1 - R_\perp(K_{s1}) e^{-j2k_1 h \cos(\theta) }]$	$-\zeta_2 m k_2^2 \sin(\phi) \cos(\theta) \exp\left(-jk_1 h \sqrt{1 - \left(\frac{k_2}{k_1}\right)^2 \sin^2(\theta)}\right)$ $\bullet \frac{T_\perp(K_{s2}) e^{-jk_2 r}}{4\pi r}$

Note that in Table 7, we simplify the expression by collapsing the material properties of the two regions into ζ_1 and ζ_2 , respectively. These wave impedances are given by:

$$\zeta_i = \sqrt{\frac{j\omega\mu_i}{\sigma_i + j\omega\epsilon_i}}, \quad \text{for } i = 1, 2 \quad (14)$$

G.) VERTICALLY ORIENTED MAGNETIC DIPOLE

The same method from the previous section can be used to find the fields for a vertically magnetic dipole above a dielectric interface. Smith has already found the far field for an array of arbitrary horizontal loops of current above a dielectric interface in [8]. This solution can be applied to find the far field for a single vertical magnetic dipole. Given an array of n loops, each with conductor radius a_n , outer radius of b_n , and heights, h_n , from the interface, the far field is given by [8] in Table 8.

Table 8. Far field components for an arbitrary array of horizontal loops above a dielectric interface

$E_{1\theta}$	$\frac{-\zeta_1 \cot(\theta) e^{-jk_1 r}}{r} \sum_{i=1}^n \left\{ \left[e^{jk_1 h_i \cos(\theta)} - R_{\parallel}(\theta) e^{-jk_1 h_i \cos(\theta)} \right] \sum_{m=1}^{m_{\max}} j^m m I_{mi} \sin(m\phi) J_m(k_1 b_i \sin(\theta)) \right\}$
$E_{1\phi}$	$\frac{\zeta_1 e^{-jk_1 r}}{4r} \sum_{i=1}^n \left\{ k_1 b_i \left[e^{jk_1 h_i \cos(\theta)} + R_{\perp}(\theta) e^{-jk_1 h_i \cos(\theta)} \right] \sum_{m=0}^{m_{\max}} h(m) j^m I_{mi} \cos(m\phi) [J_{m+1}(k_1 b_i \sin(\theta)) - J_{m-1}(k_1 b_i \sin(\theta))] \right\}$
$E_{2\theta}$	$\frac{\zeta_1 \cot(\theta') T_{\parallel}(\theta) e^{-jk_2 r}}{r} \sum_{i=1}^n \left\{ e^{-jk_1 h_i \cos(\theta')} \sum_{m=1}^{m_{\max}} j^m m I_{mi} \sin(m\phi) J_m(k_1 b_i \sin(\theta')) \right\}$
$E_{2\phi}$	$\frac{\zeta_1 e^{-jk_2 r} T_{\perp}(\theta)}{4r} \sum_{i=1}^n k_1 b_i \left\{ e^{-jk_1 h_i \cos(\theta')} \sum_{m=0}^{m_{\max}} h(m) j^m \cos(m\phi) I_{mi} [J_{m+1}(k_1 b_i \sin(\theta')) - J_{m-1}(k_1 b_i \sin(\theta'))] \right\}$

The Fresnel reflection and transmission coefficients are almost the same as those provided in Table 6, as they are general with respect to the orientation of the incident field, regardless of the source. The problem geometry allows us to simplify the transmission coefficients in the vertical case to:

$$T_{\parallel}(\theta) = \frac{2 \left(\frac{k_1}{k_2}\right) |\cos(\theta)|}{\left(\frac{k_1}{k_2}\right)^2 |\cos(\theta)| + \sqrt{\left(\frac{k_1}{k_2}\right)^2 - \sin^2(\theta)}} \quad (15)$$

$$T_{\perp}(\theta) = \frac{2|\cos(\theta)|}{|\cos(\theta)| + \sqrt{\left(\frac{k_1}{k_2}\right)^2 - \sin^2(\theta)}} \quad (16)$$

For the ease of notation, θ' was used to denote:

$$\theta' = \sin^{-1}\left(\frac{k_2}{k_1} \sin(\theta)\right) \quad (17)$$

Although the equations in Table 8 may appear cumbersome in the general case, we can make several simplifications. Let us have only a single horizontal loop (i.e. vertical magnetic dipole), setting $n = 1$. Therefore, only the first term of summation over the number of antennas is retained. Furthermore, we only consider an infinitesimal magnetic dipole, thus the loop radii $a = b \approx 0$. We consider the static case with uniform current distribution throughout the loop, thus we only keep $m = 0$ in the Fourier expansion. This assumption causes the θ component in either material to be 0, as all of the higher order modes in the sum are now zero (i.e. $I_{i1} = 0, I_{i2} = 0, \dots$). The magnetic moment, $m = I_0 \pi b^2$ must be held constant, otherwise the dipole will not radiate. Thus we must look at the asymptotic expansion of allowing $b \rightarrow 0$ without allowing the magnetic moment to go to zero (i.e. I_0 must offset b). We can first rewrite $E_{1\phi}$ and $E_{2\phi}$ as:

$$E_{1\phi} = \frac{\zeta_1 k_1 e^{-jk_1 r}}{4\pi r} I_0 b [e^{jk_1 h \cos(\theta)} + R_{\perp}(\theta) e^{-jk_1 h \cos(\theta)}] [J_1(k_1 b \sin(\theta)) - J_{-1}(k_1 b \sin(\theta))] \quad (18)$$

$$E_{2\phi} = \frac{\zeta_1 k_1 e^{-jk_2 r} T_{\perp}(\theta)}{4\pi r} I_0 b e^{-jk_1 h \cos(\theta')} [J_1(k_1 b \sin(\theta')) - J_{-1}(k_1 b \sin(\theta'))] \quad (19)$$

We can then look at the asymptotic expansion of the Bessel function [66]:

$$\begin{aligned}
& [J_1(k_1 b \sin(\theta)) - J_{-1}(k_1 b \sin(\theta))] \\
&= \left[\left(\frac{k_1 b \sin(\theta)}{2} \right)^1 \sum_{k=0}^{\infty} \frac{(-1)^k}{k! \Gamma(k+2)} \left(\frac{k_1 b \sin(\theta)}{2} \right)^{2k} \right. \\
&\quad \left. - \left(\frac{k_1 b \sin(\theta)}{2} \right)^{-1} \sum_{k=0}^{\infty} \frac{(-1)^k}{k! \Gamma(k)} \left(\frac{k_1 b \sin(\theta)}{2} \right)^{2k} \right]
\end{aligned} \tag{20}$$

The magnetic moment must remain constant as the radius decreases. If this radius, $b \rightarrow 0$, then b^2 is small. As k increases in the series expansion of the Bessel function, the radius is raised to increasing powers, thus it is becoming smaller and smaller. Only the leading term, which will form $m = I_0 b^2$, will be retained as it dominates the expansion (only $k = 0$ is considered for J_1 , but this term approaches 0 for J_{-1} , thus we must consider $k = 1$ for J_{-1}).

$$\begin{aligned}
& [J_1(k_1 b \sin(\theta)) - J_{-1}(k_1 b \sin(\theta))] \\
&= \left[\left(\frac{k_1 b \sin(\theta)}{2} \right) \frac{-1}{\Gamma(2)} - \left(\frac{2}{k_1 b \sin(\theta)} \right) \frac{-1}{\Gamma(1)} \left(\frac{k_1 b \sin(\theta)}{2} \right)^2 \right]
\end{aligned} \tag{21}$$

Noting that $\Gamma(2) = \Gamma(0) = 1$:

$$[J_1(k_1 b \sin(\theta)) - J_{-1}(k_1 b \sin(\theta))] = k_1 b \sin(\theta) \tag{22}$$

These simplifications cause the far field components in Table 8 to reduce to those in Table 9:

Table 9. Far field components of a vertical magnetic dipole above a dielectric interface

$E_{1\theta}$	0
$E_{1\phi}$	$\frac{\zeta_1 k_1^2 m \sin(\theta) e^{-jk_1 r}}{4\pi r} [e^{jk_1 h \cos(\theta)} + R_{\perp}(\theta) e^{-jk_1 h \cos(\theta)}]$
$E_{2\theta}$	0
$E_{2\phi}$	$\frac{-\zeta_2 k_2^2 m e^{-jk_2 r} T_{\perp}(\theta)}{4\pi r} \exp\left(-jk_1 h \sqrt{1 - \left(\frac{k_2}{k_1}\right)^2 \sin^2(\theta)}\right)$

To check these results, let us use these equations to compute the far field of a magnetic dipole in free space. There is no longer an interface between the materials, thus $h \rightarrow 0$, and the material properties of the two regions are equivalent (we assume they are in a vacuum): $\varepsilon_1 = \varepsilon_2 = \varepsilon_0$, and $\sigma_1 = \sigma_2 = 0$. Logically, we must show that $E_{1\phi} = E_{2\phi}$. Also, we must evaluate the Fresnel coefficients (this is a trivial case with no boundaries so, there should be no reflections and only perfect transmission). These are summarized in Table 10.

Table 10. Fresnel coefficients with no boundaries

Reflection/Transmission Coefficient	Expression
$R_{\parallel}(K_{si})$	0
$R_{\perp}(K_{si})$	0
$T_{\parallel}(K_{si})$	1
$T_{\perp}(K_{si})$	1

Furthermore, $\theta = \theta'$ when there are no boundaries.

$$E_{1\phi} = E_{2\phi} = \frac{\zeta k^2 m \sin(\theta) e^{-jkr}}{4\pi r} \quad (23)$$

This matches exactly with the far field of a loop in free space, as per Balanis [1]. We can perform a similar analysis for the far field of the horizontally orientated magnetic dipole, which was derived in the previous section.

$$E_{\theta} = E_{1\theta} + E_{2\theta} = \zeta m k^2 \cos(\phi) \frac{e^{-jk_1 r}}{2\pi r} \quad (24)$$

$$E_{\phi} = E_{1\phi} + E_{2\phi} = 0 \quad (25)$$

When we rotate the coordinate system by $\frac{\pi}{2}$ radians about the θ axis, to realign this solution to that of the vertical magnetic dipole (for comparison), this θ component becomes the new ϕ component:

$$E_\phi = \zeta m k^2 \cos(\theta) \frac{e^{-jk_1 r}}{2\pi r} \quad (26)$$

Using Balanis definition of the magnetic moment $m = I_m \ell = j\omega\mu I_0 \pi a^2$ [1], and collapsing this term into Smith's definition: $m = I_0 \pi a^2$ [7], the remaining terms can be absorbed into the wave impedance ζ . This allows us to establish equivalency between Smith's result (the left hand side of the equation), and Balanis result (right hand side):

$$\zeta m k^2 \cos(\theta) \frac{e^{-jkr}}{2\pi r} = \frac{-jk(j\pi a^2 \omega\mu I_0) \sin(\theta)}{4\pi r} e^{-jkr} \quad (27)$$

$$\zeta m k^2 \cos(\theta) \frac{e^{-jkr}}{2\pi r} = \zeta m k^2 \sin(\theta) \frac{e^{-jkr}}{2\pi r} \quad (28)$$

For the purposes of clarity, we can rewrite these expressions in terms of the index of refraction, which we define as:

$$n = \frac{k_2}{k_1}, \quad (29)$$

which simplifies to the familiar $n = \sqrt{\frac{\epsilon_2}{\epsilon_1}}$ if $\mu_1 = \mu_2 = 1$ and $\sigma_1 = \sigma_2 = 0$. The expressions for the far-field components of the horizontal and vertical magnetic dipoles above a planar interface are summarized in Table 11 and Table 12, respectively.

Table 11. Compact expression for the far-field of a horizontal magnetic dipole above a dielectric interface

Horizontal Magnetic Dipole		
	Medium 1 (Air)	Medium 2 (dielectric)
E_θ	$\omega\mu_0 m k_1 \cos(\phi) e^{jk_1 h \cos(\theta) } \frac{e^{-jk_1 r}}{4\pi r} \cdot$ $\left[1 + \frac{n^2 \cos(\theta) - \sqrt{n^2 - \sin^2(\theta)}}{n^2 \cos(\theta) + \sqrt{n^2 - \sin^2(\theta)}} e^{-j2k_1 h \cos(\theta) } \right]$	$\omega\mu_0 k_1 m \cos(\phi) \cos(\theta) \cdot$ $\exp\left(-jk_1 h \sqrt{1 - \left(\frac{k_2}{k_1}\right)^2 \sin^2(\theta)}\right) \cdot$ $\left(\frac{2}{ \cos(\theta) + \sqrt{1 - n^2 \sin^2(\theta)}} \right) \frac{e^{-jk_2 r}}{4\pi r}$
E_ϕ	$\omega\mu_0 m k_1 \sin(\phi) \cos(\theta) e^{jk_1 h \cos(\theta) } \frac{e^{-jk_1 r}}{4\pi r} \cdot$ $\left[1 - \frac{ \cos(\theta) - \sqrt{n^2 - \sin^2(\theta)}}{ \cos(\theta) + \sqrt{n^2 - \sin^2(\theta)}} e^{-j2k_1 h \cos(\theta) } \right]$	$-\omega\mu_0 k_1 n m \left(\frac{2 \sin(\phi) \cos(\theta) \sqrt{1 - n^2 \sin^2(\theta)}}{n \cos(\theta) + \sqrt{1 - n^2 \sin^2(\theta)}} \right) \cdot$ $\exp\left(-jk_1 h \sqrt{1 - n^2 \sin^2(\theta)}\right) \frac{e^{-jk_2 r}}{4\pi r}$

Table 12. Compact expression for the far-field of a vertical magnetic dipole above a dielectric interface

Vertical Magnetic Dipole		
	Medium 1 (Air)	Medium 2 (dielectric)
E_θ	0	0
E_ϕ	$\omega\mu_0 k_1 m \sin(\theta) \cdot$ $\left[e^{jk_1 h \cos(\theta)} + \frac{\cos(\theta) - \sqrt{n^2 - \sin^2(\theta)}}{\cos(\theta) + \sqrt{n^2 - \sin^2(\theta)}} e^{-jk_1 h \cos(\theta)} \right] \cdot$ $\left(\frac{e^{-jk_1 r}}{4\pi r} \right)$	$-\omega\mu_0 k_1 m n \left(\frac{2n \sin(\theta) \cos(\theta) }{n \cos(\theta) + \sqrt{1 - n^2 \sin^2(\theta)}} \right) \cdot$ $\exp\left(-jk_1 h \sqrt{1 - n^2 \sin^2(\theta)}\right) \left(\frac{e^{-jk_2 r}}{4\pi r} \right)$

H.) SPECIAL CASES

These expressions for the fields are complicated in the general case, but can be simplified if certain restrictions are applied. First, let us consider the case where $h \rightarrow 0$, that is, the antenna is located infinitely close to the interface. This simplification is demonstrated in Table 13 and Table 14 for the horizontal and vertical magnetic dipoles, respectively.

Table 13. Far field components for a horizontal magnetic dipole very close to a dielectric interface

Horizontal Magnetic Dipole		
	Medium 1 (Air)	Medium 2 (dielectric)
E_θ	$\omega\mu_0 m k_1 \cos(\phi) \frac{e^{-jk_1 r}}{4\pi r} \cdot$ $\left[1 + \frac{n^2 \cos(\theta) - \sqrt{n^2 - \sin^2(\theta)}}{n^2 \cos(\theta) + \sqrt{n^2 - \sin^2(\theta)}} \right]$	$\omega\mu_0 k_1 m \cos(\phi) \cos(\theta) \cdot$ $\left(\frac{2}{ \cos(\theta) + \sqrt{1 - n^2 \sin^2(\theta)}} \right) \frac{e^{-jk_2 r}}{4\pi r}$
E_ϕ	$\omega\mu_0 m k_1 \sin(\phi) \cos(\theta) \frac{e^{-jk_1 r}}{4\pi r} \cdot$ $\left[1 - \frac{ \cos(\theta) - \sqrt{n^2 - \sin^2(\theta)}}{ \cos(\theta) + \sqrt{n^2 - \sin^2(\theta)}} \right]$	$-\omega\mu_0 k_1 n m \left(\frac{2 \sin(\phi) \cos(\theta) \sqrt{1 - n^2 \sin^2(\theta)}}{n \cos(\theta) + \sqrt{1 - n^2 \sin^2(\theta)}} \right) \cdot$ $\frac{e^{-jk_2 r}}{4\pi r}$

Table 14. Far field components for a Vertical magnetic dipole very close to a dielectric interface

Vertical Magnetic Dipole		
	Medium 1 (Air)	Medium 2 (dielectric)
E_θ	0	0
E_ϕ	$\omega\mu_0 k_1 m \sin(\theta) \cdot$ $\left[1 + \frac{\cos(\theta) - \sqrt{n^2 - \sin^2(\theta)}}{\cos(\theta) + \sqrt{n^2 - \sin^2(\theta)}} \right]$ $\left(\frac{e^{-jk_1 r}}{4\pi r} \right)$	$-\omega\mu_0 k_1 m n \left(\frac{2 n \sin(\theta) \cos(\theta) }{n \cos(\theta) + \sqrt{1 - n^2 \sin^2(\theta)}} \right) \cdot$ $\left(\frac{e^{-jk_2 r}}{4\pi r} \right)$

Generally, if one places an antenna on an interface, the contrast in the dielectric constant or material properties is very large. Let us now consider the asymptotic case where $n \gg 1$, that is, $\varepsilon_2 \gg \varepsilon_1$. These new expressions are summarized for the horizontal and vertical magnetic dipoles in Table 15 and

Table 16, respectively.

Table 15. Far field components for a horizontal magnetic dipole very close to a high contrast dielectric interface

Horizontal Magnetic Dipole		
	Medium 1 (Air)	Medium 2 (dielectric)
E_θ	$2\omega\mu_0mk_1\cos(\phi)\frac{e^{-jk_1r}}{4\pi r}$	$\omega\mu_0k_1m\cos(\phi) \cdot$ $\left(\frac{-2j \cos(\theta) }{ \sin(\theta) }\right)\frac{e^{-jk_2r}}{4\pi r}$
E_ϕ	$2\omega\mu_0mk_1\sin(\phi) \cos(\theta) \frac{e^{-jk_1r}}{4\pi r}$	$-\omega\mu_0k_1m[j\sin(\phi)]\left(\frac{n \sin(2\theta) }{ \cos(\theta) +j \sin(\theta) }\right) \cdot$ $\frac{e^{-jk_2r}}{4\pi r}$

Table 16. Far field components for a Vertical magnetic dipole very close to a high contrast dielectric interface

Vertical Magnetic Dipole		
	Medium 1 (Air)	Medium 2 (dielectric)
E_θ	0	0
E_ϕ	0	$-\omega\mu_0k_1m\left(\frac{n \sin(2\theta) }{ \cos(\theta) + j \sin(\theta) }\right) \cdot \frac{e^{-jk_2r}}{4\pi r}$

I.) ORTHOGONAL MAGNETIC DIPOLES

With the far field solutions of both orientations of the magnetic dipole, we can now apply superposition to combine both antennas. Moreover, we will apply a phase offset to the vertical magnetic dipole in form of $e^{j\theta_x}$, where θ_x is the difference in the excitation phase from the horizontal coil. A θ_x of 0 implies they are completely in-phase, whereas a θ_x of π indicates they are completely out of phase. These are shown in Table 17. Note that E_ϕ will form a maximized beam at $\theta = 45^\circ$, because the field components from the horizontal and vertical dipoles add constructively in phase (at $\theta = -45^\circ$, they add destructively and cancel the second beam that was observed from a single magnetic dipole).

Table 17. Field components for combined orthogonal dipoles with a 90 degree phase offset very close to a high contrast dielectric interface

Cross Coil Antenna with 90° Phase Offset		
	Medium 1 (Air)	Medium 2 (dielectric)
E_θ	$2\omega\mu_0mk_1\cos(\phi)\frac{e^{-jk_1r}}{4\pi r}$	$\omega\mu_0k_1m\cos(\phi) \cdot \left(\frac{-2j \cos(\theta) }{ \sin(\theta) }\right)\frac{e^{-jk_2r}}{4\pi r}$
E_ϕ	$2\omega\mu_0mk_1\sin(\phi) \cos(\theta) \frac{e^{-jk_1r}}{4\pi r}$	$\omega\mu_0k_1m\left(\frac{n \sin(2\theta) }{ \cos(\theta) + j \sin(\theta) }\right) \cdot (\sin(\phi) + 1)\frac{e^{-jk_2r}}{4\pi r}$

J.) DIRECTIVITY

The derivation for the fields in the previous section were exclusively for the Far-field or Fraunhofer region. This radiating far-field is taken to begin at radial distances of $r > \frac{2D^2}{\lambda}$, where D is the maximum dimension of the antenna and λ is the wavelength [1]. One typically plots the radiation pattern, showing the relative intensity of the fields, in the far-field of most antennas, as the distance between transmitter and receiver is often $r \gg \frac{2D^2}{\lambda}$. A radiation pattern is a common means of judging the spatial radiation characteristics of an antenna and is defined as “a mathematical function or a graphical representation of the radiation properties of the antenna as a function of space coordinates [1].”

Generally, an antenna engineer is trying to maximize power between a transmitter and a receiver. Basic circuit analysis reveals there is a relationship between power and voltage through the standard power equations: $P = IR = \frac{V^2}{R}$, where P is power, I is current, V is the voltage drop across a given element, and R is the resistance of said element. Logically, this is a simplification of the general case of the Poynting vector, $\vec{S} = \vec{E} \times \vec{H}^*$, where \vec{S} is the Poynting vector, \vec{E} is the electric field, and \vec{H} is the

complex conjugate of the magnetic field. In the far field, the magnitude of the Poynting vector can be approximated by $|\vec{S}| = \frac{|\vec{E}|^2}{\eta}$, where η is the wave impedance [1].

To define directivity, we must first define radiation intensity. The radiation intensity, U , of an antenna is the power radiated by said antenna per unit solid angle (as opposed to radiation density, W_{rad} , which is half of the real part of the magnitude of the Poynting vector). Radiation intensity in the far field is then given by [1]:

$$U = \frac{r^2}{2\eta} \times (|E_\theta|^2 + |E_\phi|^2) \quad (30)$$

To increase the power radiated from an antenna, one can simply put more power into the device. This is hardly efficient, and says very little about the quality of an antenna (any device can be used to transmit at any frequency over any distance if supplied with infinite power, which may destroy the antenna in the process). Directivity is a unitless measurement that compares the power radiated at any specific angle (ϕ and θ) to that of the average radiated power of the antenna. A hypothetical isotropic antenna, which radiates in all directions equally, would have a directivity pattern that was a perfect sphere, with a directivity of 1 everywhere. A highly directive antenna may have a beam with $D \gg 1$ at a certain angle, but areas where comparatively little radiation is produced (so-called “nulls,” where $D \ll 1$). Traditionally, directivity is given by [1]:

$$D = \frac{4\pi U}{P_{rad}} = \frac{4\pi (|E_\theta|^2 + |E_\phi|^2)}{\int_0^{2\pi} \int_0^\pi (|E_\theta|^2 + |E_\phi|^2) \sin(\theta) d\theta d\phi} \quad (31)$$

Unfortunately, this definition does not hold true for a lossy medium. One may recall that the introduction of $\sigma > 0$ will result in a complex wave impedance ζ for either of the radiation media for our dipoles above an interface. The radiated power and radiation density must be completely real and cannot contain an imaginary (reactive) component. Smith provides a slightly different definition for the directivity to take into account the conductive losses. He considers only the radiating power by scaling the

magnitude of the complex wave impedance by its real part. This produces a modified definition of directivity, which must defined separately for region 1 and region 2 [7]:

$$D_i = \frac{\frac{4\pi\text{Re}(\zeta_i)}{2|\zeta_1|^2} \left(|E_\theta e^{jk_i r}|^2 + |E_\phi e^{jk_i r}|^2 \right)}{\int_0^{2\pi} \int_0^\pi \left(\frac{\text{Re}(\zeta_i)}{2|\zeta_1|^2} \left(|E_\theta e^{jk_i r}|^2 + |E_\phi e^{jk_i r}|^2 \right) \right) \sin(\theta) d\theta d\phi}, \text{ for } i = 1, 2 \quad (32)$$

ARBITRARY ORIENTATION OF MAGNETIC DIPOLES

In the previous section, we demonstrated that a 45° beam could be generated by exciting two orthogonal magnetic dipoles 90° out of phase. However, it was initially assumed that these two dipoles would be globally oriented such that they were aligned with the interface (i.e. the medium is parallel to the horizontally oriented magnetic dipole and perpendicular to the vertically oriented magnetic dipole), as seen in Fig. 6a. We wish to show that it is possible to generate this directive beam with any two orthogonal dipoles, regardless of their orientation relative to the interface, as seen in Fig. 6b.

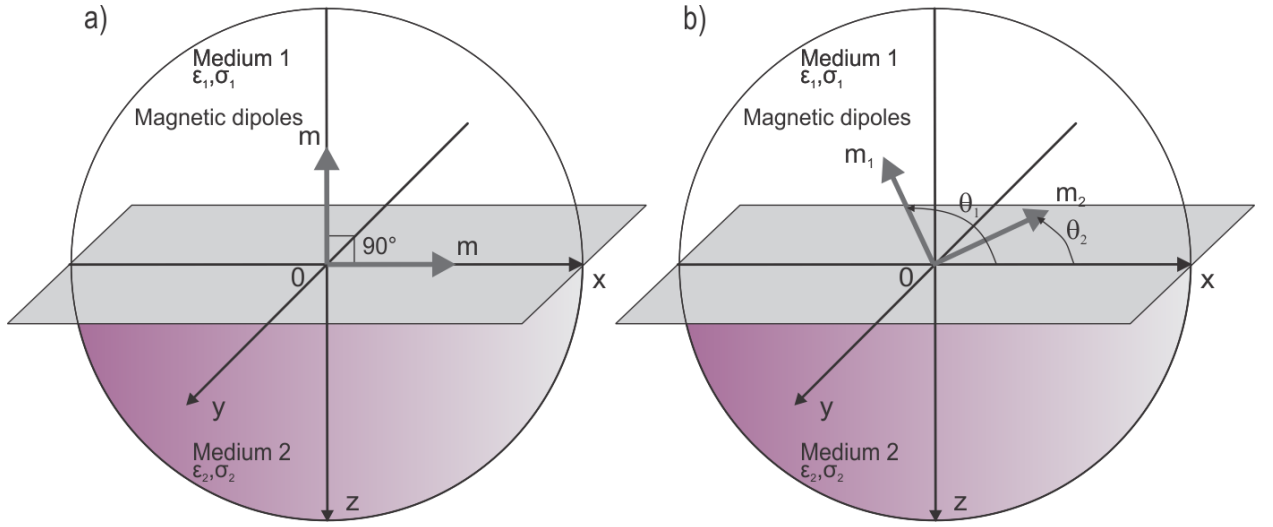


Fig. 6. Orientation of magnetic dipoles above a dielectric interface. a) the proposed orthogonal orientation b) arbitrary orientation

A.) POLARIZATION

The concept of exciting two antennas with a phase offset is not novel. Indeed, it is the foundation of the concept of polarization. Typically, if a reference direction of the polarization of an antenna is not given, one may assume that it is in the direction of maximum gain [67]. Although electromagnetic waves propagate at the same velocity (assuming a uniform medium) in all directions from a source at varying intensities, the excitement of the antenna determines its polarization. Considering the phase of the feed determines how the wave propagates over time, one can describe the polarization to be that of the vector traced by the electric field at a set point in space. Typically, one

usually encounters three general types of polarization: circular polarization, elliptical polarization, and linear polarization. The magnitude of the electric field vector is given by Equation (12) [42].

$$\begin{aligned}
 |\mathbf{E}(z, t)| &= \sqrt{E_x^2(z, t) + E_y^2(z, t)} \\
 &= \sqrt{a_x^2(\cos^2(\omega t - kz)) + a_y^2(\cos^2(\omega t - kz + \delta))}
 \end{aligned} \tag{1}$$

Here, $|\mathbf{E}(z, t)|$ is the electric field magnitude at a point in space z with respect to time t . Viewing the electric field as a planar wave (x-y plane) propagating in the z direction, Equation 3 shows that the magnitude is simply the geometric mean of the separate x and y components. These are represented by the amplitudes multiplied by \cos^2 functions, where ω represents the angular frequency, k is the wavenumber ($k = \frac{\omega\sqrt{\epsilon_r}}{c}$), and δ is the difference in phase between the respective x and y components. This phase difference is typically given in radians, thus if δ is 0, then the two components are perfectly in-phase with one another. When δ is π , they are completely out of phase [42].

Linear polarization occurs when the electric field vectors lie upon a single line throughout time. The UHF antenna in this project will need to be linearly polarized in order communicate with other JTRS users. As one would expect, this can only occur when the horizontal and vertical components of the field are completely in or out of phase. Typically, one can describe this relationship by the inclination angle with respect to the x -axis, as shown in Equation (13). This is the angle formed by the ratio of the vertical components of the field to the horizontal components of the field [42].

$$\Psi(z, t) = \tan^{-1} \left(\frac{E_y(z, t)}{E_x(z, t)} \right) \tag{2}$$

In this equation, $E_y(z, t)$ and $E_x(z, t)$ are the values of the electric field components in the vertical and horizontal directions, respectively, at a certain distance z and time t . However, this angle is not dependent on distance and time, as the vertical and horizontal components of the field will change

correspondingly, thus canceling out z and t in the final inclination angle. This is only true for the linearly polarized case as only the magnitude changes [42].

Another special case of particular interest is circular polarization. Circular polarization occurs when the magnitudes of the horizontal and vertical components of a propagating electric field are equal, but out of phase by a quarter of a cycle. An antenna is Left Hand Circularly Polarized (LHCP) if $\delta = \frac{\pi}{2}$, but it is RHCP if $\delta = -\frac{\pi}{2}$ [42]. One can make an antenna circularly polarized by changing the phase of the feeds such that the phase leading feed moves closer (in phase as opposed to distance) or further from the phase lagging feed [67]. However, opposite that of linear polarization, either direction of circular polarization will have an inclination angle that is a function of time, but the total magnitude of the electric field will remain constant. This can be seen in Equation (14), which applies Equations (12) and (13) to the RHCP case for magnitude of the electric field. Similarly, this is performed with Equation (16) to obtain the inclination angle in Equation (17) for the same RHCP case [42].

$$\begin{aligned} |\mathbf{E}(z, t)| &= \sqrt{E_x^2(z, t) + E_y^2(z, t)} \\ &= \sqrt{a^2(\cos^2(\omega t - kz)) + (-a)^2(\sin^2(\omega t - kz))} \end{aligned} \quad (3)$$

$$|\mathbf{E}(z, t)| = a \quad (4)$$

$$\Psi(z, t) = \tan^{-1} \left(\frac{a(\sin(\omega t - kz))}{a(\cos(\omega t - kz))} \right) \quad (5)$$

$$\Psi(z, t) = \omega t - kz \quad (6)$$

Note the negative sign that is included with the vertical component of the electric field. This is included to show that it is caused by $\delta = \frac{-\pi}{2}$, whereas for LHCP, the only difference would be in

the inclination angle (due to $\delta = \frac{\pi}{2}$), thus becoming $kz - \omega t$. This RHCP case is called “right-handed” because one can curl one’s fingers on one’s right hand to point in the direction of the electric field vector, and the thumb on this hand will be pointing in the direction of propagation. The same rule can be applied to LHCP with the left hand [42].

Circular Polarization can be thought of a special case of the more general elliptical polarization, where the ellipticity angle is $\chi = \pm \frac{\pi}{4}$. The rotation angle is now the angle the ellipse created (by tracing the field in a similar method as that of circular polarization) from a reference axis (typically the horizontal axis), whereas the ellipticity angle determines the curvature of the ellipse and is given by Equation (18) [42].

$$\tan(\chi) = \pm \frac{a_\eta}{a_\xi} = \pm \frac{1}{R} \quad (7)$$

This ratio between the major and minor axes, R , is more commonly known as the axial ratio, where a negative value indicates right hand polarization, and a positive value indicates left hand polarization. It can be used to gauge the shape of the polarization, as it can vary from 1 (circular polarization) to ∞ for linearly polarized antennas. The parameters a_η and a_ξ are taken from the circularly polarized case for horizontal and vertical components; however, for elliptical cases, these are instead used as a measurement of amplitude along the major and minor axes, respectively [42]. It is important to note that these are with reference to the path traced by the electric field and not to the spherical coordinate units (φ and θ) of the far-field radiation sphere, from which one would make measurements. When performing said measurements, one will usually measure the antenna gain from a reference antenna at several tilt angles from the azimuth, where one compares co-polarized gain (the same polarization as the receiver) against cross-polarized gain (the opposite polarization, which one typically wishes to reject). It is a common practice to ensure that the main beam of an antenna is pointed along the polar axis to ensure maximum gain [67].

A natural question to then ask is: “what would happen if there were a polarization mismatch between a transmitter and a receiver?” At first, it may appear as though it would not be accepted, but an antenna does not usually radiate a pure polarization (i.e., a RHCP antenna may have some LHCP components). This energy is lost, and is described by the Polarization Loss Factor (PLF), as seen in Equation (19) [67].

$$PLF = |\hat{p}_w + \hat{p}_a|^2 = |\cos(\psi_p)|^2 \quad (8)$$

In this definition (taken from the perspective of the receiving antenna), \hat{p}_w and \hat{p}_a are both unit vectors to indicate the direction of the electric field. The unit vector \hat{p}_w represents the direction of incoming radiated wave, whereas \hat{p}_a is known as the polarization vector, which is the natural polarization of the receiving antenna [67]. If the two are identical, then there are no losses; however, if they are opposites, then the antenna is completely cross polarized, and in theory, no radiation will be absorbed. The second representation of this is simply a trigonometric version of the two, using the polarization angle between these two vectors, ψ_p [67]. Therefore, it is vital to match the polarization of the transmitter and receiver and an antenna to avoid the high losses associated with polarization mismatch.

B.) ARBITRARY ORIENTATION OF THE MAGNETIC DIPOLES

Typically, antenna engineers are concerned with polarization generally excite electric dipoles with a phase difference. A similar effect can be observed when exciting two magnetic dipoles. Let us assume that these two magnetic dipoles are excited by magnetic moments, \vec{m}_1 and \vec{m}_2 , with corresponding x and y components. Each is excited at an arbitrary phase ϕ_i . The magnetic moments of each of these antennas can then be given by:

$$\vec{m}_1(t) = \begin{pmatrix} m_{x1} \\ m_{y1} \end{pmatrix} \cos(\omega t + \phi_1) \quad (6)$$

$$\vec{m}_2(t) = \begin{pmatrix} m_{x2} \\ m_{y2} \end{pmatrix} \cos(\omega t + \phi_2) \quad (7)$$

By superposition, we can combine these two dipoles:

$$\vec{m}_1(t) + \vec{m}_2(t) = \begin{pmatrix} m_{x1} \cos(\omega t + \phi_1) + m_{x2} \cos(\omega t + \phi_2) \\ m_{y1} \cos(\omega t + \phi_1) + m_{y2} \cos(\omega t + \phi_2) \end{pmatrix} \quad (8)$$

Let us now assume that $|\vec{m}_1| = |\vec{m}_2|$, that is, the magnetic moments are of equal magnitude, but of different directions and excitation phases. Therefore, we can replace this term with m . Furthermore, let us geometrically construct these moments from their normal components, as defined in Table 18.

Table 18. Vertical and horizontal components of two arbitrary magnetic moments

$m_{x1} = m_1 \cos(\theta_1)$	$m_{x2} = m_2 \cos(\theta_2)$
$m_{y1} = m_1 \sin(\theta_1)$	$m_{y2} = m_2 \sin(\theta_2)$

$$\vec{m}_1(t) + \vec{m}_2(t) = \begin{pmatrix} m \cos(\theta_1) \cos(\omega t + \phi_1) + m \cos(\theta_2) \cos(\omega t + \phi_2) \\ m \sin(\theta_1) \cos(\omega t + \phi_1) + m \sin(\theta_2) \cos(\omega t + \phi_2) \end{pmatrix} \quad (9)$$

Next, let us assume that the dipoles are physically orthogonal, that is $\theta_2 = \theta_1 + \frac{\pi}{2}$. This allows us to further simplify our expression for the sum of the magnetic moments:

$$\vec{m}_1(t) + \vec{m}_2(t) = \begin{pmatrix} m \cos(\theta_1) \cos(\omega t + \phi_1) - m \sin(\theta_1) \cos(\omega t + \phi_2) \\ m \sin(\theta_1) \cos(\omega t + \phi_1) + m \cos(\theta_1) \cos(\omega t + \phi_2) \end{pmatrix} \quad (10)$$

To simplify these expression into a more recognizable form, we require one additional assumption: that the phase excitation is exactly 90° out of phase, that is, $\phi_2 = \phi_1 + \frac{\pi}{2}$.

$$\vec{m}_1(t) + \vec{m}_2(t) = \begin{pmatrix} m \cos(\theta_1) \cos(\omega t + \phi_1) + m \sin(\theta_1) \sin(\omega t + \phi_1) \\ m \sin(\theta_1) \cos(\omega t + \phi_1) - m \cos(\theta_1) \sin(\omega t + \phi_1) \end{pmatrix} \quad (11)$$

$$\vec{m}_1(t) + \vec{m}_2(t) = \begin{pmatrix} 2m \cos(\omega t + \phi_1 - \theta_1) \\ 2m \sin(\omega t + \phi_1 - \theta_1) \end{pmatrix} \quad (12)$$

Of course, this can also be written in terms of cosines alone, to explicitly display the 90° shift:

$$\vec{m}_1(t) + \vec{m}_2(t) = \begin{pmatrix} 2m \cos(\omega t + \phi_1 - \theta_1) \\ 2m \cos\left(\omega t + \phi_1 - \frac{\pi}{2}\right) \end{pmatrix} \quad (13)$$

ORTHOGONAL COIL ANTENNAS: ANALYTICAL RESULTS

The previous section outlined the derivation for the far field of an orthogonal coil antenna excited in quadrature. As the antenna approaches the surface of the interface ($h \rightarrow 0$) and the dielectric contrast ($n = \frac{k_2}{k_1} \gg 1$) increases between the media, the antenna forms a focused beam into the lower subspace (the dielectric). This section presents the field patterns that illustrate this affect and explore the sensitivity of this beam to changes in the material properties, distance from the substrate, and excitation phase.

A.)DIRECTIVITY PATTERNS

As stated previously, directivity is one of the main standard performance metrics for antennas, as it indicates which direction the antenna radiates the most power. Naturally, we wish to generate a directed beam through the dielectric medium (e.g. a human body) when we establish a channel. A narrow beam with high directivity limits the amount of “leaked” power to other areas of the medium, that could potentially be reflected and corrupt the received signal. A narrower beam allows for greater resolution, as one can illuminate smaller objects with radiation as opposed to an entire region. Clearly this would be valuable in the case of a medical diagnosis, where the doctor is checking for a small tumor or abnormality. Finally, a high directivity maximizes gain or power transfer to the receiver, thus maximizing the signal-to-noise ratio (SNR) and reducing the error generated by ambient noise in the measurement system.

This section will perform a sensitivity analysis to determine how susceptible to change the radiation pattern and the maximum directivity are to changes in material, geometric, or excitation differences. This will allow an engineer to determine the tolerances of his or her system. For example, one may need to know how much power is no longer radiated into the dielectric medium if the antenna needs to be located at least a few millimeters from the surface.

The two performance criteria that are evaluated here are the maximum directivity, and the power radiated into the second medium. Ideally, both should be maximized to form a narrow beam that propagates through the dielectric. However, the three-dimensional radiation patterns are also shown to

illustrate the beam forming properties of this antenna. An example of the directivity pattern of an orthogonal coil antenna is shown in Fig. 7. This is the basic case where the first medium is a vacuum, and the second medium is a lossless dielectric with an ϵ_r of 10. Note that the z-axis has been inverted for clarity, thus the second medium is located on top (indicated by the yellow, semitransparent rectangular prism).

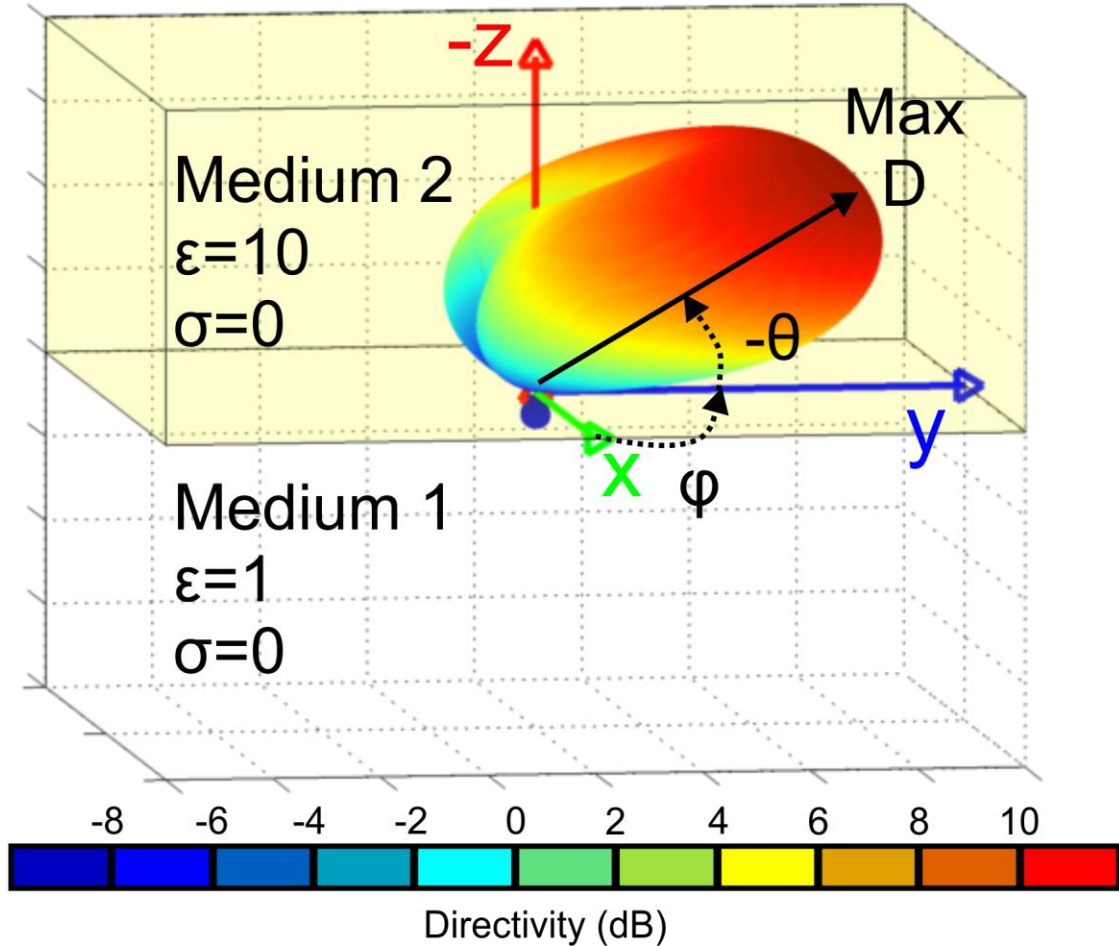


Fig. 7. Example of the Directivity Pattern of Two Orthogonal Magnetic Dipoles

For the purposes of a fair comparison, the above case is considered to be the base case for the antenna. The first medium is always assumed to be air, and the second is always a lossless dielectric with an ϵ_r of 10, unless specified otherwise. Furthermore, the antenna is considered to be directly on the interface ($h \rightarrow 0$), and the orthogonal coils are excited exactly 90° out of phase.

B.)PARAMETRIC ANALYSIS: SENSITIVITY TO CHANGES IN THE DIELECTRIC CONSTANT

In the simplified example, we allowed the dielectric contrast between the media to become very large ($n \gg 1$). This then raises the question: “how high is high enough?” By sweeping ϵ_r of the lower medium (as a control in all of these analyses, the upper medium is assumed to be air), we can establish the relation between the dielectric constant and maximum directivity. Fig. 8 begins to answer this question. There is a sharp discontinuity between the cases where both media are air (i.e. $\epsilon_{r1} = \epsilon_{r2} = 1$), and when the second medium becomes a dielectric. A narrow index of refraction, caused by similar ϵ_r values, will still produce an angled beam, although it is not focused very well. One should also note that the maximum directivity of the vertical and horizontal magnetic dipoles do not need to be equivalent for greater values of the dielectric constant, as they produce completely different patterns in the presence of a dielectric (in air, they are identical). However, as ϵ_r increases past 10~20, the maximum directivity of each antenna type remains constant.

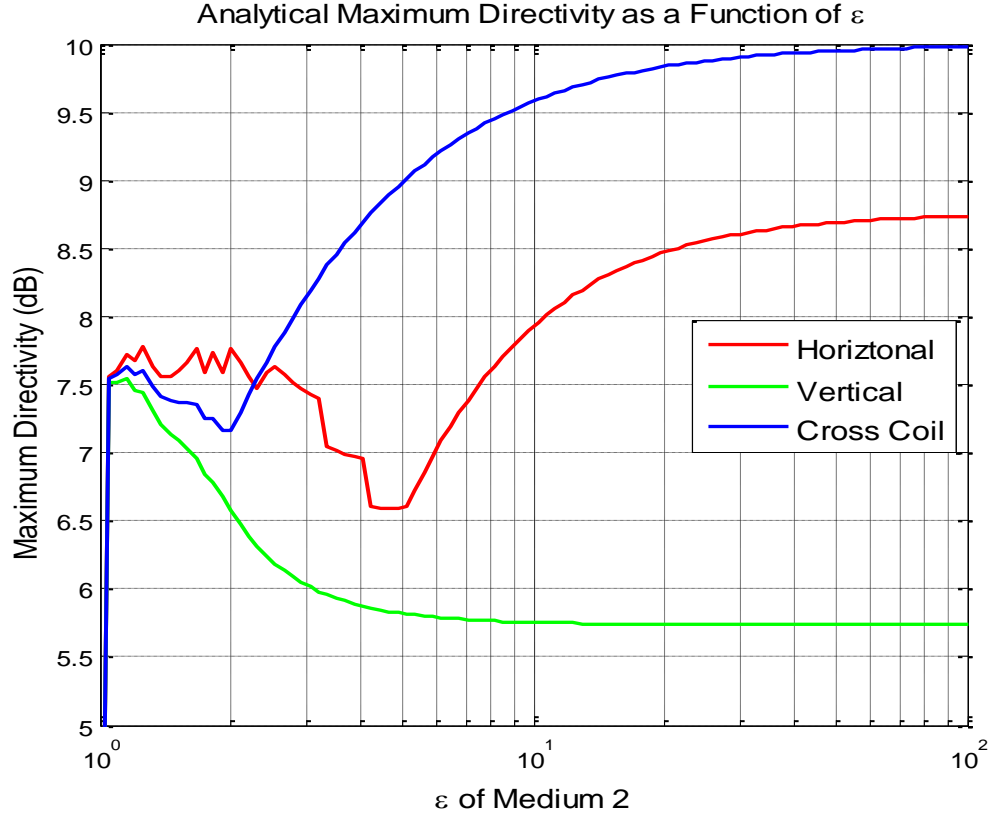


Fig. 8. Analytical Maximum Directivity as a Function of ϵ

Fig. 8 showed that the orthogonal coil antenna clearly had the greatest directivity for large values of ϵ_r . Conversely, Fig. 9 shows that the vertical magnetic dipole radiates more power into the dielectric than either the horizontal magnetic dipole or cross coil designs. As $\frac{\epsilon_{r2}}{\epsilon_{r1}} = n \rightarrow \infty$, all of the power from any of these antennas will be radiated into the dielectric as opposed to the surrounding air. This is generally desirable, as it allows one wishes to penetrate the medium, and any power radiated into the air is wasted. However, even in the case of $\epsilon_{r2} = 10$, more than 95% of the total radiated power propagates through the dielectric medium for the orthogonal coil antenna. Considering that the maximum directivity is also greater than $9.5dB$ at $\epsilon_{r2} = 10$, this is a reasonable candidate for an antenna (the majority of the material properties of the organs being considered in this study have $\epsilon_r \gg 10$).

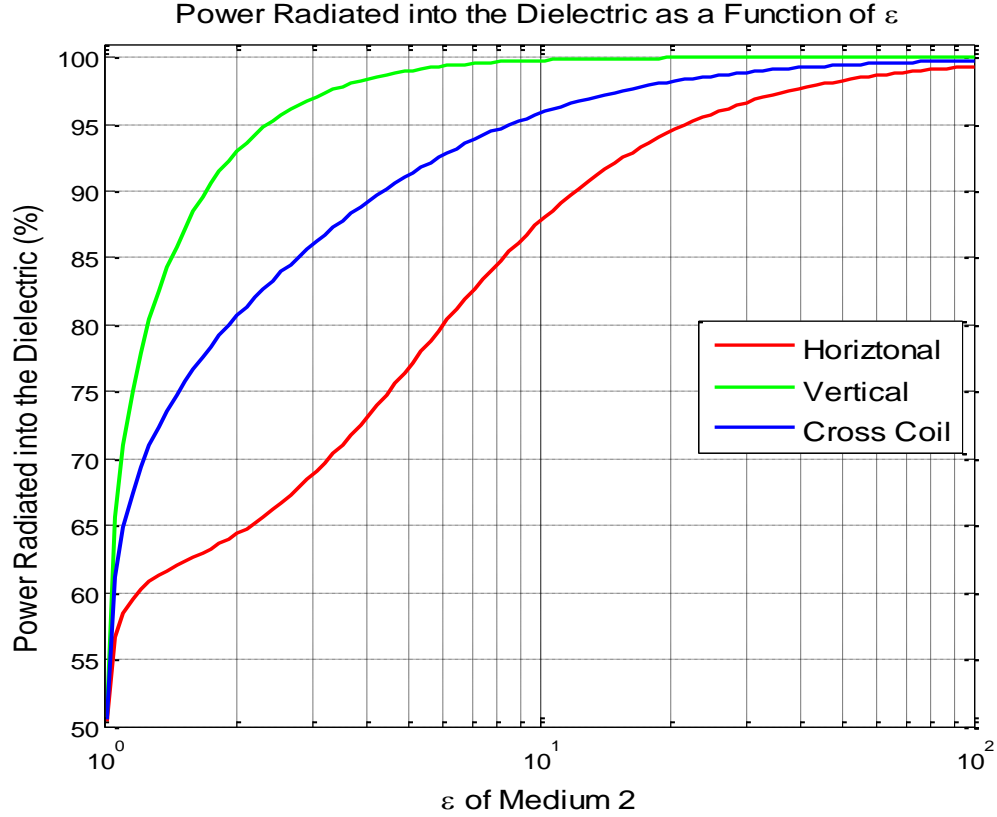


Fig. 9. Power Radiated into the Dielectric as a Function of ϵ

The figures on the following pages show the radiation pattern for the horizontal and vertical magnetic dipoles, as well as that for the combined cross coil antenna (when excited 90° out of phase). In the interests of producing a fair comparison, all other variables are held constant.

Fig. 9 shows the interesting result of having a low index of refraction (i.e. $\epsilon_{r2} \approx 1$). The first row shows the most basic case, which is the lack of a boundary altogether, thus both subspaces are air. This produces the classical pattern of a magnetic dipole or loop in the air, and of course, vertical dipole is simply a rotated version of the horizontal one. A loop in free space is not a directive antenna. However, as ϵ_r increases to 2 or 5, weak lobes are formed. The horizontal dipole has a much larger backlobe in comparison to the vertical magnetic dipole, thus they do not fully cancel one another out in the combined antenna. Moreover, their superposition produces strange patterns, with a thin bowl at the top, as the pattern of the vertical dipole does not widen until higher values of ϵ . This helps generate the sharp

increase in maximum directivity, until it decays and finally rises again (the transition region in Fig. 8, for $\epsilon < 10$).

As previously stated, these low values of ϵ are not very common in the body at 400MHz. Fig. 10 demonstrates the stability of this radiation pattern as the dielectric constant increases from 10 to 100. By a ϵ_r of 10, the horizontal magnetic dipole has formed two clear beams, with minor end-fire lobes at the top. The vertical magnetic dipole forms a hollow cone, which, unfortunately, is not very useful for directing power, as it illuminates a wide circular area. The combined cross coils has a clear, strong beam focused at 45° from the horizon, down into the material. Both the horizontal and combined antennas retain their backlobe, but this is very weak compared to the main beam, and in the case of cross coil antenna configuration, it is unnoticeable ($\max(D) \ll -10dB$) for $\epsilon_r > 20$.

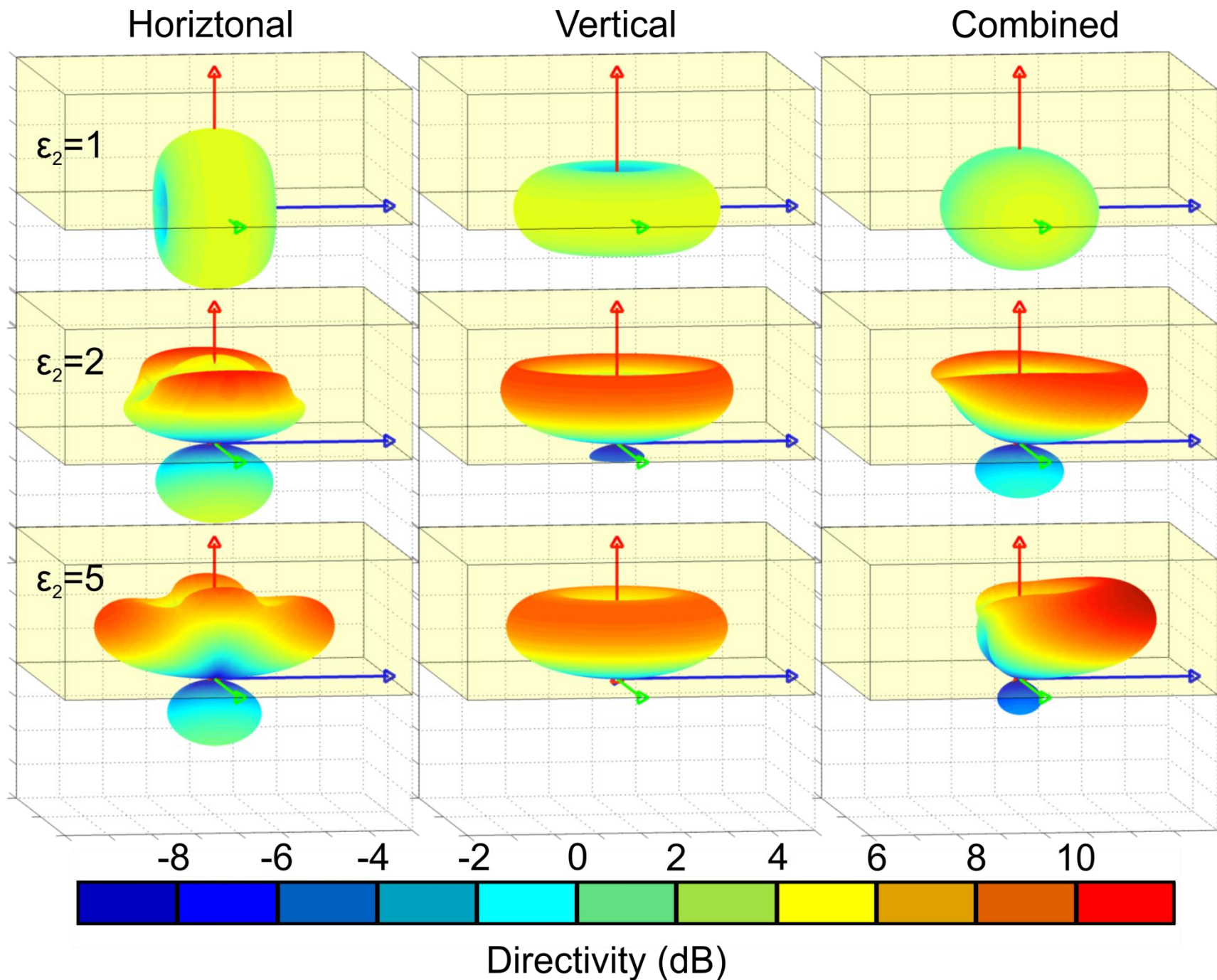


Fig. 10. Directivity Patterns for epsilon=1,2, and 5

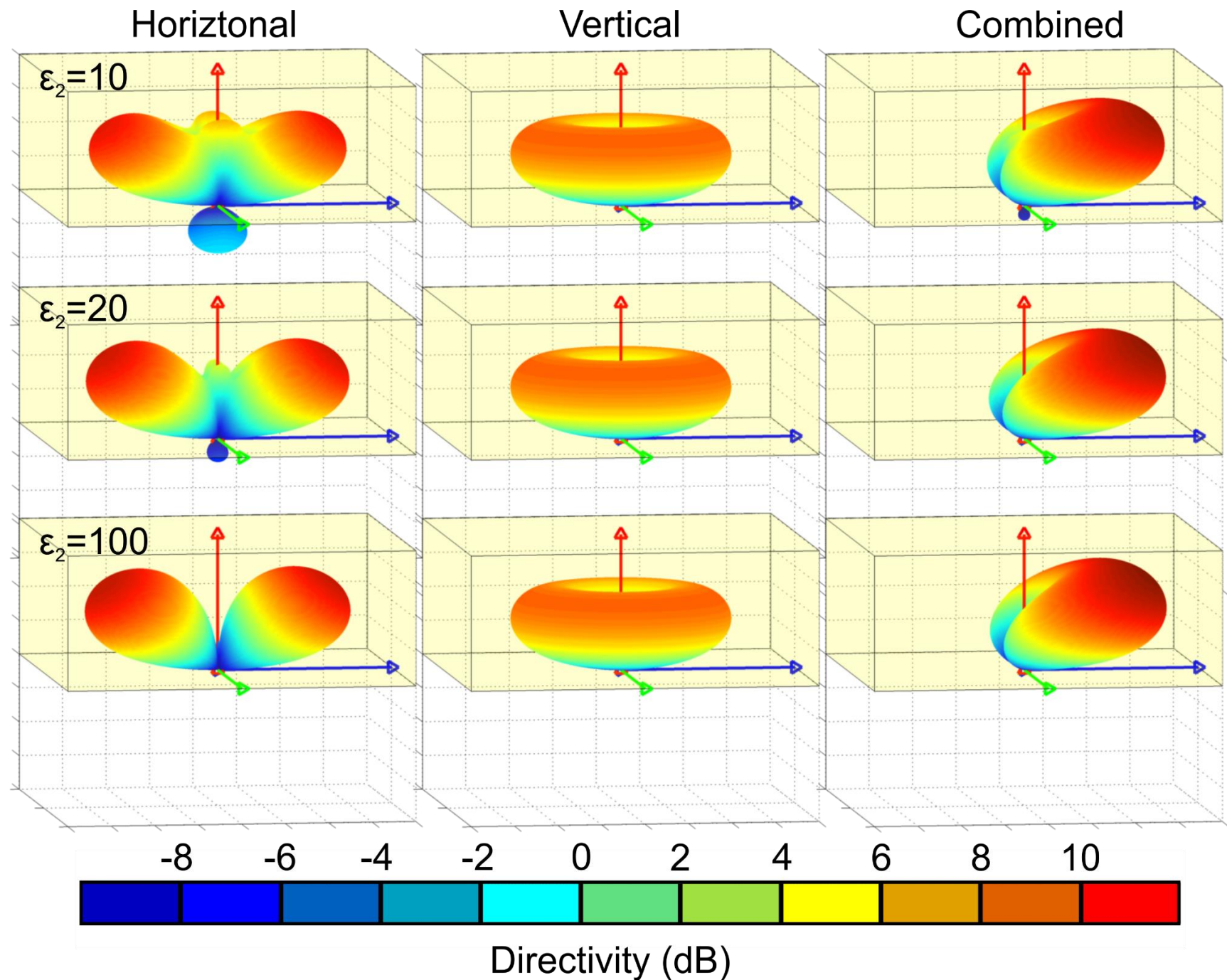


Fig. 11. Directivity Patterns for epsilon=10,20, and 100

C.)PARAMETRIC ANALYSIS: SENSITIVITY TO CHANGES IN THE CONDUCTIVITY

In the previous examples, we assumed the conductivity of both media to be 0. However, perfectly lossless media do not exist in reality. It is therefore logical to perform a sensitivity analysis on this antenna with respect to conductivity to show how σ affects the radiation pattern. Fortunately, the conductivity does not have a large effect on the pattern. Fig. 12 shows that the maximum directivity generally does not change more than 0.5dB for significant changes in σ . Conductivity values greater than $1 \left(\frac{S}{m}\right)$ had no major impact on the maximum directivity.

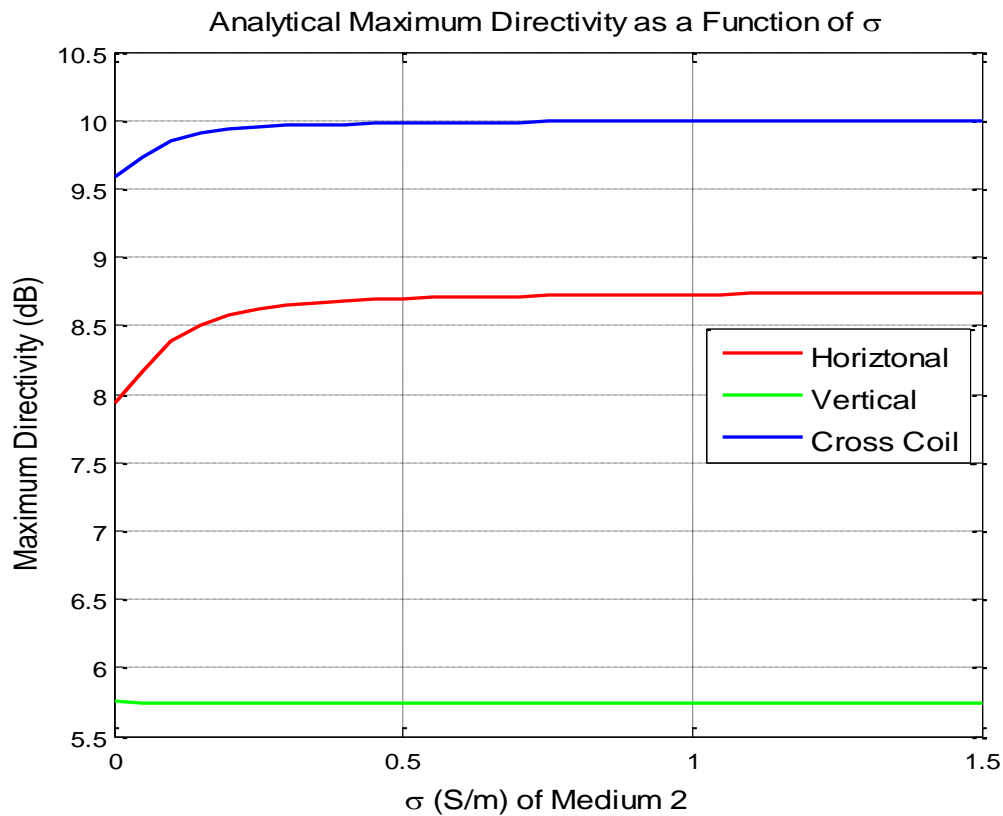


Fig. 12. Analytical Maximum Directivity as a Function of σ

As one might expect, the same pattern was observed in the total radiated power. Fig. 13 confirms that increasing the conductivity of the medium, increases the amount of power that is absorbed by it (One may further take into account the thermal conductivity and volume to determine how quickly the second material will heat due to these losses). The vertical magnetic dipole is nearly unaffected by σ altogether,

whereas a high conductivity will increase the power radiated into the second medium by 4% to 12% for the horizontal and magnetic dipoles, respectively.

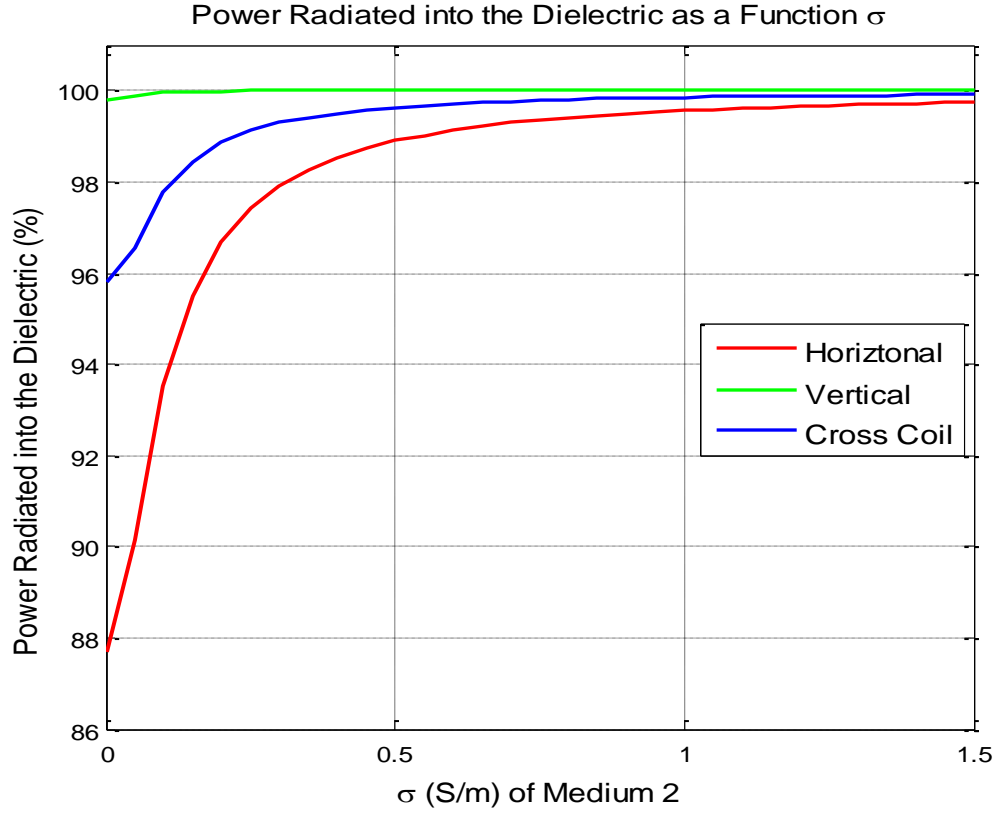


Fig. 13. Power Radiated into the Dielectric Medium as a Function of σ

A similar comparison is performed with the directivity patterns for changes in conductivity as was performed for changes in the dielectric constant; however, the changes are now more subtle. Fig. 14 shows the results of varying σ from 0 to $1\left(\frac{S}{m}\right)$. Beyond this, the changes are almost completely unnoticeable. The horizontal dipole is most affected, as the higher conductivity reduces the two end-fire lobes, which in turn help increase the maximum directivity along the main two beams. These results imply that the conductivity of a lossy transmission medium does not affect the radiation pattern significantly and can generally be neglected from a design standpoint.

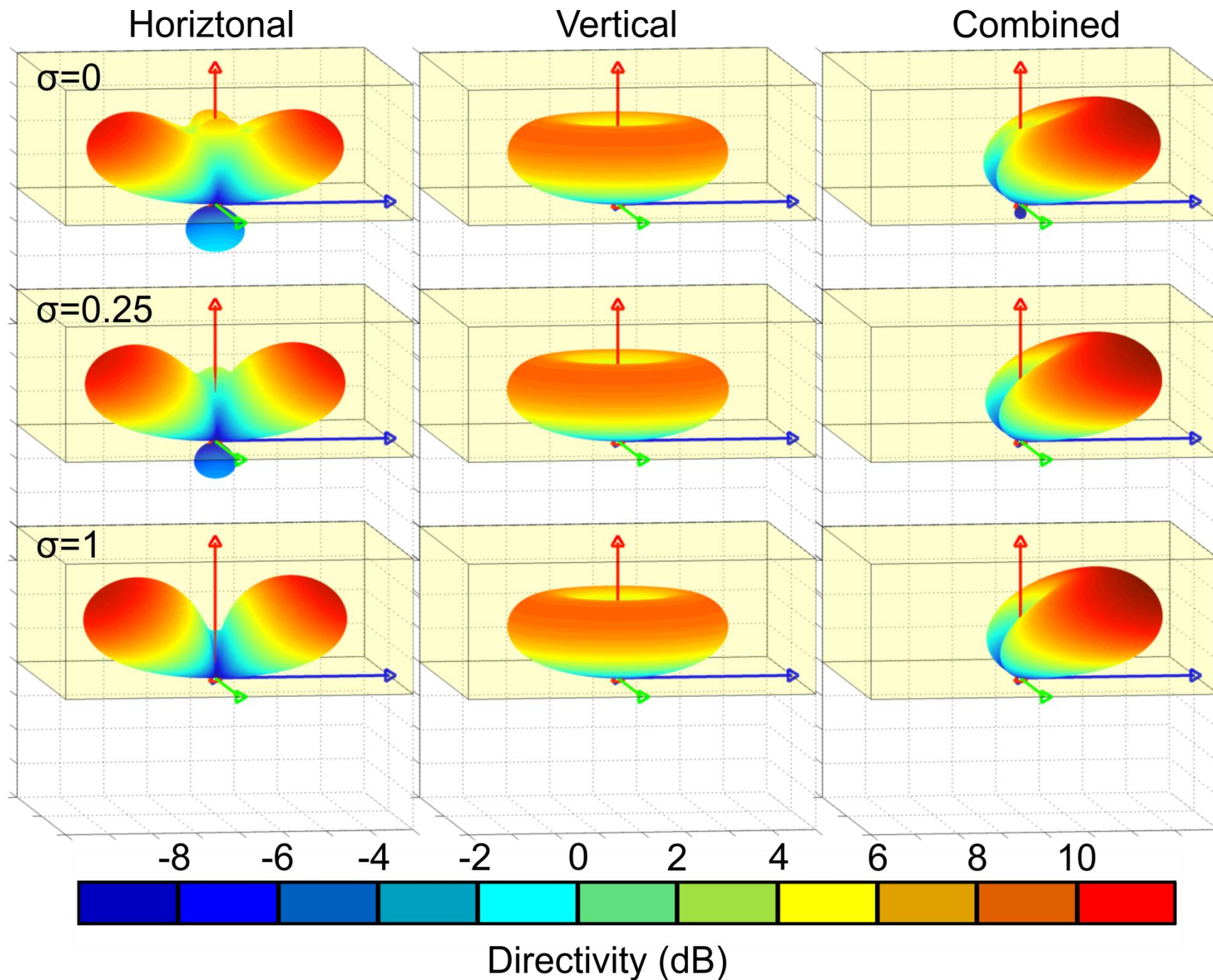


Fig. 14. Directivity Patterns for $\sigma=0, 0.25$, and 1

D.)PARAMETRIC ANALYSIS: SENSITIVITY TO CHANGES IN HEIGHT

Although the general case still holds true, one of the assumptions in the simplified model was that the antenna was located infinitesimally close to the dielectric interface ($h \rightarrow 0$). This is tantamount to placing the antenna directly on the surface of the body. Unfortunately, this is not always possible, as there may be a finite layer of clothing or an intermediate mounting for structural concerns. Therefore, it is of interest to know how sensitive the antenna pattern is to changes in height.

. Fig. 15 shows the maximum directivity as a function of height above the interface. In these examples, the height is given in terms of fractions of a wavelength (calculated in air) as opposed to an absolute distance in meters. This normalizes the scale to be independent of the frequency of operation. At short distances ($h < 0.01\lambda$, which is $\approx 7.5\text{mm}$ at 400MHz), the maximum directivity decays as one increases the height over the substrate. However, the reflections actually can create an increase in maximum directivity at certain extreme distances (e.g. 0.2λ), where it increases by nearly 7dB for the vertical magnetic dipole. This is a case where this particular performance metric fails, as the radiation pattern shows the pattern decays, regardless of the high directivity spike.

Analytical Maximum Directivity as a Function of Height above the Interface

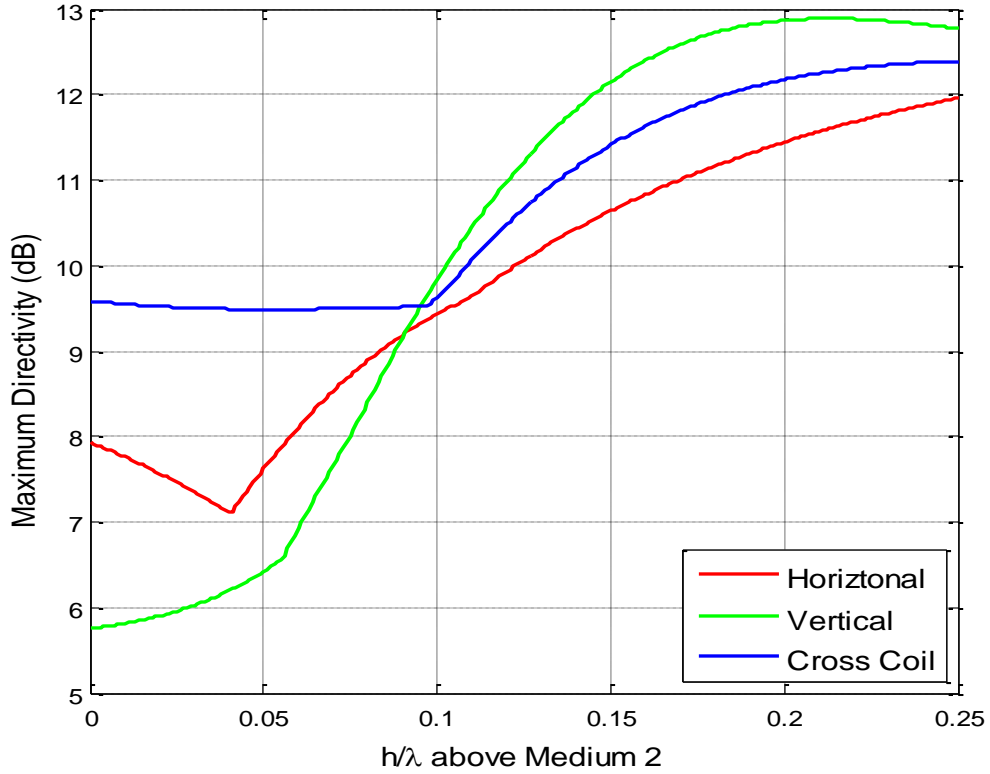


Fig. 15. Analytical Maximum Directivity as a Function of Height above the Interface

Realistically, we are only the region of small height distances ($h < 0.05\lambda$, which is $\approx 37.5\text{mm}$ at 400MHz), as shown in Fig. 15. Placing an antenna greater than this distance from the human body is not practical, and could result in additional interference. Moreover, the radiation pattern shows that the beam has degraded at this point. With small changes in height, close to the dielectric interface, the horizontal and vertical magnetic dipoles do not change more than 1dB, and the cross coil antenna does not degrade more than 0.2dB. This is convenient, as it implies than the person under test would not need the antenna to cut into the surface of their body, and may even comfortably be applied over a thin layer of clothing.

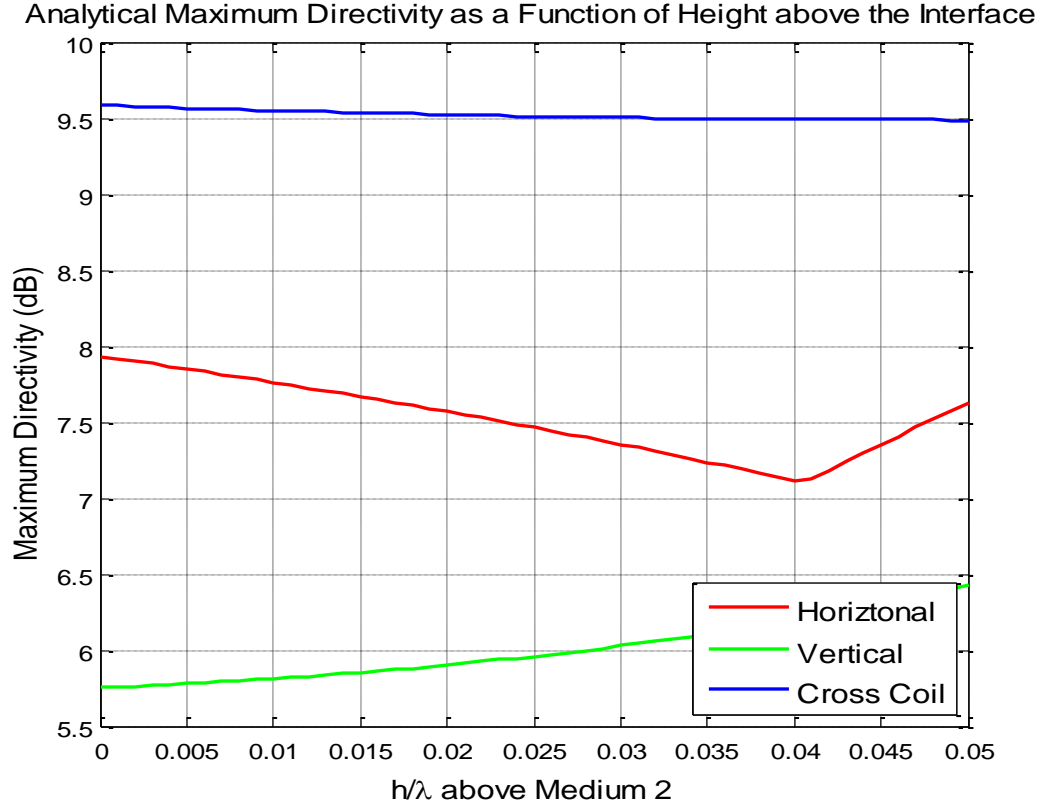


Fig. 16. Analytical Maximum Directivity as a Function of Height above the Interface for small distances

Although Fig. 15 showed an increasing maximum directivity as the antenna was placed further from the body, Fig. 16 shows that the power radiated into the second medium will decay with distance. Logically, this is expected, as the antenna is further from the second medium, thus it is radiating primarily into the air, not into the dielectric. Although the horizontal dipole is affected even at very small distances ($h < 0.05\lambda$), all three antennas appear to decay at approximately the same rate from 0.05λ to 0.2λ , losing about 10%-20% of the power radiated into the second medium for every 0.05λ further the antenna is placed from the interface.

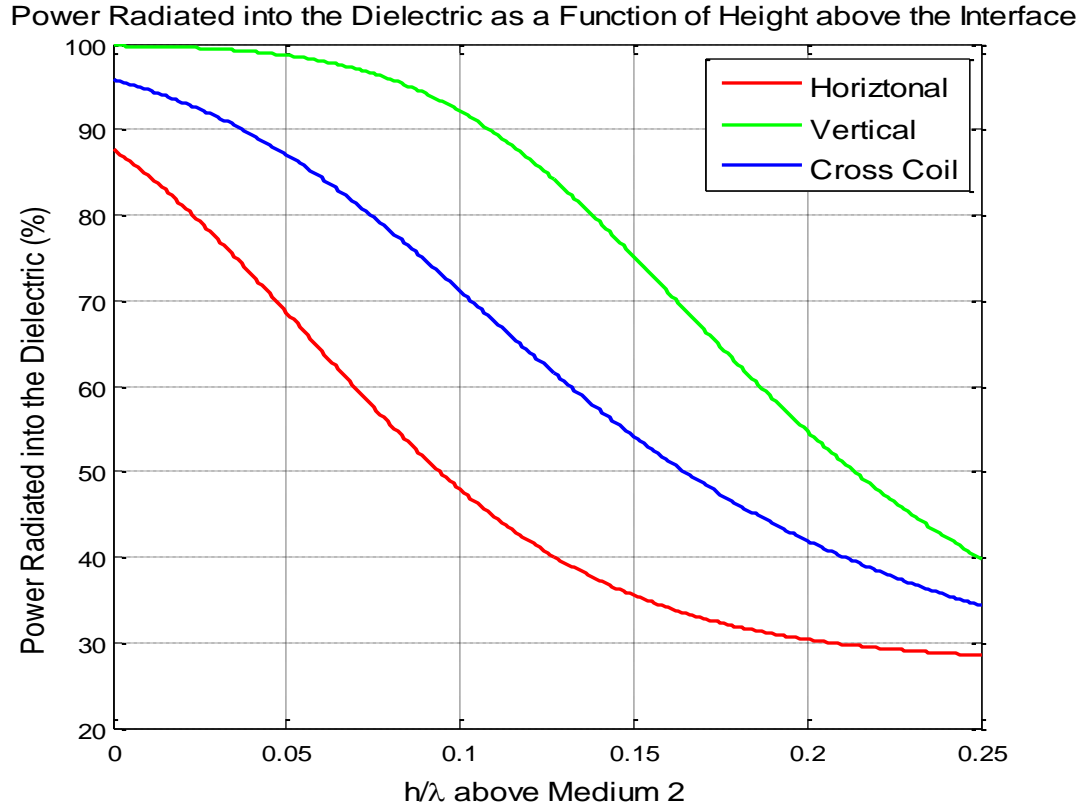


Fig. 17. Power Radiated into the Dielectric as a Function of Height above the Interface

Fig. 17 illustrates how the directivity pattern changes as the height from the interface increases. For the purposes of easy comparison, the material boxes are not shifted and the coordinate system remains stationary. As the distance from the interface increases, the end-fire lobes at the top of the horizontal magnetic dipole become more pronounced as the main two lobes decay. As expected, the backlobe will become increasingly larger as one moves further from the interface. The vertical magnetic dipole is less effected by distance, but also develops sidelobes, and will generate a cusp in its radiation pattern from the reflection from the surface of the interface. As the superposition of the horizontal and vertical magnetic dipoles, the combined antenna suffers both of these affects, generating a widened, lopsided beam with a cusp at endfire.

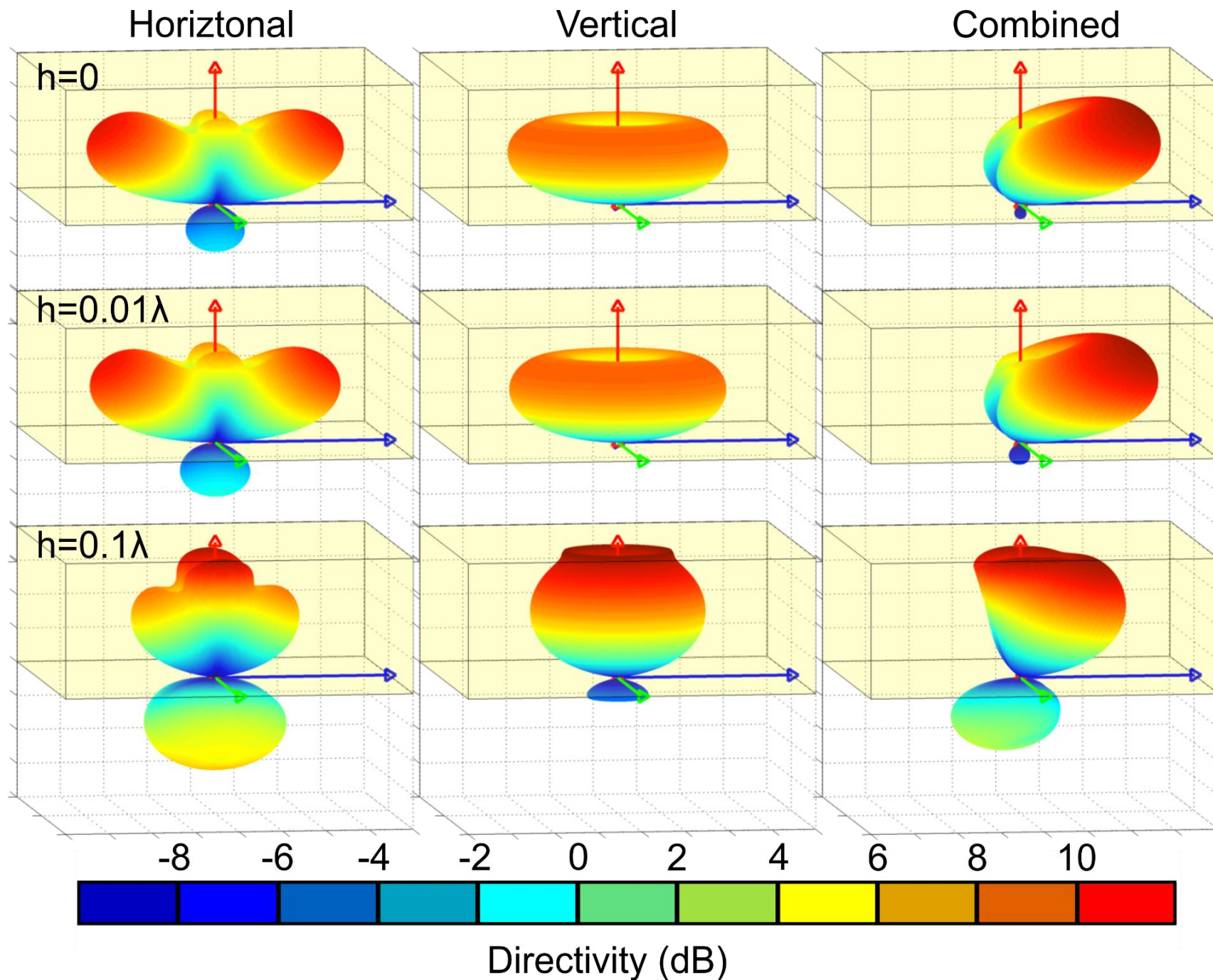


Fig. 18. Directivity Patterns for $h=0$, 0.01λ , and 0.1λ

E.) PARAMETRIC ANALYSIS: SENSITIVITY TO CHANGES IN EXCITATION PHASE

As previously established, for the E_ϕ components in the dielectric to constructively add in one beam and destructively add in the other, one must excite the antenna in quadrature, that is, one antenna must be excited 90° out of phase with the other. This can be accomplished with a 90° hybrid or a $\lambda/4$ transformer. However, these methods are frequency dependent, and it is useful to know the tolerance of this antenna system to inaccuracies in adjusting the phase offset to exactly 90° .

As expected, Fig. 19 confirms that the maximum directivity of the orthogonal coil antenna decays sinusoidally as one deviates from the optimal excitation phase of 90° . Of course, there are two sets of peaks, as one can excite the other direction. Unfortunately, this implies that traditional beam steering, similar to what one would find with a traditional phased array, would be difficult with such an antenna. However, provided one is within 25° of the true 90° phase shift, one can expect to lose less than 0.5dB of directivity.

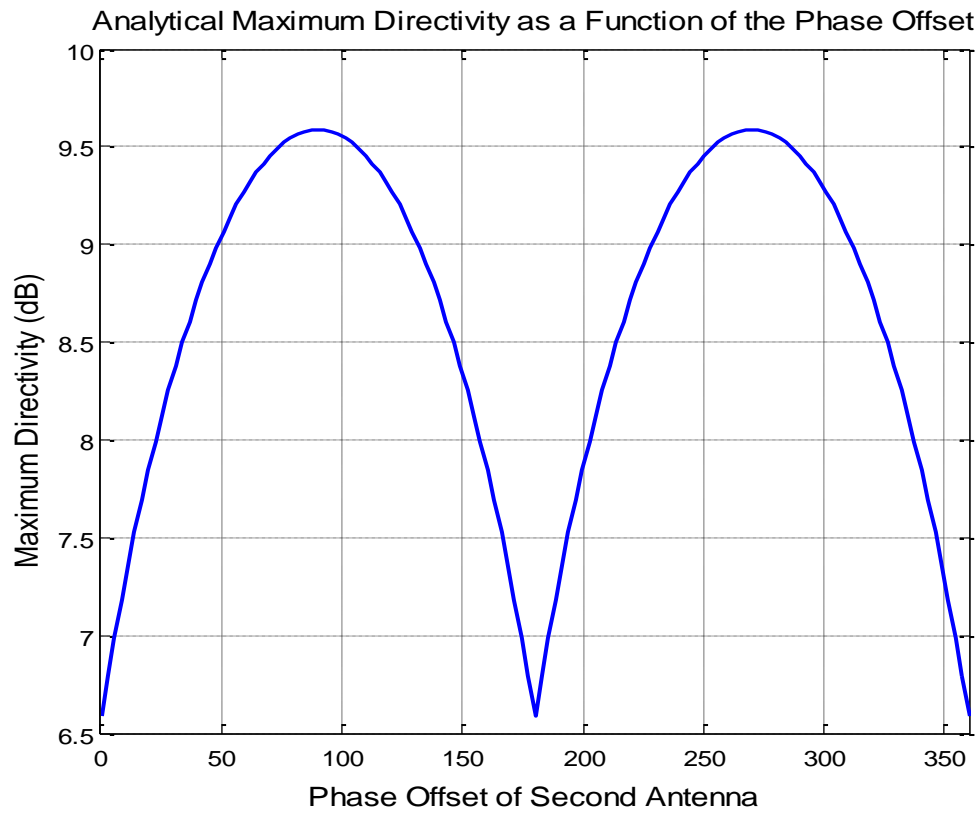


Fig. 19. Analytical Maximum Directivity as a Function of the Phase Offset

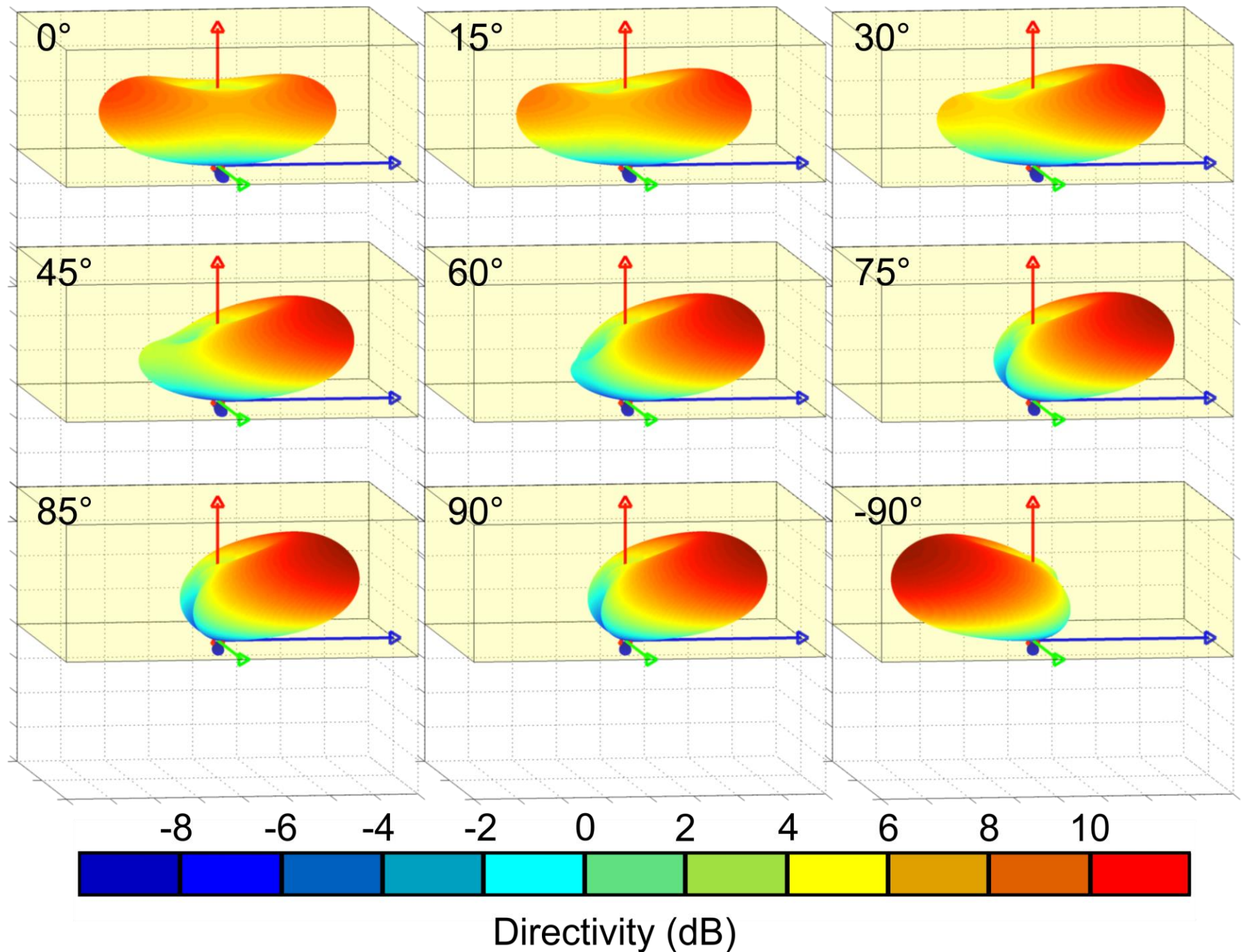


Fig. 20. Directivity Patterns for the Combined Cross Coil Antenna with Different Phase Shifts

Fig. 20 illustrates the radiation pattern for the cross coil antennas for various excitation phase offsets. The horizontal and vertical magnetic dipoles are not shown here, as the phase offset is irrelevant for these two, individual components. If excited exactly in phase (i.e. 0° offset), two symmetric beams are formed, similar to the horizontal magnetic dipole, but in a ring shape in the ϕ direction (the contribution of the vertical magnetic dipole). The beam gradually forms as one increases the phase offset to 90° . Fortunately, there is very little difference between 60° and 90° case (approximately 0.5 dB), which implies a significant tolerance in excitation offset errors. This is very useful, as hybrids and $\frac{\lambda}{4}$ transmission line segments depend on the wavelength. If one uses a different frequency, the wavelength changes, and one must acquire a new hybrid or change the length of the cables feeding the power splitter, such that they are again offset by $\frac{\lambda}{4}$. Having a high tolerance to phase offset errors allows one to effectively have a wider band of acceptable frequencies, or greater manufacturing tolerance.

Unfortunately, the beam cannot be steered by changing the phase, as the two components will only partially cancel one another out. One can, however, excite the antennas -90° or 270° out of phase to produce an identical beam, in the opposite direction. This is simple to configure during testing (one can simply switch the terminals on the power divider or hybrid), but does not provide the ability to scan through multiple angles.

APPLICATIONS OF THE ORTHOGONAL COIL ANTENNA

Previous sections described a novel antenna, the orthogonal coil, which could be excited in quadrature to generate a directive beam through a medium. This medium was abstracted as an arbitrary lossy dielectric; however, it could easily be water, the soil, or even the human body. With the theory behind the antenna established, let us try to generate a channel through the human head using the directive properties of the antenna. The channel will be affected by the material properties of each tissue layer, resulting in reflection and refraction. Ideally, we would like to detect such changes to help establish a diagnosis, but first, we must establish said channel.

Simulations were performed using Ansys High Frequency Structural Simulator (HFSS), a finite element method (FEM) solver. The meshes used to generate the model were constructed from data provided by the U.S. National Library of Medicine [50]. After segmenting and meshing individual organs of the female human head model, the results were imported into HFSS and assigned their respective dielectric constant (ϵ_r) and conductivity (σ), which were obtained from [56]. The frequency dependence of both of these material properties was accounted for in the simulations.

As an extension of the work done in [11] which utilized pulses, the finite element solver in HFSS was used to conduct continuous wave (CW) simulations at specific frequencies. Dispersion is neglected, as it is not relevant in narrowband CW studies (exactly one frequency is used at a time, thus the phase velocity for each frequency is constant). The coils were constructed of 0.4mm thick wire, and were 7mm in diameter. In order to assist in characterizing the human head channel as a transmission medium, the transmitting antenna was positioned around the head in a spherical based coordinate system as shown in Fig. 1. The distance from the center of mass of the head to the center of the coil antennas was adjusted such the edges were approximately 1mm from the surface. This adjustment was necessary because the human head is clearly not a perfect sphere, and the coils were to remain close to but not intersecting the dielectric interface. An example of the antenna used in the simulation is shown in Fig. 21.

At each labeled point in , the antenna was laterally translated (without rotation) and excited in a manner that would direct the beam through the head. The testing points extended from -60° to $+60^\circ$ in steps of 5° in either cut-plane (sagittal YZ and coronal XZ planes) for a total of 49 different testing points.

Only the results for the sagittal plane are considered in this paper, as the coronal plane is more symmetric and did not provide a feasible point to extract the fields.

For brevity, the complete set of calculations is not included in this paper.

Instead, only the most interesting and useful

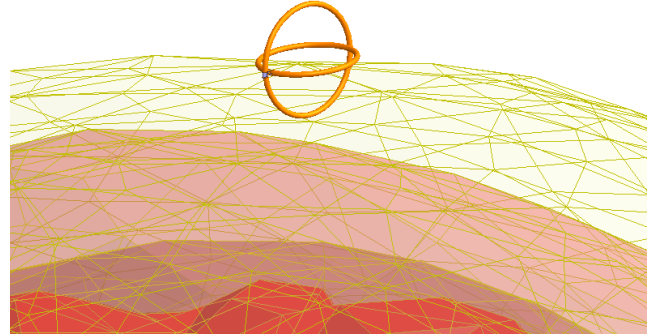


Fig. 21. Close-up view of the two orthogonal loop antennas used in the following simulations. Only the skin, skull, CSF, and brain meshes are shown for clarity

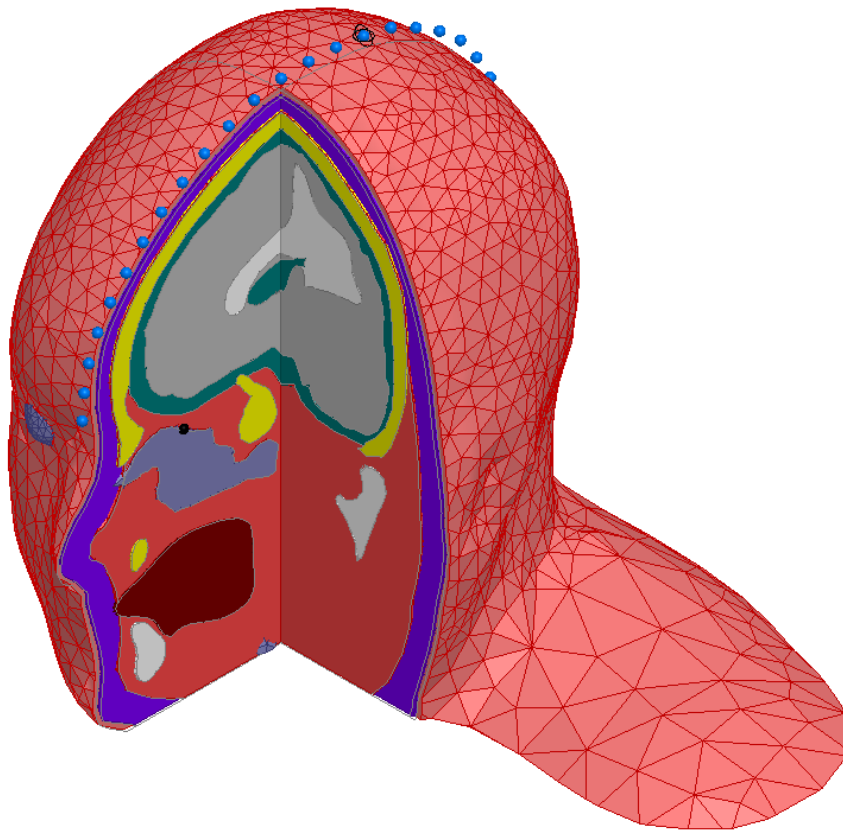


Fig. 22. Section of the surface mesh used in Ansys HFSS simulations of the head. The blue spheres indicate possible TX positions, whereas the black sphere is the location of the receiver.

field plots are displayed. It is important to note that the organs within the human head have a high relative dielectric constant (> 50), which results in a slower phase velocity. This delay is intentionally used in [11]. to remotely detect changes within the body; however, it also scales the magnitude of the received electric field. In order to more easily detect the propagation paths within the head, the Poynting vector ($\mathbf{S} = \mathbf{E} \times \mathbf{H}^*$) is plotted on a logarithmic scale. This shows the direction of power flow and eliminates the oscillating standing waves.

A.)POYNTING VECTOR FOR THE SAGGITAL PLANE

Again, the goal of this study is to establish a channel through the human head. Not only must the power penetrate the head and travel through the brain, it must be extracted. To achieve this objective, two design variables must be optimized: the location measured from the center of the head (given as the angle θ) and the frequency of excitation f . Fig. 23 shows the propagation of power at 100 MHz. At low frequencies the wavelength in free space is over a meter, and even in the brain (with one of the highest dielectric constants of $\epsilon_r = 88.9$ at 100MHz), the wavelength is still greater than 300mm [56]. The resulting Poynting vector plots resemble those of the near field of the orthogonal coils in free space.

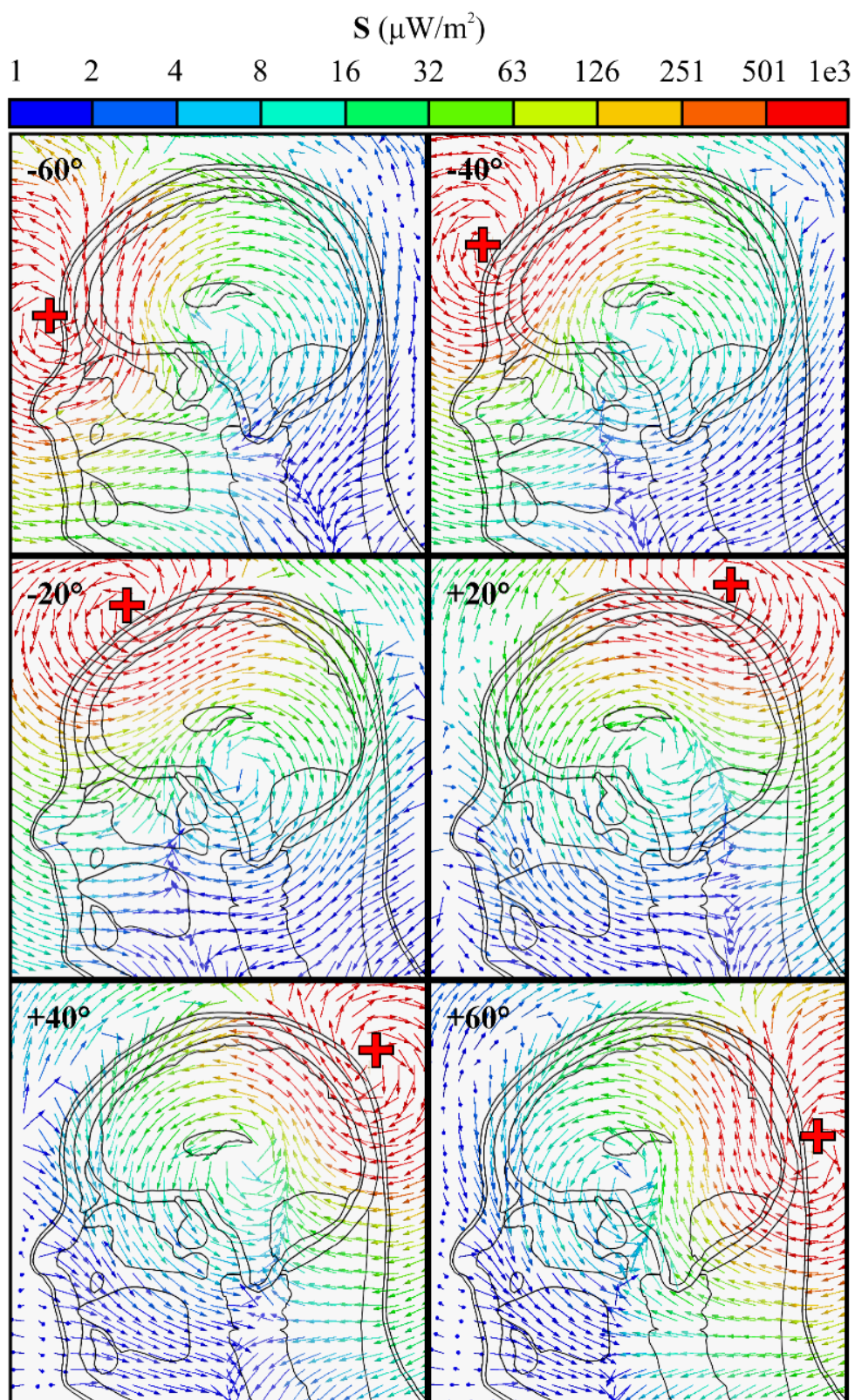


Fig. 23. Magnitude and direction of the Poynting vector for selected antenna positions at 100 MHz. The red crosses show the locations of the transmitter (the size is exaggerated for clarity).

Mid-range frequencies, such as 500 MHz, cause the wavelength to be closer to the Fresnel region and allow the antenna to demonstrate the targeted directive pattern described in [39], as seen in Fig. 24. The CSF, with $\epsilon_r = 70.1$ and $\sigma = 2.28 \frac{\text{S}}{\text{m}}$ at 500 MHz, begins to act like the walls of a waveguide around the brain [56]. Depending on the direction of excitation, this effect steers the beam along the inner contour of the brain to either the cerebellum or the sinus cavity. Unfortunately, at higher frequencies the difference in ϵ causes a much larger angle of refraction at the sinus(air)/muscle interface, making the field more difficult to recover.

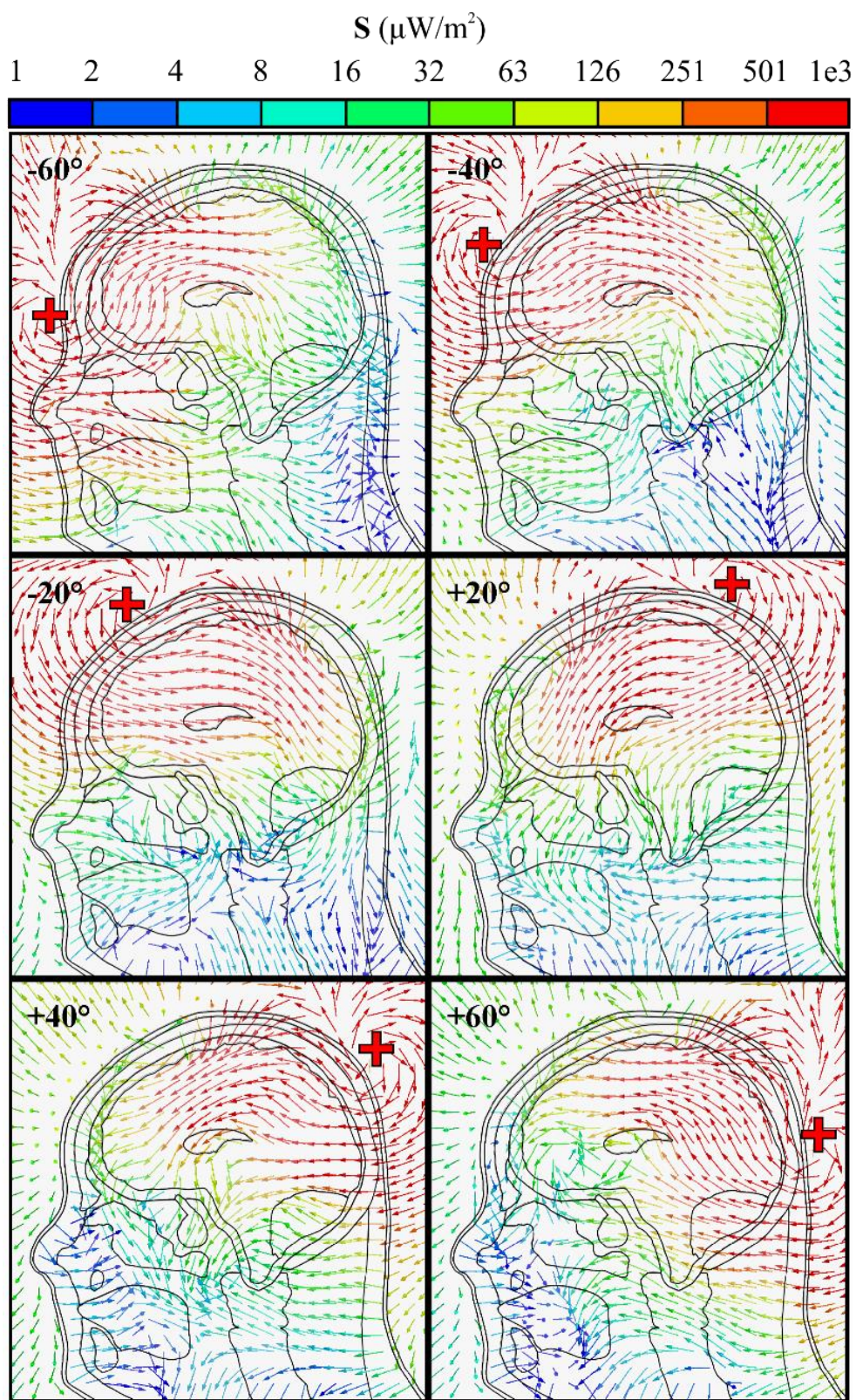


Fig. 24. Magnitude and direction of the Poynting vector for selected antenna positions at 500 MHz.

As one increases the frequency, the problems observed in Fig. 24 begin to escalate. Fig. 25 illustrates the Poynting vector for the orthogonal coils being excited at 1 GHz. The 45° beam is still clearly present, albeit curved by the aforementioned waveguide effect of the CSF, but reflections from this boundary begin to eliminate the propagating component of the wave. This cancellation would make signal extraction very challenging, as there is little to no forward propagating power through the brain that exits the head.

The quantity of multipath at 1 GHz suggests that through use of signal processing techniques one could obtain more information from the reflections. CW signals contain only one frequency (the excitation frequency), and thus do not suffer from dispersion. However, if the wave encounters a phase shifted version of itself (due to reflections), superposition dictates that it could constructively or destructively combine. A wideband signal takes advantage of frequency diversity and the dispersive effects of the channel to reconstruct the original signal. This is a traditional signal processing technique, but it introduces further complications and limitations, and it is not applicable to narrowband signals.

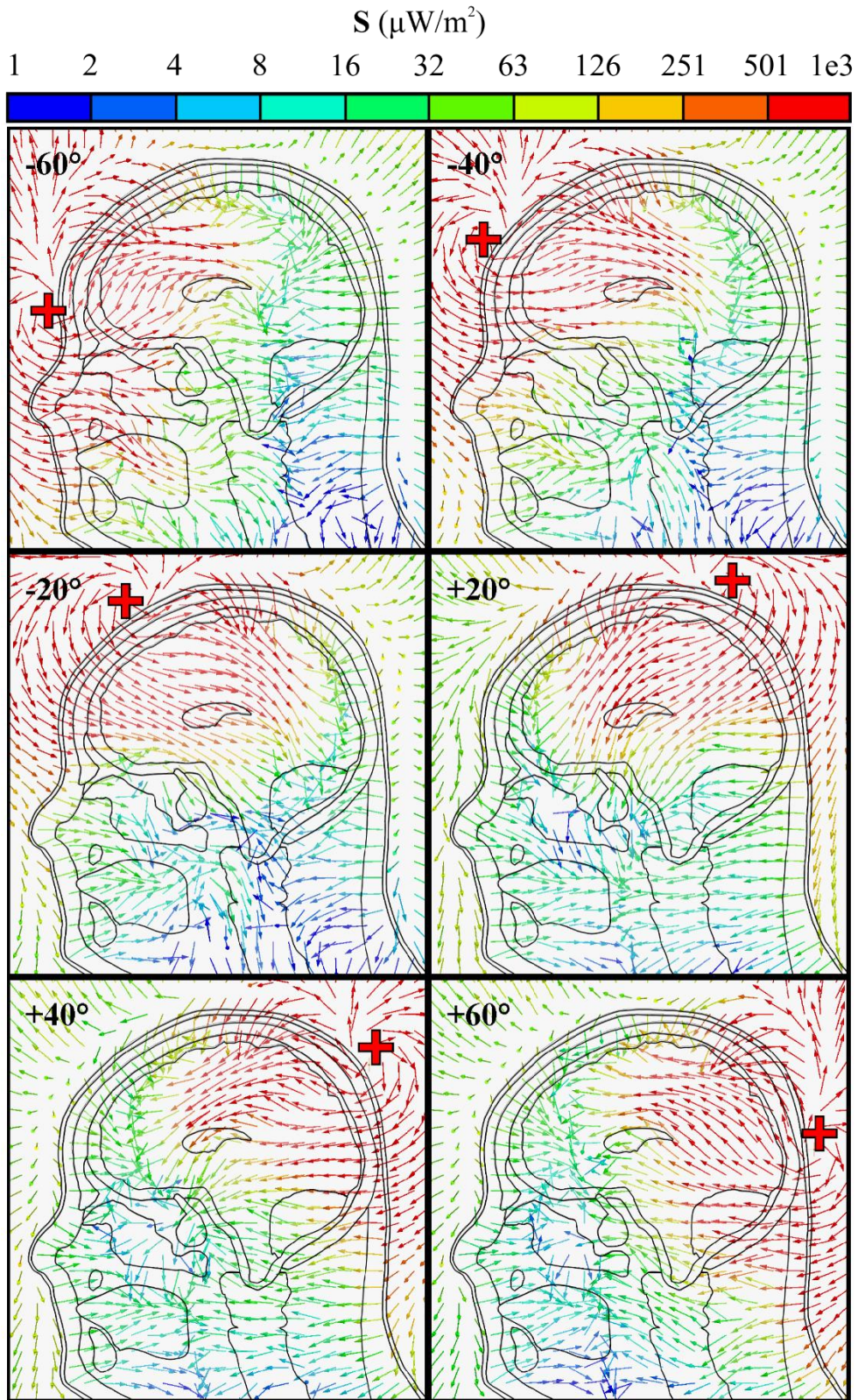


Fig. 25. Magnitude and direction of the Poynting vector for selected antenna positions at 1 GHz.

B.) ESTABLISHING A PROPAGATION CHANNEL THROUGH THE BRAIN

The ideal transmission channel would propagate through a long path within the brain and be received with the maximum power transfer through this path. A longer propagation path through the brain will experience a greater effect in attenuation and phase velocity due to abnormalities in the material properties in the brain. Furthermore, increasing this length would help negate the effects the short distances required to enter or leave the brain. Clearly, maximizing the power received (i.e. concentrating the beam) allows one to more easily observe these changes in the presence of noise.

This now becomes an optimization problem, where one must maximize the path length through the brain without compromising received power. A test point was selected on top of the sinus to measure the received fields. Although similar study could be preformed with a more practical receiver on the tongue, the sinus cavity destroys all paths to the tongue at higher frequencies.

The transmitting coils were moved from $\theta = -60^\circ$ to $+60^\circ$ in steps of 5° at a constant distance of approximately 1mm to the surface of the head, as depicted in Fig. 22. At each transmission point the fields were simulated for excitations from 100 MHz to 1 GHz in steps on 100 MHz. The magnitude of the Poynting vector at the test point shown in Fig. 27 is summarized in Fig. 26(a).

The disproportionately large magnitudes near -60° in Fig. 26(a) are caused by the caused by the close proximity of the transmitter on the front of the head and the test point in the sinuses. These values are less relevant as there is virtually no path through the brain. Near $+15^\circ$, the magnitude reaches a local plateau between -40dB and -35dB before sharply dropping. Fig. 27. Magnitude and direction of the Poynting vector for an antenna placed at $\theta=+15^\circ$ at selected frequencies., is an example of poynting vector field for an antenna located at this position. One may note that the high intensity is caused by the waveguide properties of the CSF channeling the power into the sinus cavity at frequencies between 200 MHz and 600 MHz. Higher frequencies at this position begin to suffer from reflection, reducing the magnitude of received Poynting vector.

Fig. 26(b) plots the path length through the brain on the same axes as Fig. 26(a). We define the propagation path to exclusively be the curved distance (following the vectors), not the perpendicular distance, from the transmitter to the test point. Each distance was graphically calculated using vector plots

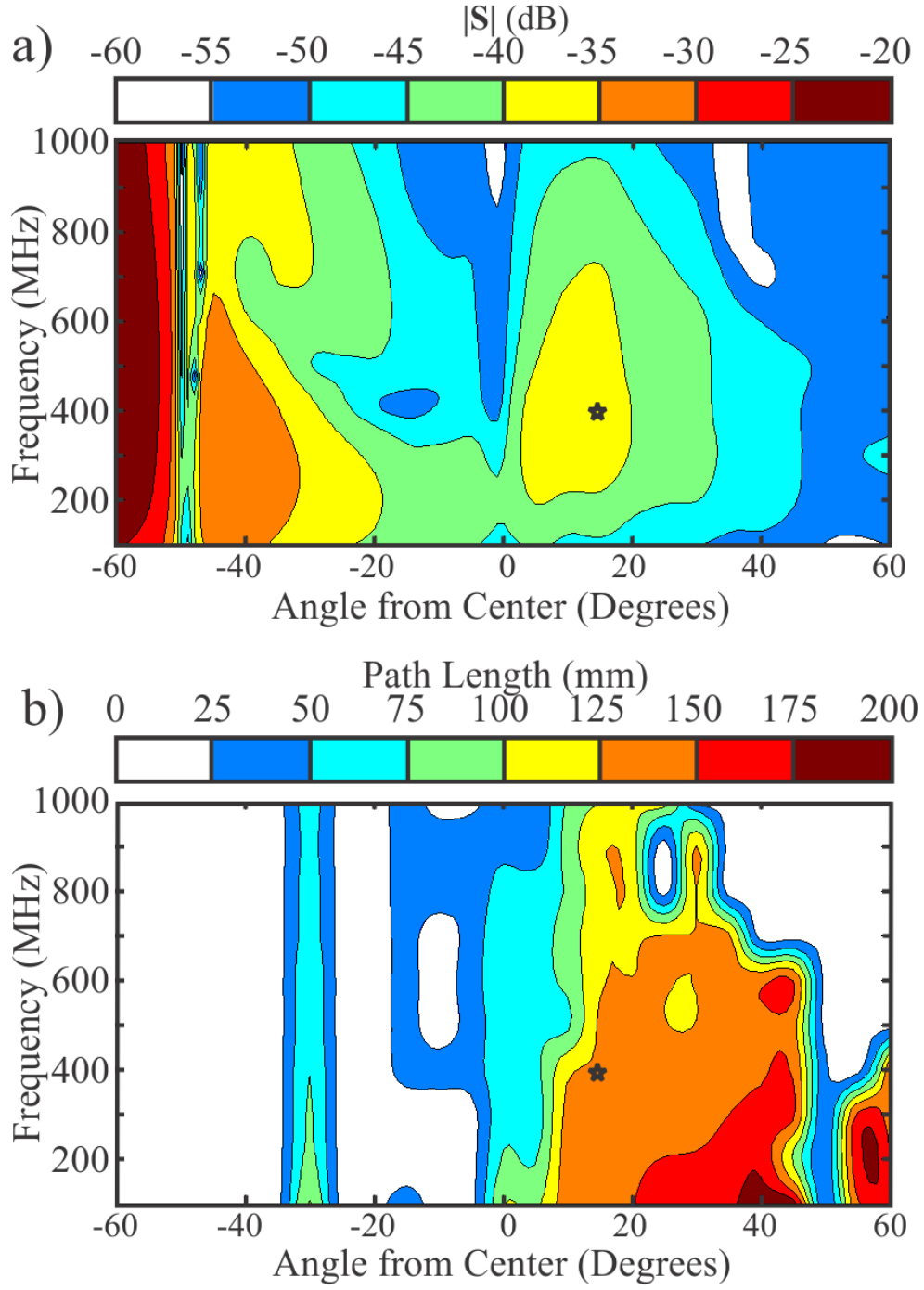


Fig. 26. a) Magnitude of the Poynting vector evaluated at the test point above the sinus cavity as shown in Fig. 27 for different excitation positions and frequencies. b) The length of the path of power propagation through the brain. The star indicates the selected optimal compromise in maximising the received power and propagation distance through the brain (at $\theta = +15^\circ$ and $f = 400 \text{ MHz}$).

such as those in -Fig. 27. Only the portion of this curve that is inside the brain is considered, and cases that did not have a path from the antenna to the test point via the brain were discarded as having a path length of 0.

The optimal location and frequency for the transmitter is problem dependent, as one must find a compromise between a long propagation path through the brain and high received power. We selected the starred point in Fig. 26. a) Magnitude of the Poynting vector evaluated at the test point above the sinus cavity as shown in Fig. 27 for different excitation positions and frequencies. b) The length of the path of power propagation through the brain. The star indicates the selected optimal compromise in maximising the received power and propagation distance through the brain (at $\theta = +15^\circ$ and $f = 400 \text{ MHz}$). (at $\theta = +15^\circ$ and $f = 400 \text{ MHz}$), where $|\mathbf{S}| > -40 \text{ dB}$, and the path length through the brain is at least 125mm. Other transmitter locations and frequencies produced a shorter path, or the received power was too low to be feasibly measured with noise.

The largest obstruction to the signal path is the sinus cavity, as it has the greatest dielectric contrast ($\epsilon_r = 1$ for air, but $\epsilon_r \approx 57.1$ at 400MHz). Moreover, the sinus cavity can be filled with mucus, or the swelling of the surrounding tissue can change its shape. Although the original concept was to place the receiver on the tongue, the large angle of refraction at the sinus cavities makes this course of action very unreliable. By injecting the receiver to the roof of the sinus, the signal can be extracted with minimal distortion from the aforementioned variations. This can greatly reduce the number of materials that can change, thus isolating fluctuations in the material properties of the brain.

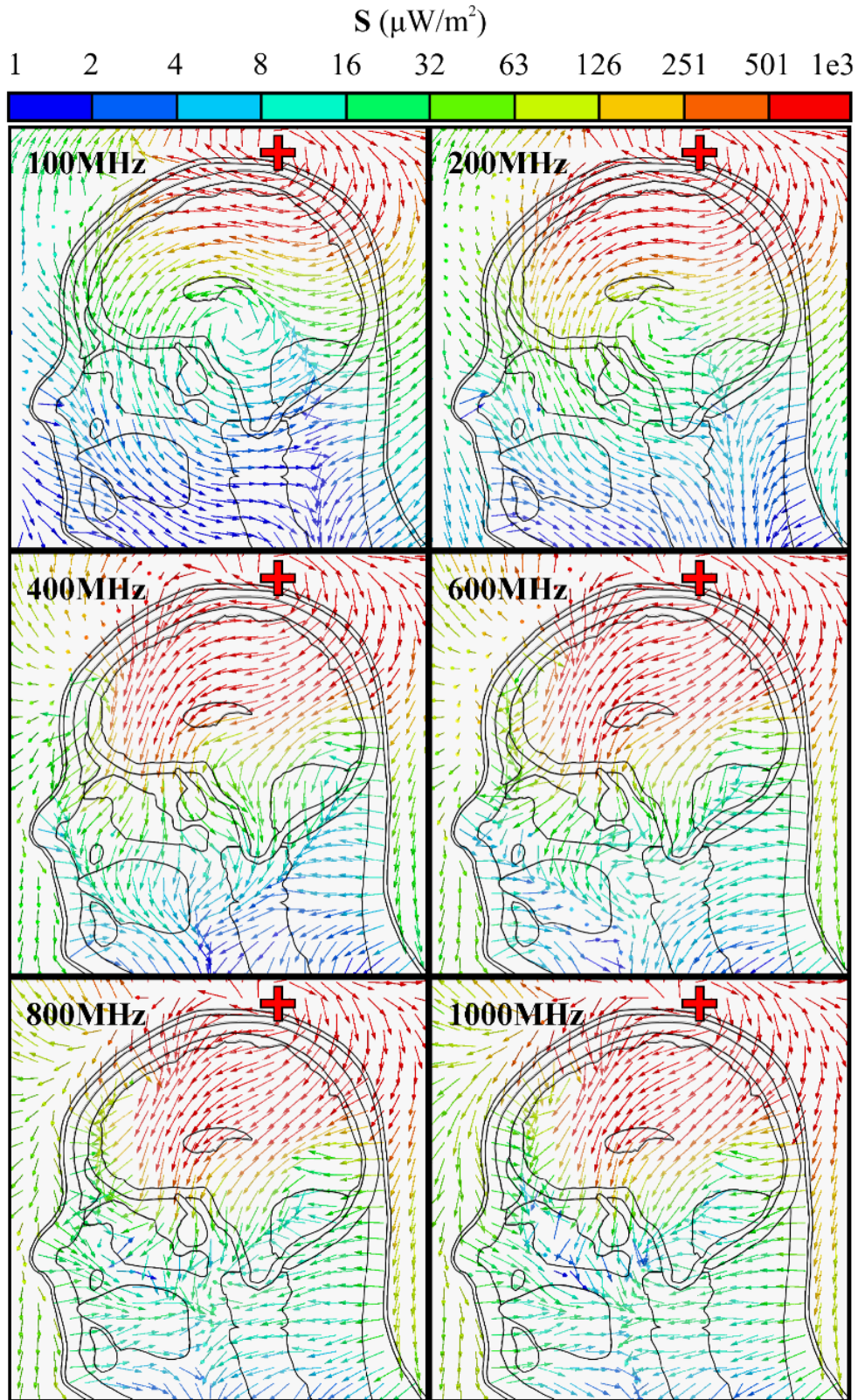


Fig. 27. Magnitude and direction of the Poynting vector for an antenna placed at $\theta = +15^\circ$ at selected frequencies.

C.) VALIDATION USING PULSES AND FDTD

All of the previous results were performed using finite element method (FEM) simulations with a single frequency continuous wave (CW). Prior to these simulations, pulse-based microwave signals were simulated using an older version of the VHP model with fewer organs, shown in Fig. 28 [11]. The goal of this study was similar in nature: to detect changes in the material properties of the cerebrospinal fluid (CSF). CSF is viscous liquid that protects and nourishes the brain. A medical professional can extract CSF from a patient in a fairly dangerous procedure called a “spinal tap,” which involves drawing this fluid close to the brain stem.



Fig. 28. Combined low-resolution mesh for the Visible Human Body Project (female)

Doctors can test the CSF for glucose levels, cell counts, supernatant color, latex agglutination, and other medically important characteristics. A study showed that the dielectric constant is approximately 10-20% greater for individuals with hepatic encephalopathy meningitis, and encephalitis at 2.683GHz [68]. This was due to a change in glucose or protein levels. Moreover, another recent study showed that the one may be able to detect Alzheimer's disease (AD) before the symptoms manifest themselves [69]. The CSF supplies amino acids to the brain. A team of researchers found a close correlation between concentrations of two of these proteins, β -Amyloid protein 1-42 ($A\beta$ -42) and CSF phosphorylated tau_{181P} (P-Tau_{181P}), and the development of AD up to 10 years before the first symptoms begin to develop. Clearly there is a need to non-invasively test for the presence of these proteins to help diagnosis AD in its early stages.

The same orthogonal coil antenna is placed above the head. As stated previously, this antenna will form a directive beam into the dielectric when the coils are excited in quadrature. A finite difference time domain (FDTD) simulation of the coil above a dielectric shown in Fig. 29. Note that in the H-plane, the waves propagating towards port 3 add destructively and cancel, whereas the waves toward port 4 add constructively. This results in the concentrated 45° beam.

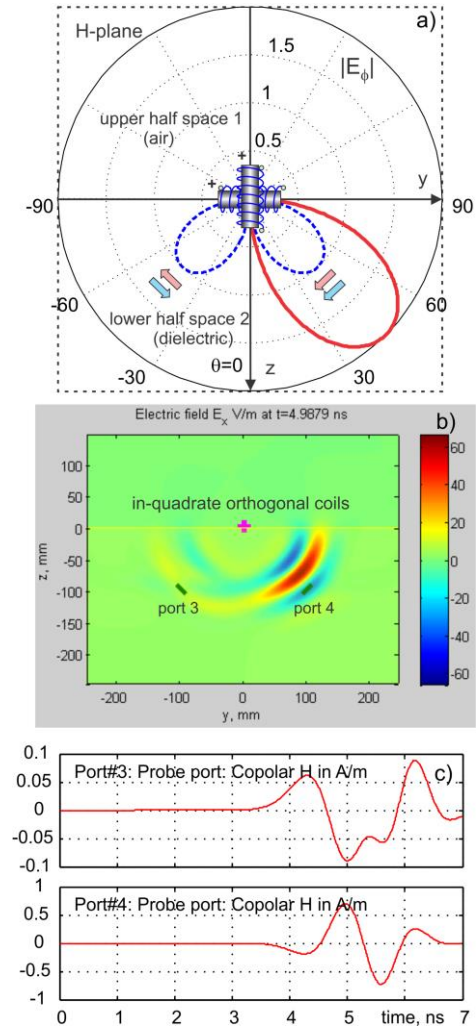


Fig. 29. Orthogonal-coil antenna used at the simulations: a) concept; b) Operation at the top of a lossy dielectric half-space, c) Magnetic field at the probe location in

Before using our refined VHP model and frequency dependent material properties from IT'IS [56], static values at for the dielectric constant and conductivity were collected from various sources. The dielectric constant and conductivity were only recorded at 400MHz and assumed to remain constant over the width of the pulse. These values are summarized in Table 19.

Table 19. Electrical data of biological tissues at 400 MHz, [41] used at the simulations as nominal values.

Biological Tissue	Permittivity (ϵ_r)	Conductivity (σ , S/m)
Brain	49.7	0.59
Cerebral Spinal Fluid (CSF)	71.0	2.25
Skin	46.7	0.69
Skull	17.8	0.16
Spinal Cord	35.4	0.45
Jaw Bone	22.4	0.23
Tongue	57.7	0.77
Eye Tissue	57.7	1.00
Teeth	22.4	0.23

Each magnetic dipole (small coil) was excited with a time-varying current source in the form of a Rayleigh pulse [11]:

$$i(t) = \frac{I_0(t_0 - t)}{\tau} \exp\left(-\frac{(t - t_0)^2}{4\tau^2}\right), \quad t_0 = 5\tau, \quad f_c = \frac{0.16}{\tau}, \quad (33)$$

where I_0 is maximum current ($I_0 = 1A$ was selected for simplicity), f_c is the center frequency, and τ determines the bandwidth of the pulse. Center frequencies of 400MHz, 800MHz, and 1600MHz were examined with corresponding pulse delays of 0.4ns, 0.2ns, and 0.1ns, respectively. The resulting electric field for each case is plotted in Fig. 30.

The first row of Fig. 30 shows the electric field propagating through the head at 400MHz as time progresses. The volumetric wave propagating through the brain is clearly the most dominant feature, although there is some multipath as the wave reaches the outer surface of the combined skin-fat layer. Note that the secondary lobe is still present, albeit much weaker than the main lobe, as the body is not a perfect dielectric.

The second row shows the electric field at 800MHz. The wavelength is becoming shorter and the attenuation is more noticeable at higher frequencies, resulting in a quickly decaying wave. This attenuation makes signal extraction more challenging for higher frequency excitations. However, one may

notice the appearance of a surface wave that is decoupled from the volumetric wave. This surface wave propagates mostly only skin/air interface, and carries little information regarding the brain.

The final row illustrates the effects of increasing the center frequency to 1.6GHz. In addition to increased attenuation, the aforementioned surface wave becomes more dominant than the volumetric wave. Observing this last row more closely reveals that increasing the frequency also increases the multipath components, as expected.

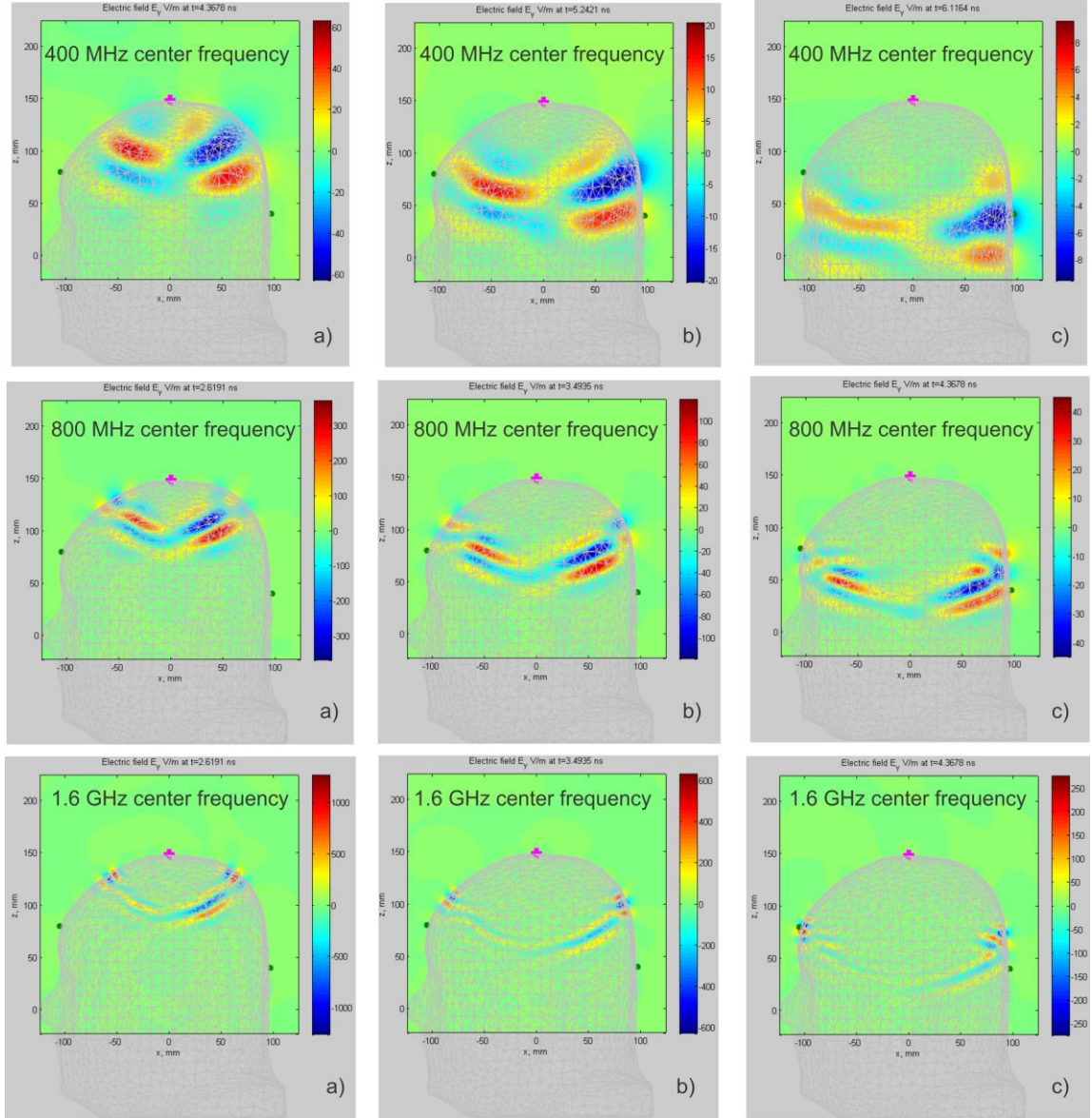


Fig. 30. Evolution of the pulse signal (dominant co-polar electric-field component is shown) within the human head at 400MHz, 800MHz, and 1600MHz center frequency. Only the outer shape of the human head is shown.

Fig. 31 demonstrates the resulting signal from a receiver placed on the back of the head if the dielectric constant of the CSF varied by approximately $\pm 15\%$. The diffraction pulse through the air does not pass through the body at all, and is completely unaffected by the change in the CSF. Furthermore, an increased dielectric constant reduces phase velocity, thus the diffraction pulse arrives at the receiver significantly earlier than the volumetric wave.

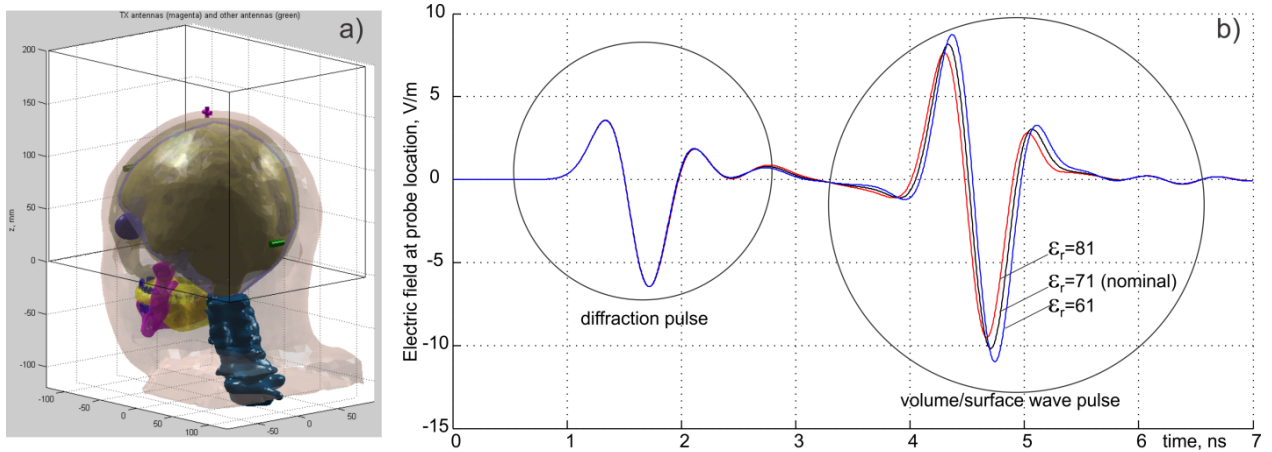


Fig. 31. a) - Orthogonal-coil antenna on top of the head excited at 400MHz and two small orthogonal receiving dipoles (or field probes; b) - The copolar electric field at one receiver location (on the back of the head). The received voltage signal for a small

The volumetric wave shares the same general shape as the original transmitted pulse. The spreading is caused by the wave diffracting off of the internal tissue layers, resulting in heavily attenuated and slightly delayed “echoes” to appear. Observing Fig. 31 closely, one may notice the phase shifts between the different test cases. These correspond to the different phase velocities determined by the dielectric constant. Moreover, the amplitude will slightly fluctuate due to the shift in the angle of refraction, such that the receiver is no longer centered.

These simulations showed that one could find use an orthogonal coil antenna to excite a beam through the head, thus finding a change in CSF properties through the correlation of the signal from nominal CSF and that of the patient. Unfortunately, this method has several uncertainties, such as inconsistencies in skin composition between tests (e.g. the patient may have varying degrees of dry or wet skin), consistent placement of the TX and RX antennas, and adapting the configuration to different body shapes.

D.) RF SIMULATIONS ON A HUMAN FEMUR MODEL: PRELIMINARY RESULTS

We use a section of the Ansys Human body model, as seen in Fig. 32. This coronal plane is the main testing plane for all of the following results, as the sagittal plane suffered too many reflections from muscle tissue to have a beam penetrate through the femur. Two orthogonal coil antennas (i.e. magnetic dipoles) were excited in quadrature to generate a directive beam into the body.

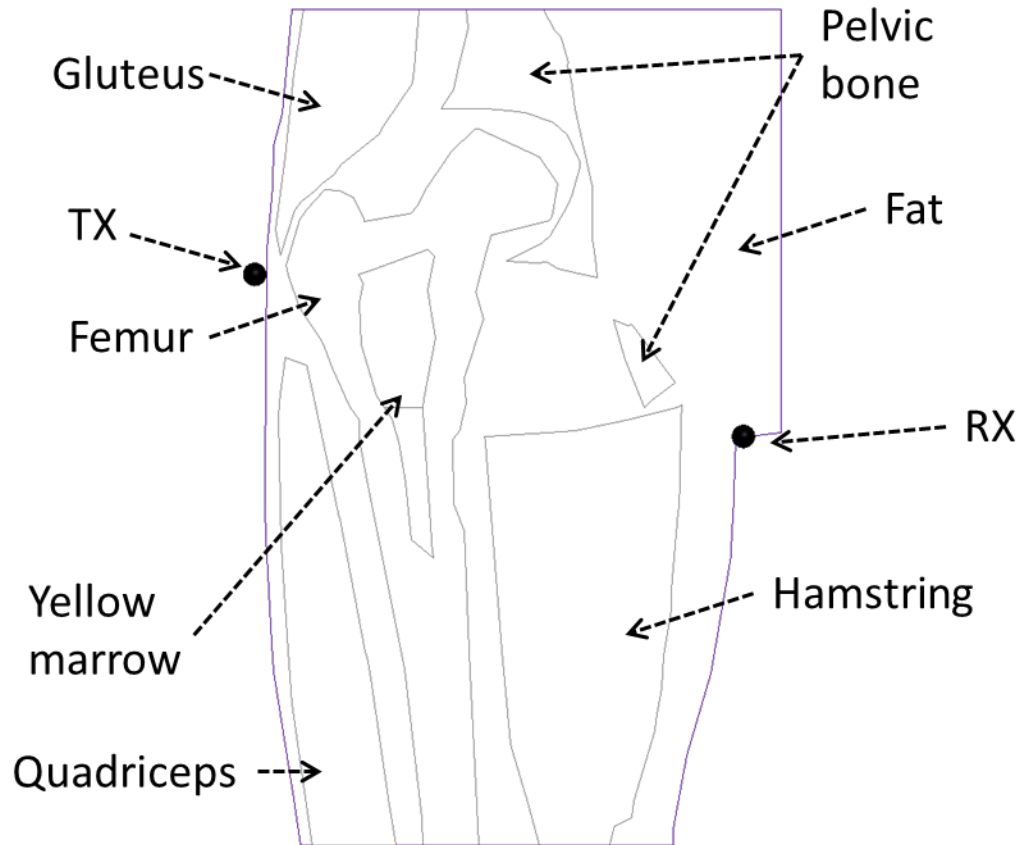


Fig. 32 Leg and hip from the Ansys Human Body Model

We compared two extreme cases that are displayed in Fig. 33. One image is an extremely osteoporotic case, with the majority of the femur consisting of Bone marrow (~18.8% of the total femur volume). This is compared to a “normal” femur with only ~7.4% of the total femur volume consisting of bone marrow. The marrow replaces the volume normally occupied by cancellous bone.

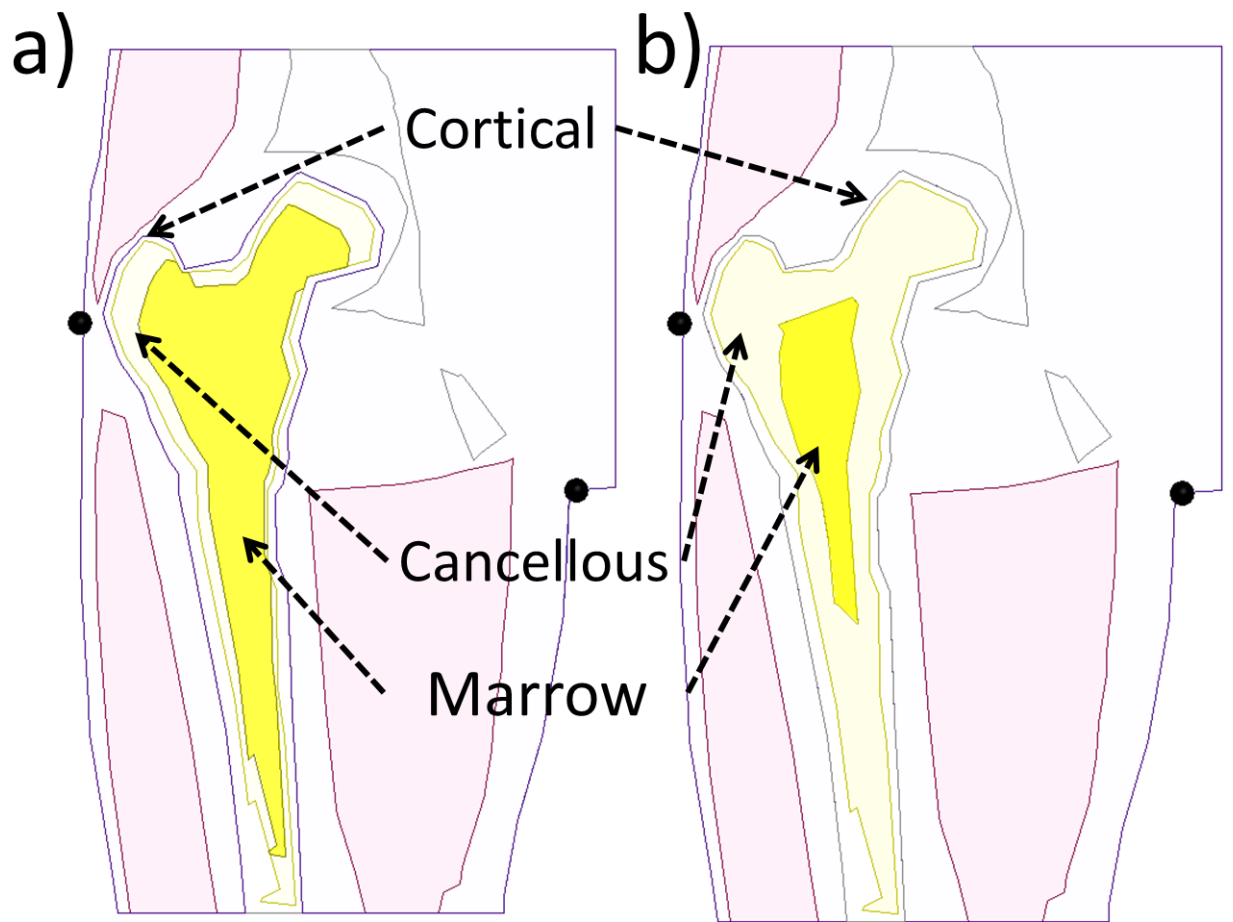


Fig. 33. Comparison of an a) osteoporotic femur and b) a normal femur

The magnitude of the Poynting vector was then measured at the RX point shown in Fig. 33 for 400MHz and 800MHz excitations. These vector plots can be seen in Fig. 34. The differences between the osteoporotic (a) and the normal (b) femurs are subtle from the field perspective. A closer inspection shows that the osteoporotic case, due to the large volume of bone marrow, causes more diffraction as the Poynting vector propagates through it. The result is power being dispersed across the entire inner portion of the leg (where the receiver array would be located).

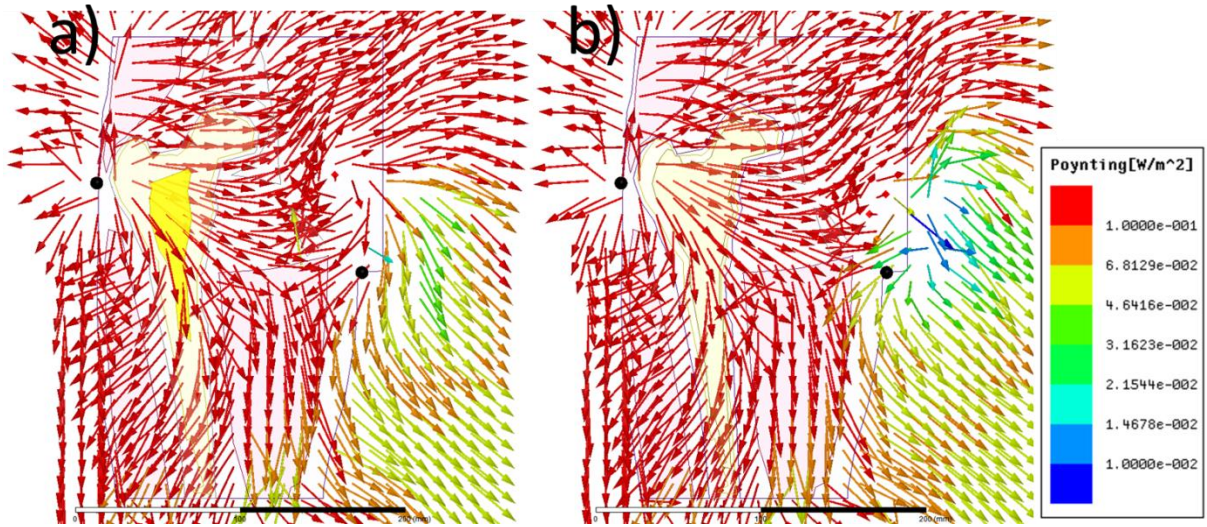


Fig. 34. Signal path through the leg for an 800 MHz excitation. a) the osteoporotic case and b) the normal femur

In comparison, a large difference in the received magnitude can be observed between the two cases. The changes in the received signal strength (RSS) are summarized in Table 20. Even without an optimal channel, one can clearly see an observable change in the total received power at both 400MHz and 800MHz. Unfortunately, this assumes that all other tissues remain the same between the osteoporotic and normal cases, which is highly unlikely.

Table 20. Change in RSS between two femur models for selected CW frequencies

400MHz	RSS (mW)	% Change
Normal	136.27	13.69%
Osteoporotic	117.62	
800MHz		
Normal	155.50	43.60%
Osteoporotic	87.71	

Frequency Selection

In the previous section, we used 400MHz and 800MHz as two seemingly arbitrary frequencies to demonstrate the change in RSS between the osteoporotic and normal human femur models. Most organic tissues are dispersive, and thus have different material properties at different frequencies [55]. Ideally, we would like to select a frequency (or range of frequencies) where the different between the osteoporotic

case would be most noticeable. The primary difference between the osteoporotic femur and the normal femur is that the former replaces most of the cancellous bone with yellow bone marrow. We are then interesting in scanning at a frequency where the difference between the material properties of the cancellous bone and the bone marrow are largest.

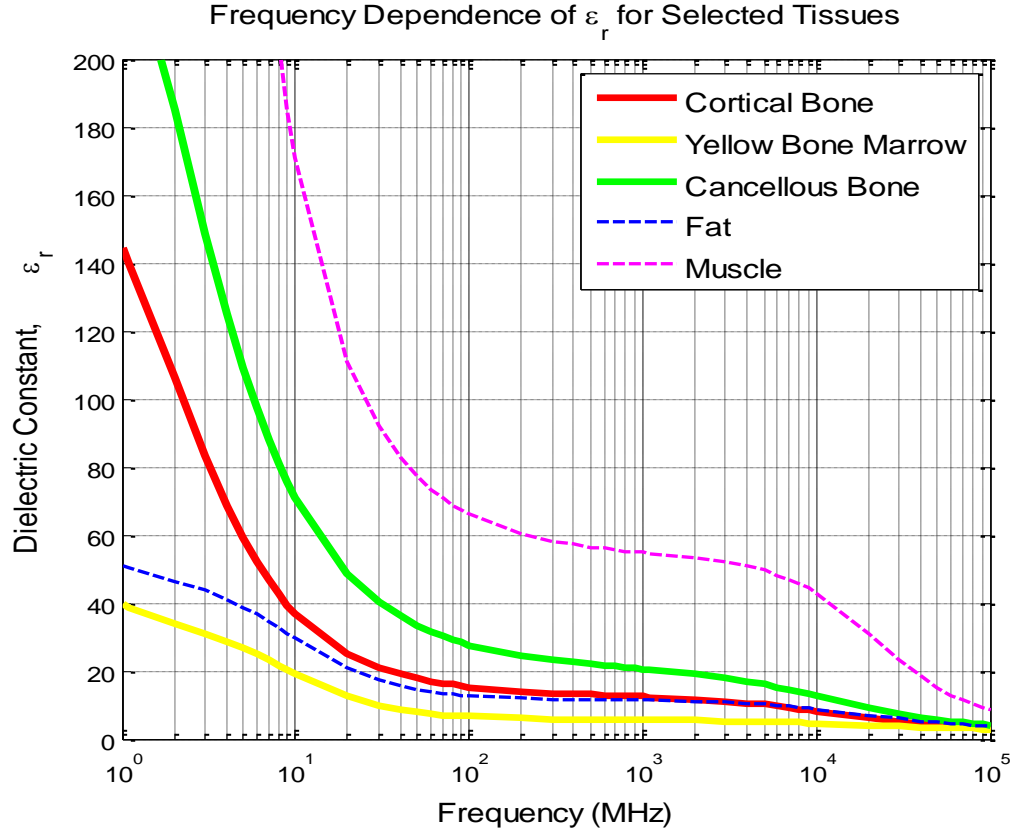


Fig. 35. Frequency dependence of the dielectric constant on selected tissues

One can see in Fig. 35 that the dielectric constant of most tissues decreases with frequency. Again, we are interested in maximizing the difference between the dielectric constant of the cancellous bone (the green curve) and the yellow bone marrow (the yellow curve). At low frequencies (i.e. <1MHz) there is a large difference because the ϵ_r of the cancellous bone marrow becomes very large. This is not very useful because the wavelength is extremely long at 1MHz (~300m in air, or ~21m in the cancellous bone), making it difficult to generate a directive beam. Conversely, the dielectric constant shrinks for all organs above 10GHz, which would make discerning between the materials difficult.

Instead, let us plot the percentage difference between the cancellous bone and the yellow bone marrow, as shown in Fig. 36. A very large difference of greater than 70% occurs in the 10MHz to 1 GHz region. Although the wavelength is still too long at 10MHz ($\sim 30\text{m}$ in air at $\sim 3.8\text{m}$ in cancellous bone), we can scan between 100MHz and 1GHz, which is the main frequency range for this study. Moreover, the cortical bone has approximately the same dielectric constant as the surrounding fat in this region, which effectively eliminates this additional interface.

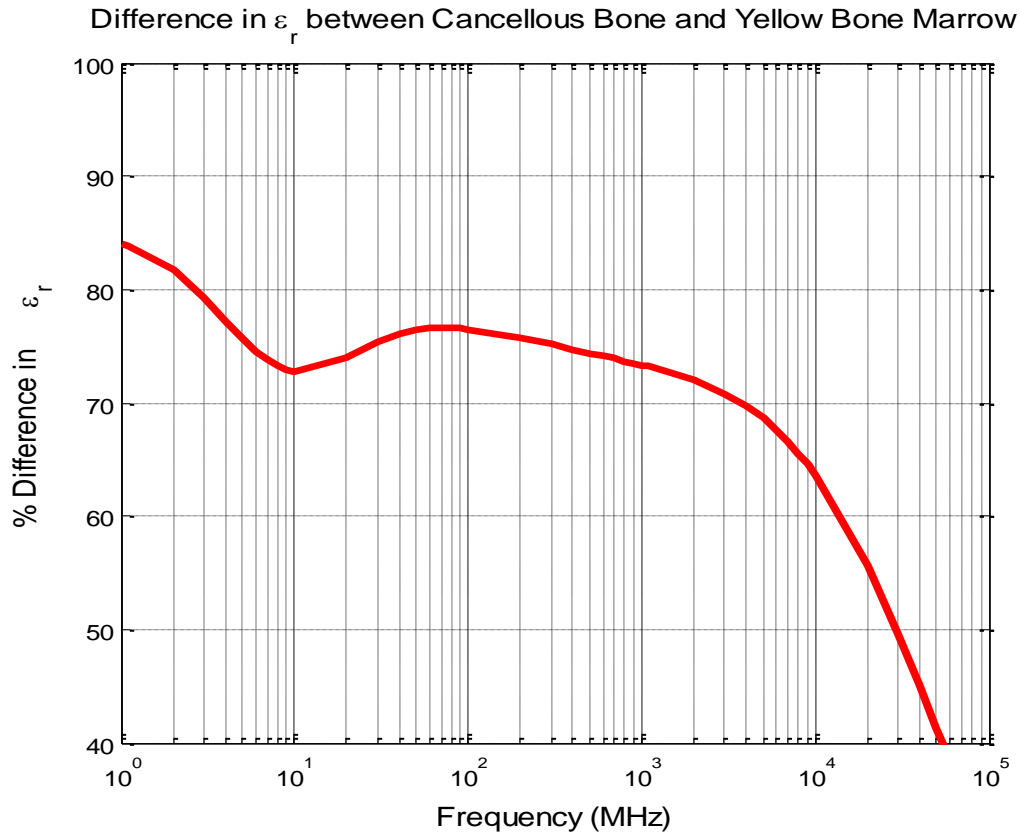


Fig. 36. Percentage difference in Dielectric Constant between the Cancellous Bone and Yellow Bone Marrow

We can also examine the conductivity, σ . Although the conductivity does not affect the wavelength, a high conductivity will result in high losses, reducing the received SNR.

Fig. 37 shows the frequency dependence of the conductivity of the same tissues. One may immediately note that the conductivity of all tissues increases with frequency, and sharply rises past 1GHz. Frequencies beyond this value will suffer significant attenuation in the media, making the recovery signal processing very challenging and prone to measurement error. Secondly, one may also note that the

muscle is much more conductive than the surrounding organs. Avoiding muscle in the signal path is advantageous to the high losses it can occur. The conductivity values between the yellow bone marrow and the cancellous bone are much more stable than the dielectric constant, as seen in Fig. 38.

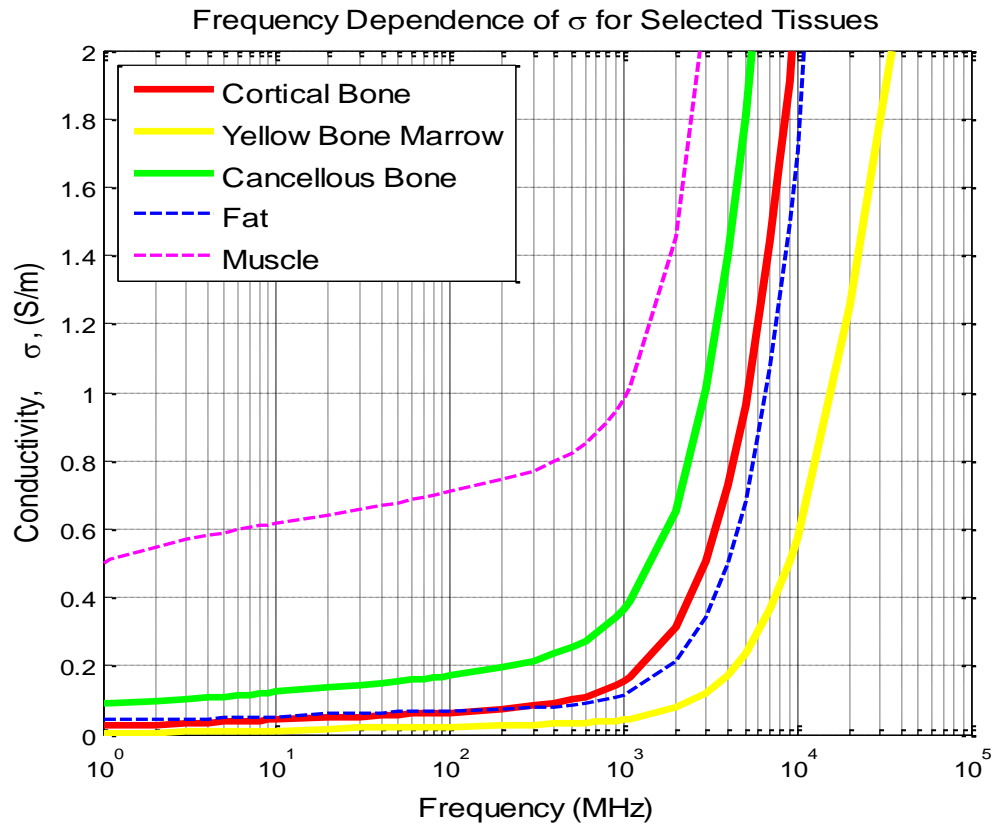


Fig. 37 Frequency dependence of the conductivity of selected tissues

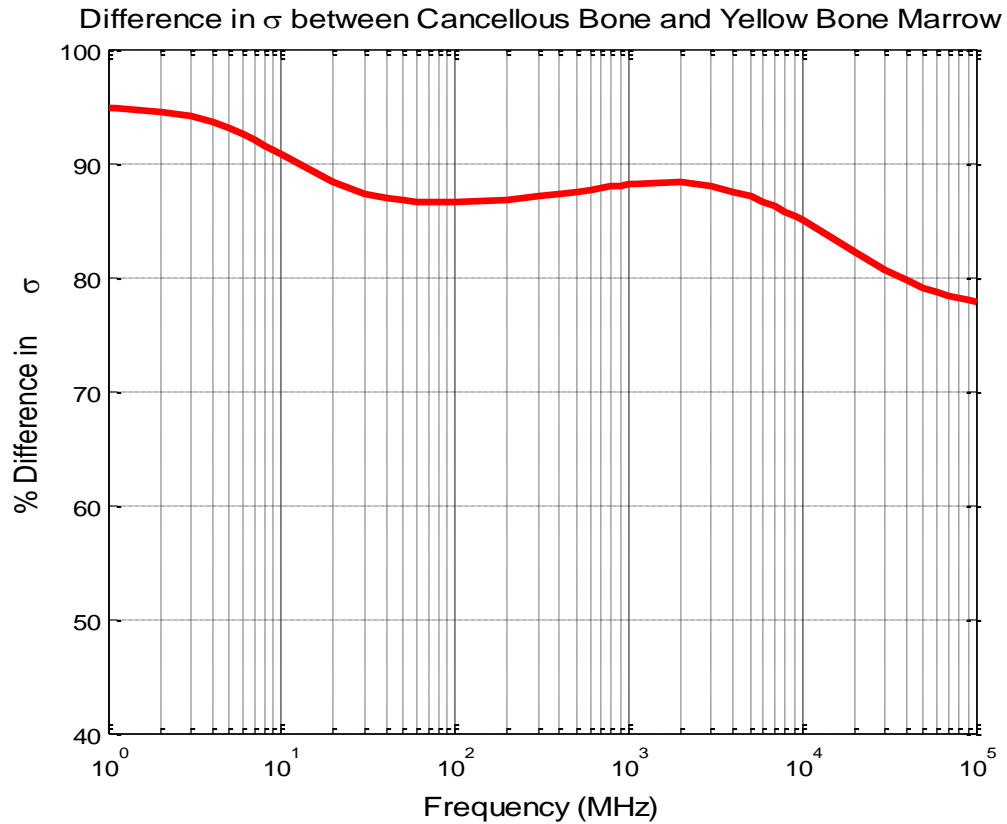


Fig. 38. Percentage difference in Conductivity between the Cancellous Bone and Yellow Bone Marrow

RX Array

Unlike consumer goods, biological components are not mass produced with exacting standards in terms of size and composition. Varying dimensions and material properties between humans could lead to large variations in the measured RSS. To counter this, we propose that we use an array to measure changes in RSS, as opposed to the magnitude. An example of such an array was created in our Ansys model to measure an infinite number of points, as seen in Fig. 39. As previously shown, the muscle tissue generally caused very large angles of refraction due to the high dielectric contrast with the surrounding fat tissue. The TX positions are selected near the muscle gap between the Gluteus and quadriceps, and are located 10 mm apart from one another.

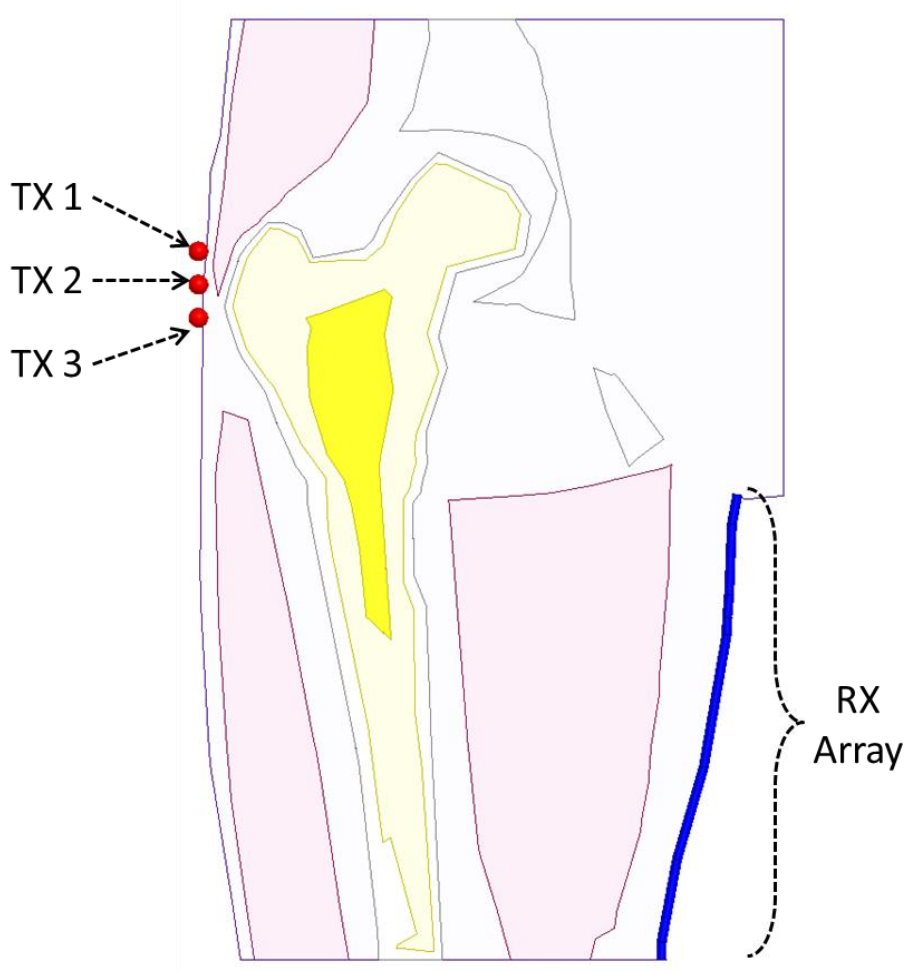


Fig. 39. Transmitter and receiver array positions on the leg

Nominal Case

To evaluate the robustness of our model, a sensitivity analysis was performed with the different tissue layers. The first case to be observed was the nominal case, where we compare the normal and osteoporotic femurs, assuming their normal material properties (i.e. those provided by IT'IS), as shown in Table 21. Again, one should note the high permittivity and conductivity of the muscle tissue in comparison to all surrounding tissues. This is significant, as it will cause a high angle of diffraction.

Table 21. Relevant Material Properties for the Nominal Femur

Tissue/Organ	$\epsilon_r(400MHz)$	$\sigma(400MHz)$
Fat Tissue	11.6	0.081

Muscle Tissue	57.1	0.796
Cortical Bone	13.1	0.091
Cancellous Bone	22.4	0.235
Yellow Marrow	5.67	0.030

Fig. 40 shows the normalized RSS across the receiver for both the normal and osteoporotic femurs, assuming all materials have their nominal properties. The 0mm distance across the receiver array corresponds to the point closest to the groin (as this point is closest to the TX, it logically has the highest signal strength), and greater distances are further down the leg. For all antenna positions, one may notice that the presence of additional bone marrow (from the osteoporotic femur) causes greater dispersion of the power, and a wider received area, regardless of the TX position. The middle TX position (#2) appears to show the greatest difference, with a peak of a 72.86% change at approximately 700MHz.

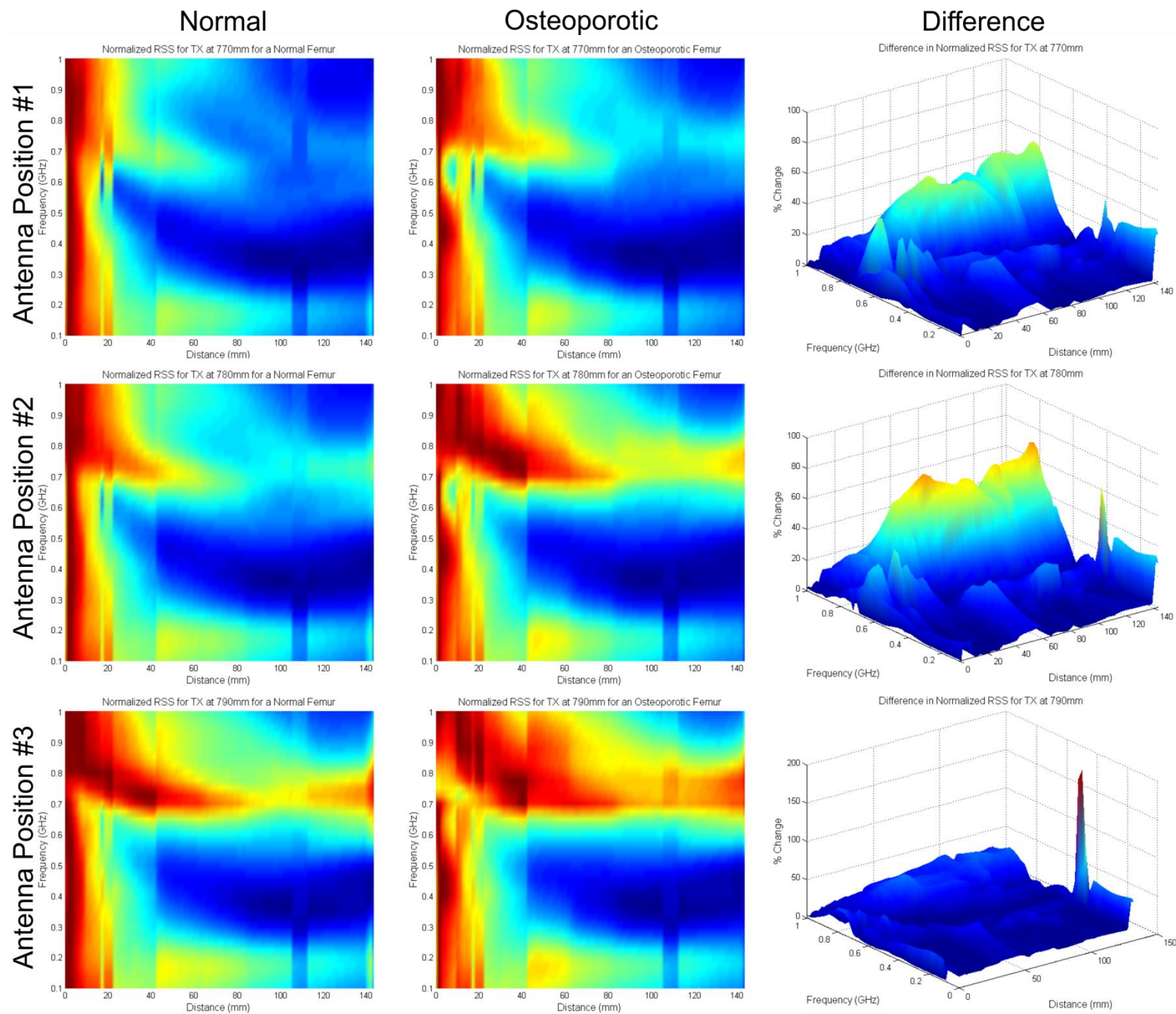


Fig. 40 Simulated, Normalized RSS along the Femur for the Nominal Case

Increased Fat Dielectric Constant Case

The majority of this femur from the Ansys body model consists primarily of fat. To be a useful medical diagnosis tool, this method would need to have little variation between the quantity and material properties of the fat layer (which could vary from patient to patient). Generating a new FEM mesh is very difficult, thus we instead elected to increase the dielectric constant of the fat layer by 10%. Note that all material properties are still frequency dependent, thus the ϵ_r of fat was increased across the entire frequency sweep, not a specific point. A sample of these frequencies is displayed in Table 22.

Table 22. Relevant Material Properties for the Femur with an Increased Fat Dielectric Constant

Tissue/Organ	$\epsilon_r(400MHz)$	$\sigma(400MHz)$
Fat Tissue	12.76	0.081
Muscle Tissue	57.1	0.796
Cortical Bone	13.1	0.091
Cancellous Bone	22.4	0.235
Yellow Marrow	5.67	0.030

Fig. 41 shows the normalized RSS across the receiver for both the normal and osteoporotic femurs, with fat having a higher dielectric constant. All else was kept the same as the previous study in the interests of a fair comparison. Visually, there is very little difference between the nominal case and the one with a different dielectric constant for fat. The curves are slightly less defined, as there is less of a sharp difference between the fat tissue and surrounding muscle (the angle of diffraction will not be as large). The maximum difference (ignoring the outlier due to numerical error for the third case) is now 73.87%, which is still a substantial difference (only a single percentage point change from the nominal case).

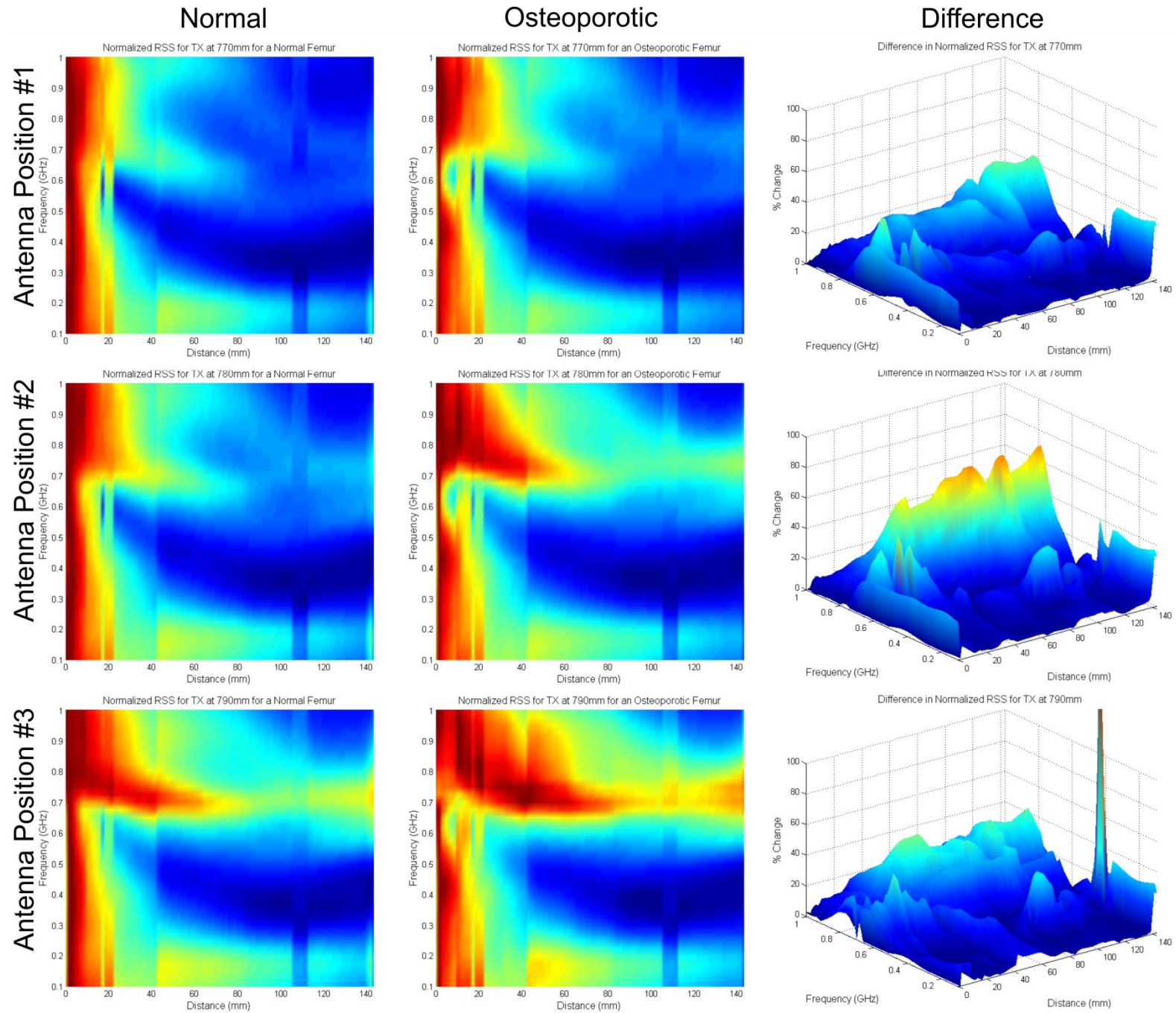


Fig. 41 Simulated, Normalized RSS along the Femur with an Increased Fat Dielectric Constant

Highly Conductive Muscle Case

Considering the high volume of muscle surrounding the femur, it is logical to examine the variation of its material properties on the received signal. The conductivity of the muscle tissue is raised to match its dielectric constant. Table 23 summarizes these new values in comparison to the other material properties at 400MHz.

Table 23. Relevant Material Properties for the Femur with Highly Conductive Muscles

Tissue/Organ	$\epsilon_r(400MHz)$	$\sigma(400MHz)$
Fat Tissue	11.6	0.081
Muscle Tissue	57.1	57.1
Cortical Bone	13.1	0.091
Cancellous Bone	22.4	0.235
Yellow Marrow	5.67	0.030

Fig. 42 shows the normalized RSS across the receiver for both the normal and osteoporotic femurs, with all material properties being nominal with the exception of the highly conductive muscle. The results are substantially different from the previous two cases. Instead of destroying the channel, the muscle helps act as a waveguide, focusing it to the other side of the leg, provided the transmitter is in the correct location. The first and third TX locations cause the beam to strike the conductive muscle tissue almost at a 90° angle, resulting in very little of the beam arriving at the RX array (thus there is a very small difference between the normal and osteoporotic cases). However, if one places the TX antenna at position 2, the beam has a clear path through the bone marrow, and there is a very clear change (91.6%) at 700MHz.

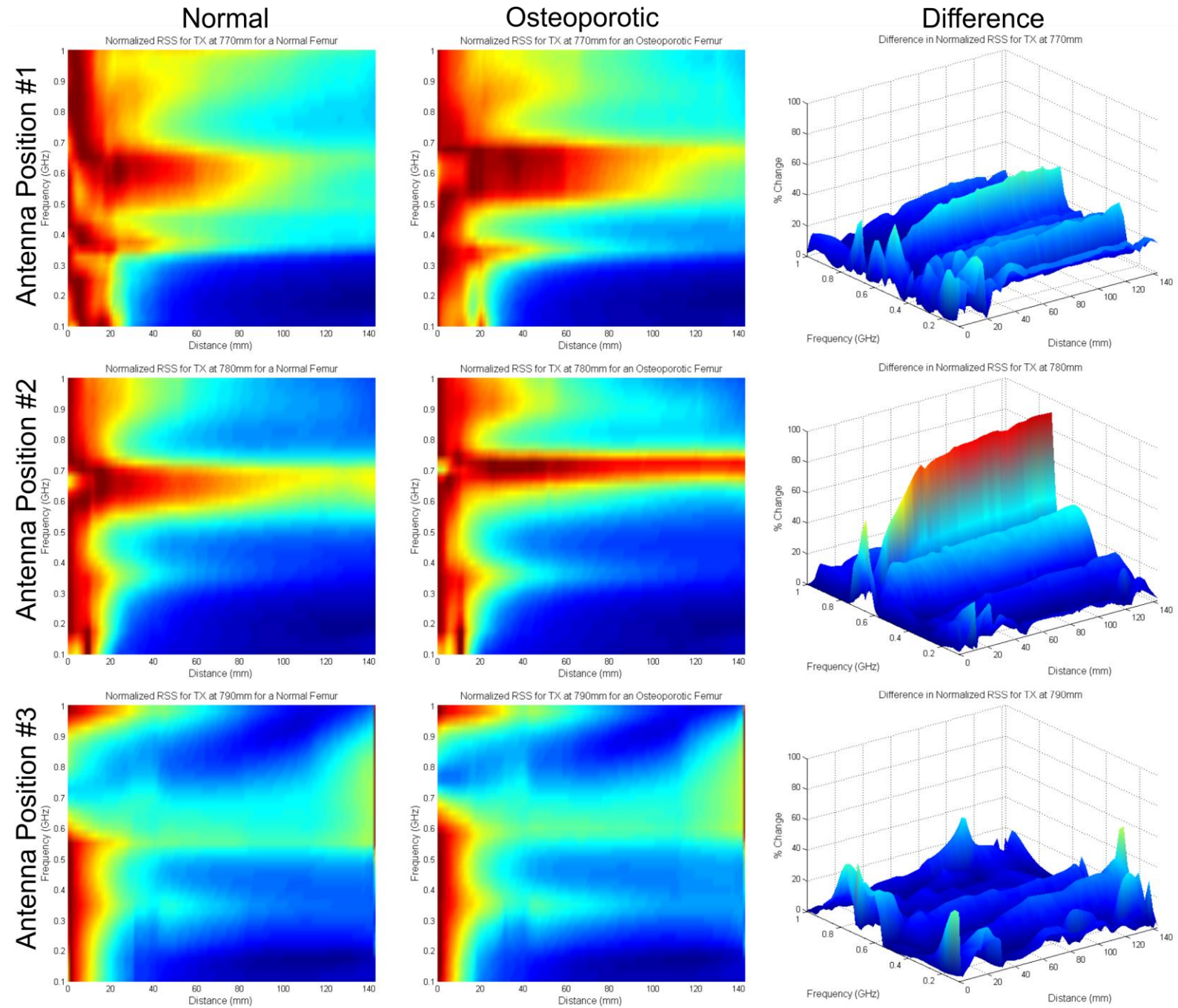


Fig. 42 Simulated, Normalized RSS along the Femur with highly conductive muscle tissue

CONCLUSION

The goal of this project was to design an electrically small antenna that could generate a directive beam into a dielectric. We have shown that two orthogonal loops driven in quadrature will produce a highly-directive beam with a maximum directivity of upwards of 10dB. This is significantly greater than a traditional loop in free space, which only produces a maximum directivity of 1.76dB. [1]. Although significantly higher directivities are possible from superdirective antennas, and traveling wave antennas, these are often comparable to a wavelength in size. Superdirective arrays generally require very high currents for a small gain in directivity. Yagi-Uda travelling wave antennas can reach directivities greater than 14dB (generally between 14.8 and 17.8), but require multiple reflectors and directors, each approximately $\frac{\lambda}{2}$ in length and $\frac{\lambda}{4}$ spacing between directors [1]. Both are much less practical than the proposed orthogonal loop design, provided one wishes to radiate into the dielectric

A.) HUMAN BODY RESULTS

No human testing was performed in this work, and all analysis is based purely on simulation data. Fortunately, modern FEM meshes have become increasingly accurate, and can closely follow the complex curvature of human organs. This, in combination with the frequency dependent material properties of each tissue layer (provided by [55]), helps validate our studies.

Our simulations have demonstrated the existence of a channel through the brain to the sinus cavity. By exciting orthogonal coil antennas in quadrature, a directed beam can be generated and steered through a dielectric medium (e.g. the brain, skull, etc.). By adjusting the transmitter position and excitation frequency, an optimal path through the brain was found.

The meshes used in this study were improved from those in [11] from both an anatomical and material perspective. Previous versions did not include separate layers for the fat, muscle, and other organs. However, the previous model still illustrates a similar path through the brain to the tongue at a similar transmission position. This implies that the existence of the path may be robust to material changes. One may need to tune the exact frequency and position, but there should be at least one

acceptable transmission path. The variance in the conditions for generating these paths for different head models would be a worthwhile avenue of research for conducting practical microwave tomography.

Similar results were observed in a separate study of the human leg. To determine if a patient is developing osteoporosis, we proposed that an orthogonal coil antenna is placed next the femur and several receivers are positional along the inside the leg. The osteoporotic femur is clearly distinguishable from the healthy femur because osteoporosis causes the cancellous bone to be replaced by bone marrow. As these have very different material properties, the change in the angle of diffraction shifts the transmission path and results in a relative power peak at a given location and frequency. Even after varying the conductivity of the muscle and the dielectric constant of the fat, one could identify which femur was osteoporotic due to the aforementioned peaks.

B.) FUTURE EXTENSIONS AND APPLICATIONS

At the time of writing, models of the orthogonal antenna are being constructed at WPI for testing, as shown in Fig. 43. Each of the antennas is constructed from 24 gauge coax on a square 25.4mm \times 25.4mm FR4 substrate (1.6mm thick). To achieve a 90° phase offset, one of the loops is fed through a coax cable that is $\frac{\lambda}{4}$ (at 400MHz \rightarrow 18.74cm) after the output of the power splitter. After shielding the cables with an RF choke (stopping the wires from radiating), a testing apparatus must be constructed to verify the directive properties of the coils. This will likely consist of a water tank with an adjustable TX antenna on the outer surface and an RX antenna internally (to avoid reflections caused by the outside of the tank). This is an extension of the theory and will tested at a later date.

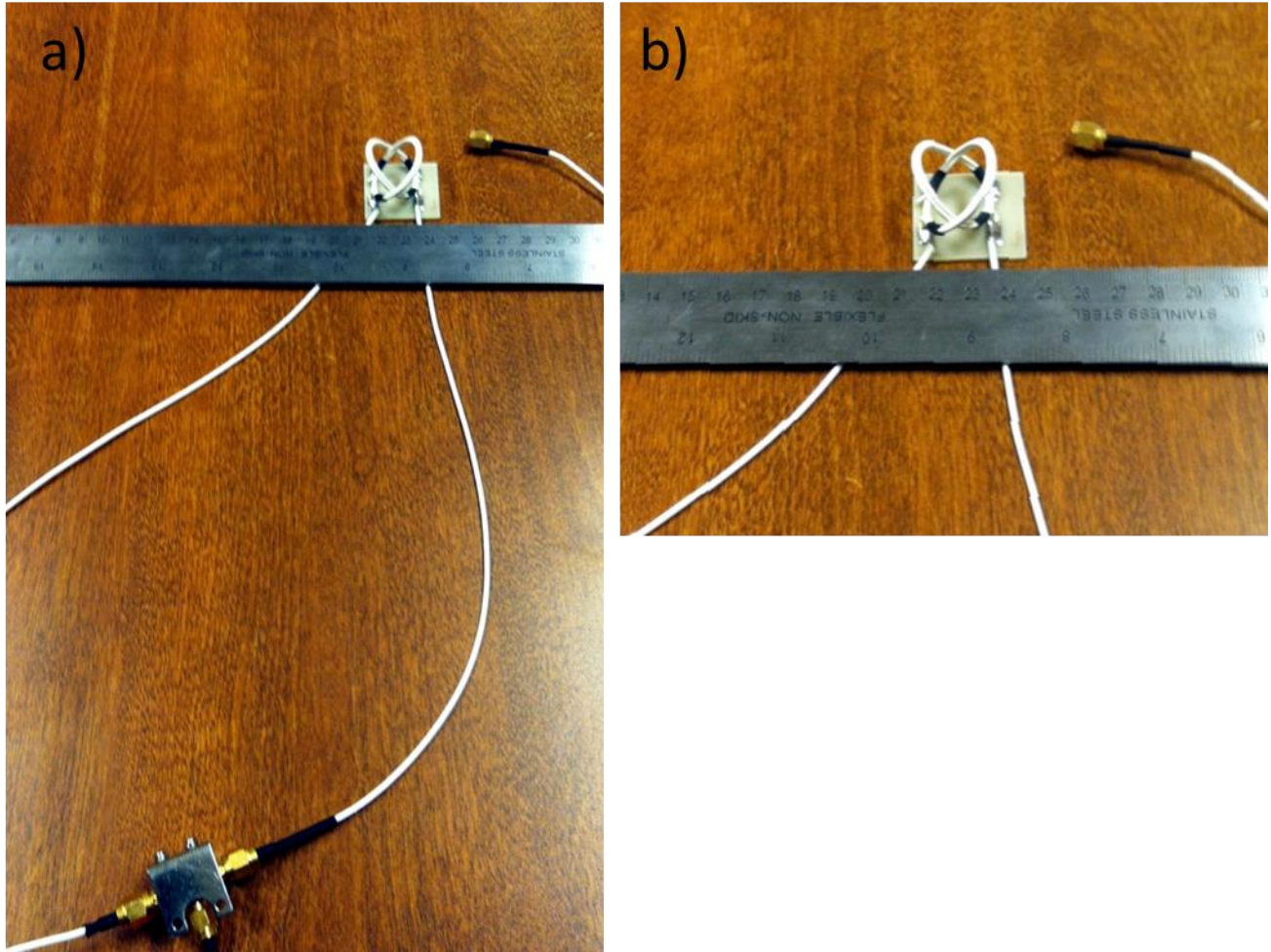


Fig. 43. Prototype orthogonal coil antennas. a) Power splitter connected to two cables offset by $\lambda/4$ b) Close-up view of the antenna

The orthogonal coil antenna is not limited to biomedical applications. Indeed, our recent work focuses on establishing channels through the head and leg to detect material abnormalities, but the same method can be extended to any arbitrary dielectric. For example, one may wish to apply this technique to ground penetrating radar [70], [71] or submarine detection [72], [73]. The small size and directivity of this antenna lends itself well to constructing large arrays to obtain greater resolution for imaging techniques.

REFERENCES

- [1] C. Balanis, *Antenna Theory*, 3rd edition, Hoboken, NJ: Wiley-Interscience, 2005.
- [2] M. Cheney, D. Isaacson and J. Newell, "Electrical Impedance Tomography," *SIAM Review, Society for Industrial and Applied Mathematics*, vol. 41, no. 1, pp. 85-101, 1999.
- [3] L. Ma, H. Wei and M. Soleimani, "Pipelines Inspection Using Magnetic Induction Tomography Based on a Narrowband Pass Filtering Method," *Progress in Electromagnetics Research*, vol. 23, no. 1, pp. 65-78, 2012.
- [4] S. Semenov, "Microwave tomography: review of the progress towards clinical applications," *Philosophical Transactions the Royal Society of Mathematical, Physical & Engineering Sciences*, vol. 367, no. 1, pp. 3021-3042, 2009.
- [5] U. Serguei, Y. Semenov and D. R. Corefield, "Microwave tomography for brain imaging: Feasibility assessment for stroke detection," *International Journal of Antennas and Propagation*, 2008.
- [6] J. L. Volakis, C.-C. Chen and K. Fujimoto, *Small Antennas Miniaturization Techniques & Applications*, McGraw Hill, 2010.
- [7] G. S. Smith, "Directive Properties of Antennas for Transmission into a Material Half-Space," *IEEE Transactions on Antennas and Propagation*, vol. 32, no. 33, pp. 232-245, 1984.
- [8] G. S. Smith and L. N. An, "Loop antennas for directive transmission into a material half space," *Radio Science*, vol. 18, no. 5, pp. 664-674, 1983.
- [9] P. S. Hall, Y. Hao and S. L. Cotton, "Progress in antenna and propagation for body area networks," *International Symposium on Signals Systems and Electronics (ISSSE)*, vol. 1, pp. 1,7, 2010.
- [10] A. Gupta and T. D. Abhayapala, "Body Area Networks: Radio channel modelling and propagation characteristics," *Communications Theory Workshop*, pp. 58,63, 2008.
- [11] G. Noetscher, A. Htet, J. Elloian, S. Makarov, F. Sciré-Scappuzzo and A. Pascual-Leone, "Detecting in Vivo Changes of Electrical Properties of Cerebral Spinal Fluid Using Microwave Signals from Small Coil Antennas-Numerical Simulation," *IEEE Signal Processing in Medicine and Biology Symposium (SPMB)*, pp. 1-6, 2012.
- [12] N. Rais, P. J. Soh, F. Malek, S. Ahmad, N. Hashim and P. S. Hall, "A review of wearable antennas," in *Antennas & Propagation Conference, 2009*, Loughborough, 2009.
- [13] J. Matthew, B. Pirollo, A. Tyler and G. Pettitt, "Body wearable antennas for UHF/VHF," in *Antennas and Propagation Conference*, Loughborough, 2008.
- [14] D. A. Hill and J. R. Wait, "Analytical Investigations of Electromagnetic Location Schemes Relevant to Mine Rescue," U.S. Bureau of Mines, Pittsburgh, 1974.
- [15] X. Xu and Y. F. Huang, "An efficient Analysis of Vertical Dipole Antennas Above a Lossy Half-Space," *Progress in Electromagnetics Research*, vol. 75, no. 1, pp. 3553-377, 2007.
- [16] S. J. Radzevicius, J. J. Daniels, E. D. Guy and M. A. Vendl, "Significance of Crossed-Dipole Antennas for High Noise Environments," in *Proceedings of the Symposium on the Application of Geophysics to Environmental and Engineering Problems*, 2000.
- [17] S. L. Dvorak and E. F. Kuester, "Numerical Computation of 2D Sommerfeld Integrals- Decomposition of the Angular Integral," *Journal of Computational Physics*, vol. 98, no. 1, pp. 199-216, 1992.
- [18] I. V. Lindell and E. Alanen, "Exact Image Theory for the Sommerfeld Half-space Problem, Part I: Vertical Magnetic Dipole," *IEEE Transactions on Antennas and Propagation*, vol. 32, no. 2, pp. 126-133, 1984.

- [19] I. V. Lindell and E. Alanen, "Exact Image Theory for the Sommerfeld Half-space Problem, Part II: Vertical Electric Dipole," *IEEE Transactions on Antennas and Propagation*, vol. 32, no. 8, pp. 841-847, 1984.
- [20] I. V. Lindell and E. Alanen, "Exact Image Theory for the Sommerfeld Half-Space Problem, Part III: General Formulation," *IEEE Transactions on Antennas and Propagation*, vol. 21, no. 10, pp. 1027-1032, 1984.
- [21] W. Lukosz and R. E. Kunz, "Light Emission by Magnetic and Electric Dipoles Close to a Plane Interface," *Optical Society of America*, vol. 67, no. 12, pp. 1607-1615, 1978.
- [22] W. Lukosz and R. E. Kunz, "Light Emission by MAGnetic and Electric Dipoles close to a Plane Dielectric Interface. II Radiation Patterns of Perpendicular Oriented Dipoles," *Optical Society of America*, vol. 67, no. 12, pp. 1615-1619, 1978.
- [23] M. Mark, T. Bjorninen, L. Ukkonen, L. Sydanheimo and J. Rabaey, "SAR reduction and link optimization for mm-size remotely powered wireless implants using segmented loop antennas," in *IEEE Topical Conference on Biomedical Wireless Technologies, Networks and Sensing Systems (BioWireless)*, 2011.
- [24] S. Lee and Y. Yoon, "Fatt arm spiral antenna for wideband capsule endoscope systems," in *IEEE Radio and Wireless Symposium (RWS)*, 2010.
- [25] K. Karathanasis and I. Karanasiou, "Combining reflector focused and phased array beamforming for microwave diagnosis and therapy," in *IEEE 12th International Conference on Bioinformatics & Bioengineering (BIBE)*, 2012.
- [26] D. Margetis, "Radiation of Horizontal Electric Dipole on Large Dielectric Sphere," *Journal of Mathematical Physics*, vol. 43, no. 6, pp. 3162-3201, 2002.
- [27] D. Margetis and T. T. Wu, "Exactly Calculable Field Components of Electric Dipoles in Planar Boundary," *Journal of Mathematical Physics*, vol. 42, no. 2, pp. 713-745, 2001.
- [28] P. R. Bannister, "Summary of Image Theory Expressions for Quasi-Static Fields of Antennas at or above the Earth's Surface," *Proceedings of the IEEE*, vol. 67, no. 7, pp. 1001-1008, 1979.
- [29] P. R. Bannister and R. L. Dube, "Simple Expressions for Horizontal Electric Dipole Quasi-Static Range Subsurface-to-Subsurface and Subsurface-to-Air Propagation," *Radio Science*, vol. 13, no. 3, pp. 501-507, 1978.
- [30] K. Li, Y. Lu and W. Pan, "Exact Formulas for the Lateral Electromagnetic Pulses Generated by a Horizontal Electric Dipole in the Interface of Two Dielectrics," *Progress in Electromagnetics Research*, vol. 55, no. 1, pp. 249-284, 2005.
- [31] K. Li, *Electromagnetic Fields in Stratified Media*, Springer Berlin Heidelberg, 2009.
- [32] R. K. Moore and W. E. Blair, "Dipole Radiation in a Conducting Half Space," *Journal of Research of the National Bureau of Standards*, vol. 64, no. 6, pp. 547-563, 1961.
- [33] N. Engheta, C. H. Papas and C. Elachi, "Radiation Patterns of Interfacial Dipole Antennas," *Radio Science*, vol. 17, no. 6, pp. 1557-1566, 1982.
- [34] K. I. Nikoskinen, "Time-Domain Study of Half-Space Transmission Problem with Vertical and Horizontal Dipoles," *IEEE Transactions on Antennas and Propagation*, vol. 41, no. 10, pp. 1399-1407, 1993.
- [35] M. Parise, "Second-Order Formulation for the Quasi-Static Field from a Horizontal Electric Dipole on a Lossy Half Space," *Progress in Electromagnetics Research*, vol. 140, no. 1, pp. 439-455, 2013.
- [36] M. Parise, "Second-Order Formulation for the Quasi-Static Field from a Vertical Electric Dipole on a Lossy Half-Space," *Progress in Electromagnetics Research*, vol. 136, no. 1, pp. 509-521, 2013.
- [37] M. Parise, "Exact Electromagnetic Field Excited by a Vertical Magnetic Dipole on the Surface of a Lossy Half-Space," *Progress in Electromagnetics Research*, vol. 23, no. 1, pp. 69-82, 2010.

- [38] R. W. King, "The Electromagnetic Field of a Horizontal Eleetric Dipole in the Presence of a Three-Layered Region: Supplement," *Journal of Applied Physics*, vol. 74, no. 8, pp. 4845-4848, 1993.
- [39] S. Makarov and G. Noetscher, "Directional in-quadrature orthogonal coil antenna and an array thereof for localization within a human body in a Fresnel region," in *Antennas and Propagation Society Interational Symposium IEEE (APSURSI)*, 2012.
- [40] J. Kim and Y. Rahmat-Samii, "Implanted antennas inside a human body: simulations, designs, and characterizations," *IEEE Trans. Microwave Theory Techniques*, vol. 52, no. 8, pp. 1934-1943, Aug. 2004.
- [41] C. Gabriel and S. Gabriel, "Compilation of the dielectric properties of body tissues at RF and microwave frequencies. Armstrong Lab.," 1996. [Online]. Available: <http://www.brooks.af.mil/AFRL/HED/hedr/reports/dielectric/home.html>.
- [42] F. Ulaby, E. Michielssen and U. Ravaioli, *Fundamentals of Applied Electromagnetics*, 6th Edition, Upper Saddle River, NJ: Pearson Education, 2010.
- [43] A. Lea, P. Hui, J. Ollikainen and R. Vaughan, "Propagation Between On-Body Antennas," *IEEE Transactions on Antennas and Propagation*, vol. 57, no. 11, pp. 3619-3627, Nov. 2009.
- [44] A. Sommerfeld, "Electromagnetic waves near wires," *Wied Annalen*, vol. 67, pp. 223-290, 1899.
- [45] J. Zenneck, "Ueber die fortplanzung ebener electromagnetischen wellen laengs einer ebenen Leiterflaeche und ihre Bezeihung zur drahlosen Telegraphie," *Nannalen der Physik*, vol. 23, pp. 846-866, 1907.
- [46] J. Wait, "The ancient and modern history of EM ground-wave propagation," *IEEE Antennas and Propgation Magazine*, vol. 40, no. 5, pp. 7-24, Oct. 1998.
- [47] A. Lea, P. Hui, J. Ollikainen and R. Vaughan, "Theory of propagation for direct on-body wireless sensor communications," *Antennas and Propagation for Body-Centric Wireless Communications*, pp. 1-5, April 2009.
- [48] R. King and M. Brown, "Lateral electromagnetic waves along plane boundaries: A summarizing approach," *Processings of the IEEE*, vol. 72, no. 5, pp. 595,611, May 1984.
- [49] K. Norton, "The Propagation of radio waves over a plane earth," *Nature*, p. 135, 1935.
- [50] U.S. National Library of Medicine, "The Visible Human Project," [Online]. Available: http://www.nlm.nih.gov/research/visible/visible_human.html.
- [51] P. A. Yushkevich, J. Piven, H. C. Hazlett, R. G. Smith, S. Ho, J. C. Gee and G. Gerig, "User-guided 3D active contour segmentation of anatomical structures: significantly improved efficiency and reliability," *Neuroimage*, vol. 31, no. 3, pp. 1116-1128, Jul. 1 2006.
- [52] J. Vollmer, R. Mencl and H. Müller, "Improved Laplacian smoothing of noisy suface meshes," *Computer graphics forum*, vol. 18, no. 3, pp. 131-138, Sep. 1999.
- [53] MSC Software Corporation, "MD NASTRAN Input," 2010. [Online]. Available: http://www.aero.polimi.it/~lanz/bacheca/downloads/cost/aa10_11/MD_Nastran_Input.pdf.
- [54] "La syntaxe particulière de Nastran," [Online]. Available: https://moodle.polymtl.ca/pluginfile.php/120548/mod_page/content/3/Travaux_pratiques/TP1/suppl_lab0_sem0.pdf.
- [55] IT'IS Foundation, "Tissue Properties," IT'IS Foundation, 2012. [Online]. Available: <http://www.itis.ethz.ch/itis-for-health/tissue-properties/database/dielectric-properties/>. [Accessed 15 October 2013].
- [56] IT'IS Foundation, "Tissue Properties," IT'IS Foundation, 2012. [Online]. Available: <http://www.itis.ethz.ch/itis-for-health/tissue-properties/database/dielectric-properties/>. [Accessed 15 October 2013].

- [57] C. Gabriel, S. Gabriel and C. Corthout, "The Dielectric Properties of Biological Tissues: I. Literature Survey," *Physics in Medicine and Biology*, vol. 41, no. 11, pp. 2231-2249, 1996.
- [58] S. Gabriel, R. W. Lau and C. Gabriel, "The dielectric properties of biological tissues: II Measurements in frequency range of 10Hz to 20GHz.," *Physics in Medicine and Biology*, vol. 41, no. 11, pp. 2251-2269, 1996.
- [59] S. Gabriel, R. W. Lau and C. Gabriel, "The dielectric properties of biological tissues: III Parameteric models for the dielectric spectrum of tissues," *Physics in Medicine and Biology*, vol. 41, no. 11, pp. 2271-2293, 1996.
- [60] J. Tunaley, "A Summary of EM Theory for Dipole Fields near a Conducting Half-Space," London Research and Development Corporation, Ottawa, 2012.
- [61] A. Sommerfeld, *Partial Differential Equations in Physics*, Volume VI, London: Academic Press, 1964.
- [62] A. Banos, *Dipole Radiation in the Presence of a Conducting Half-Space*, Oxford: Pergamon Press, 1966.
- [63] J. R. Wait, *Electromagnetic Radiation from Cylindrical Structures*, New York: 1959, 1959.
- [64] C. Someda, *Electromagnetic Waves*, Second Edition, Boca Raton, FL: Taylor & Francis Group, 2006.
- [65] L. Novotny and B. Hecht, *Principles of Nano-Optics*, Cambridge: Cambridge University Press, 2006.
- [66] I. S. Gradshteyn and I. M. Ryzhik, *Table of Integrals, Series, and Products*, Burlington, MA: Elsevier Inc., 2007.
- [67] C. Balanis, *Antenna Theory*, Hoboken, NJ: Wiley-Interscience, 2005.
- [68] A. Lopoppan, V. Thomas, G. Bindu, C. Rajasekaran and K. T. Mathew, "Analysis of human cerebro spinal fluid at ISM band of frequencies," *Journal of Electromagnetic Waves and Applications*, vol. 20, no. 6, pp. 773-779, Apr. 2012.
- [69] G. D. Meyer, F. Shapiro, H. Vanderstichele, E. Vanmechelen, S. Engelborghs, P. Deyn, E. Coart, O. Hansson, L. Minthon, H. Zetterberg, K. Blennow, L. Shaw and J. Trojanowski, "Diagnosis independent Alzheimer Disease biomarker signature in cognitively normal elderly people," *Arch Neurol*, vol. 67, no. 8, pp. 949-956, Aug. 2010.
- [70] R. W. King, B. H. Sandler and L. C. Schen, "A Comprehensive Study of Subsurface Propagation from Horizontal Electric Dipoles," *IEEE Transactions on Geoscience and Remote Sensing*, vol. 18, no. 3, pp. 225-233, 1980.
- [71] S. J. Radzevicius, C.-c. Chen, L. Peters and J. J. Daniels, "Near-Field dipole radiation dynamics through FDTD," *Journal of Applied Geophysics*, vol. 52, no. 1, pp. 75-91, 2003.
- [72] L. Brock-Nannestad, "EM Phenomena in the ELF Range: EM Fields of Submerged Dipoles and Finite Antennas," Saclant ASW Research Center, La Spezia, Italy, 1965.
- [73] P. Bannister, "New Formulas for HED, HMD, VED, and VMD Subsurface-to-Subsurface Propagation," Naval Underwater Systems Center, Newport, 1984.
- [74] D. Ireland and M. Bialkowski, "Microwave Head Imaging for Stroke Detection," *Progress in Electromagnetics Research*, vol. 21, pp. 163-175, 2011.
- [75] FEKO, "Bio-Electromagnetics," 2013. [Online]. Available: <http://www.feko.info/applications/Bio-Electromagnetics>. [Accessed 27 March 2013].
- [76] CST, "HUGO Human Body Model," Computer Simulation Technology, 2013. [Online]. Available: <http://www.cst.com/Content/Applications/Article/HUGO+Human+Body+Model>. [Accessed 27 March 2013].
- [77] "High Resolution Phantom Models," Speag, 2012. [Online]. Available:

<http://www.speag.com/products/semcad/applications/medical-technology-simulations/high-resolution-phantom-models/>. [Accessed 2013 27 March].

- [78] C. Penney, "Computation of Fields and SAR for MRI with Finite-Difference, Time-Domain Software," 23 January 2008. [Online]. Available:
http://www.remcom.com/storage/downloads/publications/computation%20of%20fields%20and%20sar%20for%20mri_mw%20journal%20dec%202007_final.pdf. [Accessed 27 March 2013].
- [79] Ansys, "Ansoft Human Body Model Documentation," Ansys, Canonsburg, PA, USA, 2012.

ACKNOWLEDGEMENTS

This work would not have been possible without meshing assistance provided by Aung T. Htet of Worcester Polytechnic Institute. Cumulatively, Prof. Makarov, and his two PhD students, Gregory Noetscher and Janakinadh Yanamadala, spent over 1000 hours generating the human body mesh that was used in this and other projects. It is time-consuming and meticulous work that requires great skill and patience to accurately trace each organ.

Dr. Alvaro Pascual-Leone of the Beth Israel Deaconess Medical Center at Harvard Medical School provided technical expertise regarding the maladies and associated symptoms with the human brain. I lack a biology background, thus he could confirm the validity of material properties of the brain changing when there is an imbalance of proteins.

I am greatly appreciative of my fellow graduate student, Nicholas DeMarinis, for his help is formatting my paper and his additional support. Although this may sound trivial, he spent nearly 20 hours over the course of the past year helping me format the pictures, tables, and text to look professional.

I would also like to thank Dr. S. Louie of Ansys for her advice regarding the simulation software and methods. Dr. Rao of the MITRE Corporation also provided invaluable advice and feedback. As my advisor for my undergraduate senior project, Dr. Rao taught me much about antennas and propagation. Professor Ludwig was always available whenever I needed feedback on a theoretical problem, or when I was uncertain about an electromagnetic principle. Of course, my advisor, Professor Makarov, constantly pushed me forward, even when I struggled. At some times, this was frustrating and tiring; however, this level of quality would never have been achieved without him. Needless to say, he helped me through all of the mathematical derivations and was always available when I had a question.

APPENDIX A. ORTHOGONAL MAGNETIC DIPOLES IN FREE SPACE

The loop is a very simple option for selecting an antenna that can propagate through the body. A small loop or coil is very similar to a small dipole; however, it is horizontally polarized as opposed to vertically polarized [67]. This implies that a dipole would be radiating in E_θ , whereas a loop is radiating in H_θ . First, let us consider the basic case of this orthogonal coils or magnetic dipoles in free-space.

A.) VERTICAL AND HORIZONTAL MAGNETIC DIPOLES IN FREE SPACE

In the absence of any media interfaces, it is more straightforward to exploit symmetry in field solutions. The derivation of the fields is a classical textbook problem and is only briefly outlined here. For a more in-depth discussion of the derivation, please refer to a text such as [67].

Let us assume we have a horizontal ring of current on the x-y plane, such that it acts as a vertical magnetic dipole. The source is located at the spherical coordinates (r', θ', ϕ') in reference to the observation point (r, θ, ϕ) . Given this coordinate system and corresponding spherical unit vectors $\hat{\mathbf{a}}_r, \hat{\mathbf{a}}_\theta$, and $\hat{\mathbf{a}}_\phi$, it is possible to define the current vector as [67]:

$$\begin{aligned} \vec{\mathbf{I}}_e = & \hat{\mathbf{a}}_r [I_\phi \sin(\theta) \sin(\phi - \phi')] + \\ & \hat{\mathbf{a}}_\theta [I_\phi \cos(\theta) \sin(\phi - \phi')] + \\ & \hat{\mathbf{a}}_\phi [I_\phi \sin(\theta) \sin(\phi - \phi')] \end{aligned} \quad (1)$$

One should note that in this special case, current is only flowing around the ring, and thus only in the ϕ direction. The distance formula dictates that distance between the observation point and the source point of this infinitesimal magnetic dipole can be given by:

$$R = \sqrt{r^2 + a^2 - 2arsin(\theta)\cos(\phi - \phi')}, \quad (2)$$

where a is the radius of the loop. Fortunately, the integral for the vector potential can be simplified because the spatial current distribution is not dependent on ϕ , allowing one to simply set it to zero. The resulting vector potential with respect to an excitation current I_0 , magnetic permeability μ (of the surrounding transmission medium, which is assumed to have $\mu_r = 1$), and wavenumber k , is then given by:

$$A_\phi = \frac{a\mu I_0}{4\pi} \int_0^{2\pi} \frac{\cos(\phi') e^{-jkD}}{D} d\phi' \quad (3)$$

When integrated, this evaluates to the vector potential:

$$\vec{A} = \frac{k\mu a^2 I_0 \sin(\theta)}{4\pi} \left[1 + \frac{1}{jkr}\right] e^\wedge - jkr \quad (4)$$

Of course, this vector potential can be expanded into the individual magnetic and electric field components. Let us also substitute this radius and current in the loop for the equivalent magnetic dipole moment and length, I_m and ℓ respectively to produce the fields given in Table 24 [67].

Table 24. Electric and magnetic field components for a vertical magnetic dipole in free-space

	\vec{E}	\vec{H}
r	0	$\frac{I_m \ell \cos(\theta)}{2\pi\eta r^2} \left[1 + \frac{1}{jkr}\right] e^{-jkr}$
θ	0	$j \frac{k I_m \ell \sin(\theta)}{4\pi\eta r} \left[1 + \frac{1}{jkr} - \frac{1}{(kr)^2}\right] e^{-jkr}$
ϕ	$-j \left(\frac{k I_m \ell \sin(\theta)}{4\pi r}\right) \left[1 + \frac{1}{jkr}\right] e^{-jkr}$	0

With the full field solution for the vertical magnetic dipole presented, let us now consider the horizontal dipole. As previously stated, one may exploit symmetry of the fields due to the lack of any media interfaces that would otherwise cause absorption or diffraction. In general, a spherical coordinate system may be rotated by a rotation matrix.

$$\vec{E} = \begin{bmatrix} \sin(\theta) \cos(\phi) & \cos(\phi) \cos(\theta) & -\sin(\phi) \\ \sin(\theta) \sin(\phi) & \sin(\phi) \cos(\theta) & \cos(\phi) \\ \cos(\theta) & -\sin(\theta) & 0 \end{bmatrix} \begin{bmatrix} E_r \\ E_\theta \\ E_\phi \end{bmatrix} \quad (5)$$

To produce the fields of a horizontal magnetic dipole, the original solution must be rotated about the θ axis by 90° (not the azimuthal axis, ϕ , which is symmetric about the vertical dipole).

$$\vec{E} = \begin{bmatrix} 1 & 0 & 0 \\ 0 & 0 & 1 \\ 0 & -1 & 0 \end{bmatrix} \begin{bmatrix} E_r \\ E_\theta \\ E_\phi \end{bmatrix} = \begin{bmatrix} E_r \\ E_\phi \\ -E_\theta \end{bmatrix} \quad (6)$$

A similar process is followed for the magnetic field components. Substituting back the original values for the fields from Table 24, we can find the electric and magnetic field solution for a horizontally oriented dipole in free-space.

Table 25- Electric and magnetic field components for a horizontal magnetic dipole in free-space

	\vec{E}	\vec{H}
r	0	$\frac{I_m \ell \cos(\theta)}{2\pi\eta r^2} \left[1 + \frac{1}{jkr}\right] e^{-jkr}$
θ	$-j \left(\frac{k I_m \ell \sin(\theta)}{4\pi r} \right) \left[1 + \frac{1}{jkr}\right] e^{-jkr}$	0
ϕ	0	$-j \frac{k I_m \ell \sin(\theta)}{4\pi\eta r} \left[1 + \frac{1}{jkr} - \frac{1}{(kr)^2}\right] e^{-jkr}$

B.) ORTHOGONAL MAGNETIC DIPOLES IN FREE-SPACE

The previous section outlined the field solutions for both the horizontal and vertical magnetic dipoles in free-space. The proposed orthogonal coil antenna effectively utilizes both of these antennas. To generate the field solution for this orthogonal dipole, one must apply a 90° phase shift in the time domain to either of the excitations. One may then apply superposition to add the two time-harmonic fields together.

A 90° phase shift can be applied to the electric and magnetic field solution by simply multiplying each term by $e^{\frac{j\pi}{2}}$. The fields for the delayed horizontal dipole are then given by Table 26.

Table 26- Electric and magnetic field components for a horizontal magnetic dipole that is delayed by 90 degrees

	\vec{E}	\vec{H}
r	0	$\frac{I_m \ell \cos(\theta)}{2\pi\eta r^2} \left[1 + \frac{1}{jkr}\right] e^{-j(kr + \frac{\pi}{2})}$
θ	$-j \left(\frac{kI_m \ell \sin(\theta)}{4\pi r} \right) \left[1 + \frac{1}{jkr}\right] e^{-j(kr + \frac{\pi}{2})}$	0
ϕ	0	$-j \frac{kI_m \ell \sin(\theta)}{4\pi\eta r} \left[1 + \frac{1}{jkr} - \frac{1}{(kr)^2}\right] e^{-j(kr + \frac{\pi}{2})}$

By the principle of superposition, the field resulting from two orthogonal magnetic dipoles is the sum of each vector component from each respective antenna.

Table 27- Electric and magnetic field components for two orthogonal magnetic dipoles in free-space

	\vec{E}	\vec{H}
r	0	$\frac{I_m \ell \cos(\theta)}{2\pi\eta r^2} \left[1 + \frac{1}{jkr}\right] [e^{-j(kr + \frac{\pi}{2})} + e^{-jkr}]$
θ	$-j \left(\frac{kI_m \ell \sin(\theta)}{4\pi r} \right) \left[1 + \frac{1}{jkr}\right] e^{-j(kr + \frac{\pi}{2})}$	$j \frac{kI_m \ell \sin(\theta)}{4\pi\eta r} \left[1 + \frac{1}{jkr} - \frac{1}{(kr)^2}\right] e^{-jkr}$
ϕ	$-j \left(\frac{kI_m \ell \sin(\theta)}{4\pi r} \right) \left[1 + \frac{1}{jkr}\right] e^{-jkr}$	$-j \frac{kI_m \ell \sin(\theta)}{4\pi\eta r} \left[1 + \frac{1}{jkr} - \frac{1}{(kr)^2}\right] e^{-j(kr + \frac{\pi}{2})}$

APPENDIX B. MESH AND MODEL SENSITIVITY

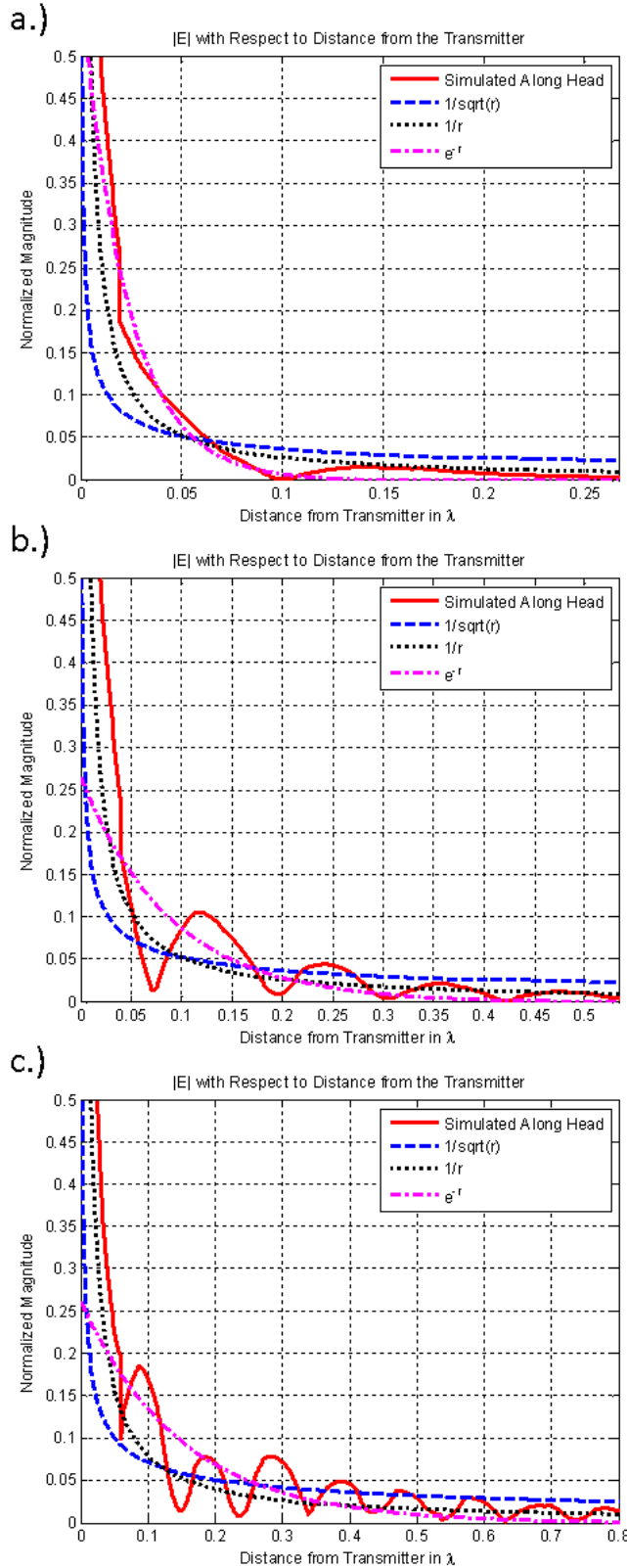


Fig. 44. Normalized magnitude of the simulated electric field along the surface of the head at a.) 800 MHz, b.) 1600 MHz, and c.) 2400 MHz.

The model simulated in [11] demonstrated faint, yet distinct surface waves along the head. No surface waves were observed on the new mesh. In order to better classify the fields on this earlier model, the magnitude of the electric field was simulated following a segmented line along the surface of the head. While the head is not large enough to show the trends in the far field, it is possible to find a curve of best fit using the least mean square algorithm for several different rates. Note that the field strengths have been normalized to their respective maximum amplitudes such that $|E| = 1$ at a distance of 0λ (an infinitesimal distance from the surface of the antenna).

As shown in Fig. 44(a), it is difficult to see the surface wave propagating at 800 MHz; but it appears emerging near 0.1λ . The

field intensity appears to decay at

a rate proportional to e^{-r}

indicative of a Norton wave

propagating along the scalp [49].

In the previous section, it was

clear that surface waves began to

develop near 1600 MHz. Fig.

Table 28. Root mean square error of each fit of the E field

f(MHz)	RMSE			
	1/R	1/sqrt(R)	exp(-R)	
400	0.0777	0.0784	0.0271	
800	0.0178	0.0292	0.0079	
1400	0.0190	0.0287	0.0165	
1600	0.0187	0.0271	0.0190	
1800	0.0194	0.0262	0.0191	
2400	0.0245	0.0170	0.0150	

10(b) shows a distinct oscillating pattern that appears to be decaying at a slower rate than the expected $\frac{1}{r}$.

Indeed, it more closely follows $\frac{1}{\sqrt{r}}$, and exhibits the behavior best represented by a Zenneck wave [45].

Unfortunately, it is difficult to examine the fields at a larger distance (extending the simulation to the far field) because of the limited size of the human head and the curved nature of the boundary. Of course, these oscillations are noticeably shorter than a wavelength because they are coupled to the surface of the skin, which has a much higher dielectric constant to that of air.

As one could infer from the images, the oscillations become much more profound at higher frequencies. Fig. 44(c) shows a clear oscillating decay expected from a surface wave. However, the irregular curvature of the head complicates the classification of this wave. It is possible that any of the previously presented waves could be described by the Norton wave with a rate of decay proportional to e^{-r} [49], but these classifications are only valid for planar surfaces in the far field. Table 28 presents the root mean square error (RMSE) of each type of fit for the corresponding frequencies.

When the brain undergoes any form of serious trauma, through either injury or the development of a tumor, the physical and electric properties change accordingly. Recent studies indicate that different levels of blood content, potentially caused by burst blood vessels in the head, will lead to different dielectric properties [5], [74]. The channel established earlier in this text can be used to detect such abnormalities.

Table 29. Phase difference in the electric field in a given direction on the tongue with respect to changes in the dielectric constant of the brain.

$\Delta\epsilon_r$ (%)	$\Delta\theta_x(^{\circ})$	$\Delta\theta_y(^{\circ})$	$\Delta\theta_z(^{\circ})$
-10.00	-52.27	-65.53	-22.95
-7.50	-40.09	-50.36	-18.32
-5.00	-25.91	-34.45	-12.77
-2.50	-14.32	-17.59	-6.54
2.50	15.52	18.21	6.84
5.00	32.88	36.54	14.03
7.50	52.25	54.88	21.15
10.00	73.95	72.64	28.60

A continuous wave is ideal for detecting volumetric changes of the brain. It is narrowband, straightforward to produce and measure, and provides a clear phase reference. Conversely, a broadband pulse would provide additional frequency diversity, allowing one to determine the existence of small objects, such as localized lacuna tumors in the brain. This is

possible because the additional frequencies allow one to resolve more paths, thus obtaining additional information from the multipath characteristics of the channel. Broadband pulse simulation is beyond the scope of this study. An excellent example of such an analysis is provided in [5], but requires complex signal processing and 72 antennas to image the entire head. On the contrary, the CW technique shown here allows for simple and rapid detection of any general abnormality in the brain by observing the integral characteristics of the wave. This, perhaps, could be used as a screening measure to determine if more in-depth analysis is needed.

Although there was significant multipath at higher frequencies, two primary propagation channels were observed at 1600MHz with the transmitter coils located 10° from the vertical axis. One propagation path, caused by the surface wave, exists along the dielectric interface created by the skin. As seen in Fig. 23, this path does not penetrate more than 1.5 cm into the head, limiting the amount of information that can be obtained about the brain. The second channel is the volumetric wave that propagates through the brain, CSF, and skull to the mouth. This opening provides a convenient location to extract the signal.

The same simulation model was used to study the effects of changes in the dielectric constant. For comparison, the electric field was observed on the forehead and the tongue, as seen in Fig. 45. These two locations provide access to the volumetric and surface waves with minimal interference from multipath.

The phase velocity in a dielectric medium is proportional to the relative dielectric constant of medium of propagation. This implies that a continuous wave should undergo different phase shifts corresponding

to the change in the dielectric properties of the brain. Although the magnitude should also change, small differences in magnitude are difficult to accurately measure in a lossy material. Furthermore, the amount of decay is dependent on the length of the given path. In comparison the forehead is closer to the transmitter than the tongue, thus it will always have a higher received magnitude. Only the relative phase delays are considered for the purpose of this comparison.

The phase shifts for the electric field in the X, Y, and Z directions is shown in Table 29. All three components are shown because the polarization of the receiver antenna would determine which would be accepted. One should note that in the X and Y directions, the phase shift was greater than 14° even for a slight change in the dielectric constant of 2.5%. In comparison, the phase difference on the forehead,

caused by the surface waves, was almost completely unaffected by the changes in the brain. In general, the overall phase shift on the forehead was typically not more than 1%, with a few outliers exceeding 5%

that may be attributed to numerical error.

APPENDIX C. MATLAB CODE FOR THE ORTHOGONAL COIL RADIATION PATTERN GRAPHICAL USER INTERFACE

The following MATLAB code produces the radiation pattern for vertical, horizontal, and orthogonal magnetic dipoles based on the prompted user inputs:

```
function []=radgui()
close all
global thetares;
global phires;
global w;
global m;
global phaseoff;
global epsilon1;
global epsilon2;
global sigma1;
global sigma2;
global plotflag;
global lowlim;
global uplim;

%GUI Version
%Fields for horizontal and magnetic dipoles:
%General Case: Arbitrary Material Properties and Height

%% Defaults
plotflag=0; %generate plots? (1=yes)

% constants
thetares=pi/128; %resolution of theta sweep in radians
phires=pi/64; %resolution of phi sweep in radians

mu0=1.25663706e-6; %permeability of free space (m*kg/(s^2*A^2))
eps0=8.85418782e-12; %permittivity of free space ((s^4*A^2)/(m^3*kg))

w=2*pi*400e6; %angular frequency (rads/s)

m=1;%magnetic dipole moment (=I0*pi*a^2)
r=1; %radial distance (this will cancel out, but is here for completeness)

h=0; %height (in meters) from the surface of the interface
phaseoff=exp(j*pi/2); %phase offset between horizontal and vertical dipoles

%display
lowlim=-10; %lowest limit (in dB) for plotting purposes
uplim=10; %highest limit (in dB) for plotting purposes

%material properties
epsilon1=eps0*1;
epsilon2=eps0*10;
sigma1=0;
sigma2=0;
```

```

%output text (display max directivity, where it occurs and power ratio)
outtext.maxD1='Maximum D (dB)';
outtext.maxangle1='Location of max(D)';
outtext.powerratio1='Power radiated in Mat. 1 vs Mat. 2';

scrsz = get(0,'ScreenSize');
mainmenu=figure('OuterPosition',[1 scrsz(4)/2 scrsz(3) (scrsz(4)/2)])
%horizontal
figure('OuterPosition',[1 50 scrsz(3)/3 (scrsz(4)/2)-50])
horaxis=gca;
%title('Horiztonal Magnetic Dipole')
%vertical
figure('OuterPosition',[scrsz(3)/3 50 scrsz(3)/3 (scrsz(4)/2)-50])
veraxis=gca;
%title('Vertical Magnetic Dipole')
%combined
figure('OuterPosition',[2*scrsz(3)/3 50 scrsz(3)/3 (scrsz(4)/2)-50])
comaxis=gca;
%title('Orthogonal Dipoles')

%Generate the "Command Menu"
%% General options
genpanel=uipanel(mainmenu,'Title','General
Options','Position',[0.01,0.01,0.32,0.9])
uicontrol(genpanel,'Style','text','Units','Normalized','Position',[0,0.9,0.15
,0.1],'String','Theta Resolution (degrees)')
uicontrol(genpanel,'Style','edit','Units','Normalized','Position',[0.15,0.9,0
.15,0.1],'String',thetares*180/pi,'Callback',@setthetaCB)
uicontrol(genpanel,'Style','text','Units','Normalized','Position',[0,0.8,0.15
,0.1],'String','Phi Resolution (degrees)')
uicontrol(genpanel,'Style','edit','Units','Normalized','Position',[0.15,0.8,0
.15,0.1],'String',phires*180/pi,'Callback',@setphiCB)
uicontrol(genpanel,'Style','text','Units','Normalized','Position',[0,0.7,0.15
,0.1],'String','Generate Plots?')
uicontrol(genpanel,'Style','checkbox','Units','Normalized','Position',[0.15,0
.7,0.15,0.1],'Callback',@checkboxCB)
uicontrol(genpanel,'Style','text','Units','Normalized','Position',[0,0.6,0.15
,0.1],'String','Minimum Scale (dB):')
uicontrol(genpanel,'Style','edit','Units','Normalized','Position',[0.15,0.6,0
.15,0.1],'String',-10,'Callback',@setlowCB)
uicontrol(genpanel,'Style','text','Units','Normalized','Position',[0.5,0.6,0.
15,0.1],'String','Maximum Scale (dB):')
uicontrol(genpanel,'Style','edit','Units','Normalized','Position',[0.65,0.6,0
.15,0.1],'String',10,'Callback',@sethighCB)
uicontrol(genpanel,'Style','pushbutton','Units','Normalized','Position',[0,0.
3,1,0.2],'String','Update','Callback',@genpattern)

%display results for the Horiztonal Magnetic Dipole
handles.texthor1=uicontrol(genpanel,'Style','text','Units','Normalized','Posi
tion',[0,0.2,1,0.1],'String',outtext.maxD1)

```

```

handles.texthor2=uicontrol(genpanel,'Style','text','Units','Normalized','Position',[0,0.1,1,0.1],'String',outtext.maxangle1)
handles.texthor3=uicontrol(genpanel,'Style','text','Units','Normalized','Position',[0,0.1,1,0.1],'String',outtext.powerratio1)

%callback functions
function checkboxCB(hObj,event)
    %global plotflag;
    plotflag=get(hObj,'Value');
end

function setthetaCB(hObj,event)
    %global thetares;
    thetares=str2num(get(hObj,'String'))*(pi/180);
end

function setphiCB(hObj,event)
    %global phires;
    phires=str2num(get(hObj,'String'))*(pi/180);
end

function setlowCB(hObj,event)
    %global phires;
    lowlim=str2num(get(hObj,'String'));
end

function sethighCB(hObj,event)
    %global phires;
    uplim=str2num(get(hObj,'String'));
end

%% Excitation options
excitepanel=uipanel(mainmenu,'Title','Excitation Options','Position',[0.33,0.01,0.32,0.9])
uicontrol(excitepanel,'Style','text','Units','Normalized','Position',[0,0.9,0.15,0.1],'String','Frequency (MHz)')
uicontrol(excitepanel,'Style','edit','Units','Normalized','Position',[0.15,0.9,0.15,0.1],'String',(w/(2*pi))/1e6,'Callback',@setfreqCB)
uicontrol(excitepanel,'Style','text','Units','Normalized','Position',[0,0.8,0.15,0.1],'String','Magnetic Moment (A/m^2)')
uicontrol(excitepanel,'Style','edit','Units','Normalized','Position',[0.15,0.8,0.15,0.1],'String',m,'Callback',@setmCB)
uicontrol(excitepanel,'Style','text','Units','Normalized','Position',[0,0.7,0.15,0.1],'String','Phase Offset (degrees)')
uicontrol(excitepanel,'Style','edit','Units','Normalized','Position',[0.15,0.7,0.15,0.1],'String',90,'Callback',@setphaseoffCB)

%display results for the Vertical Magnetic Dipole
handles.textver1=uicontrol(excitepanel,'Style','text','Units','Normalized','Position',[0,0.2,1,0.1],'String',outtext.maxD1)
handles.textver2=uicontrol(excitepanel,'Style','text','Units','Normalized','Position',[0,0.1,1,0.1],'String',outtext.maxangle1)
handles.textver3=uicontrol(excitepanel,'Style','text','Units','Normalized','Position',[0,0.1,1,0.1],'String',outtext.powerratio1)

```

```

%callback functions

function setfreqCB(hObj,event)
    %global w;
    w=str2num(get(hObj,'String'))/1e6)*2*pi;
end

function setmCB(hObj,event)
    %global m;
    m=str2num(get(hObj,'String'));
end

function setphaseoffCB(hObj,event)
    %global phaseoff;
    phaseoff=exp(j*str2num(get(hObj,'String'))*(pi/180));
end

%% Material Properties
matpanel=uipanel(mainmenu,'Title','Material
Properties','Position',[0.65,0.01,0.32,0.9])
uicontrol(matpanel,'Style','text','Units','Normalized','Position',[0.25,0.9,0
.25,0.1],'String','epsilon')
uicontrol(matpanel,'Style','text','Units','Normalized','Position',[0.5,0.9,0.
25,0.1],'String','sigma')
uicontrol(matpanel,'Style','text','Units','Normalized','Position',[0,0.8,0.25
,0.1],'String','Material 1')
uicontrol(matpanel,'Style','text','Units','Normalized','Position',[0,0.7,0.25
,0.1],'String','Material 2')
uicontrol(matpanel,'Style','text','Units','Normalized','Position',[0,0.6,1,0.
1],'String','Height above the interface (m):')
uicontrol(matpanel,'Style','edit','Units','Normalized','Position',[0.25,0.5,0
.5,0.1],'String',h,'Callback',@heightCB)

uicontrol(matpanel,'Style','edit','Units','Normalized','Position',[0.25,0.8,0
.25,0.1],'String',epsilon1/eps0,'Callback',@eps1CB)
uicontrol(matpanel,'Style','edit','Units','Normalized','Position',[0.5,0.8,0.
25,0.1],'String',sigma1,'Callback',@sig1CB)
uicontrol(matpanel,'Style','edit','Units','Normalized','Position',[0.25,0.7,0
.25,0.1],'String',epsilon2/eps0,'Callback',@eps2CB)
uicontrol(matpanel,'Style','edit','Units','Normalized','Position',[0.5,0.7,0.
25,0.1],'String',sigma2,'Callback',@sig2CB)

%display results for the Orthogonal Dipoles
handles.textcom1=uicontrol(matpanel,'Style','text','Units','Normalized','Posi
tion',[0,0.2,1,0.1],'String',outtext.maxD1)
handles.textcom2=uicontrol(matpanel,'Style','text','Units','Normalized','Posi
tion',[0,0.1,1,0.1],'String',outtext.maxangle1)
handles.textcom3=uicontrol(matpanel,'Style','text','Units','Normalized','Posi
tion',[0,0,1,0.1],'String',outtext.powerratio1)

%callback functions
function eps1CB(hObj,event)

```

```

    %global epsilon1;
    %global eps0;
    epsilon1=eps0*(str2num(get(hObj,'String')));
end

function eps2CB(hObj,event)
    %global epsilon2;
    %global eps0;
    epsilon2=eps0*(str2num(get(hObj,'String')));
end

function sig1CB(hObj,event)
    %global sigma1;
    sigma1=(str2num(get(hObj,'String')));
end

function sig2CB(hObj,event)
    %global sigma2;
    sigma2=(str2num(get(hObj,'String')));
end

function heightCB(hObj,event)
    %global h;
    h=(str2num(get(hObj,'String')));
end

function genpattern(hObj,event)
    zeta1=sqrt(j*w*mu0/(sigma1+j*w*epsilon1));
    zeta2=sqrt(j*w*mu0/(sigma2+j*w*epsilon2));

    k1=w*mu0/(zeta1); %wave numbers
    k2=w*mu0/(zeta2);
    %n=sqrt(epsilon2/epsilon1); %index of refraction
    n=k2/k1;

    %air hemisphere
    theta1=0:thetares:pi/2-1e-5; %avoid theta=pi/2, because there is a
singularity
    phi1=0:phires:2*pi;
    [theta1,phi1]=meshgrid(theta1,phi1);
    %dielectric hemisphere
    theta2=pi/2+1e-5:thetares:pi;
    phi2=0:phires:2*pi;
    [theta2,phi2]=meshgrid(theta2,phi2);

    %% Field components
    %horizontal magnetic dipole
    ndiff1=sqrt(n^2-sin(theta1).^2);
    ndiff2=sqrt(1-n^2*sin(theta2).^2);

    Rpar=(n^2*abs(cos(theta1))-ndiff1)./(n^2*abs(cos(theta1))+ndiff1);
    Tpar=2./(abs(cos(theta2))+ndiff2);
    Rperp=(abs(cos(theta1))-ndiff1)./(abs(cos(theta1))+ndiff1);

```

```

Tperp=2*ndiff2./(n*abs(cos(theta2))+ndiff2);

heightterm=exp(-abs(real(-j*k1*h*ndiff2))+j*imag(-j*k1*h*ndiff2));

E_theta_hor1=w*mu0*m*k1*cos(phi1).*exp(j*k1*h*abs(cos(theta1)))*(exp(-
j*k1*r)/(4*pi*r)).*(1+Rpar.*exp(-j*2*k1*h*abs(cos(theta1)))));

E_theta_hor2=w*mu0*m*k1*cos(phi2).*abs(cos(theta2)).*heightterm.*Tpar.*(exp(-
j*k2*r)/(4*pi*r));

E_phi_hor1=w*mu0*m*k1.*sin(phi1).*abs(cos(theta1)).*exp(j*k1*h*abs(cos(theta1
))).*(exp(-j*k1*r)/(4*pi*r)).*(1-Rperp);
E_phi_hor2=-
w*mu0*k1*n*m*sin(phi2).*abs(cos(theta2)).*Tperp.*heightterm.*(exp(-
j*k2*r)/(4*pi*r));

%vertical magnetic dipole
Tpar=(cos(theta1)-ndiff1)/(cos(theta1)+ndiff1);
Tperp=2*n./(n*abs(cos(theta2))+ndiff2);

E_theta_ver1=zeros(size(theta1));
E_theta_ver2=zeros(size(theta2));

E_phi_ver1=w*mu0*m*k1*sin(theta1).*(exp(j*k1*h*cos(theta1))+Tpar.*exp(-
j*k1*h*cos(theta1))).*(exp(-j*k1*r)/(4*pi*r));
E_phi_ver2=-
w*mu0*k1*m*n*sin(theta2).*abs(cos(theta2)).*Tperp.*heightterm.*(exp(-
j*k2*r)/(4*pi*r));

%combined with 90 degree offset
E_theta_com1=E_theta_hor1+E_theta_ver1*phaseoff;
E_theta_com2=E_theta_hor2+E_theta_ver1*phaseoff;

E_phi_com1=E_phi_hor1+E_phi_ver1*phaseoff;
E_phi_com2=E_phi_hor2+E_phi_ver2*phaseoff;

%% Calculate Directivity

[D1_hor,D2_hor,Prad1_hor,Prad2_hor]=directivity(r,k1,k2,zeta1,zeta2,theta1,th
eta2,phi1,phi2,...
E_theta_hor1,E_theta_hor2,E_phi_hor1,E_phi_hor2);

[D1_ver,D2_ver,Prad1_ver,Prad2_ver]=directivity(r,k1,k2,zeta1,zeta2,theta1,th
eta2,phi1,phi2,...
E_theta_ver1,E_theta_ver2,E_phi_ver1,E_phi_ver2);

```



```

[D1_com,D2_com,Prad1_com,Prad2_com]=directivity(r,k1,k2,zeta1,zeta2,theta1,th
eta2,phi1,phi2,...
    E_theta_com1,E_theta_com2,E_phi_com1,E_phi_com2);

%% Generate Plots
%put back pi/2 for plotting purposes
theta1(:,end)=pi/2;
theta2(:,1)=pi/2;

if plotflag==1
    fontsize=12;
    % Directivity for the Horiztonal Magnetic Dipole
    axes(horaxis)
    cla
    plotqty1=10*log10(D1_hor);
    plotqty2=10*log10(D2_hor);

    %set limits

    plotqty1(plotqty1>uplim)=uplim;
    plotqty2(plotqty2>uplim)=uplim;
    %uplim=max(max(max(plotqty1,plotqty2)));
    plotqty1(plotqty1<lowlim)=lowlim;
    plotqty2(plotqty2<lowlim)=lowlim;

    [x,y,z]=sph2cart(phi1,pi/2-theta1,plotqty1+abs(lowlim));
    surf(x,y,-z,plotqty1,'FaceColor','interp','EdgeColor','none')
    hold on
    [x,y,z]=sph2cart(phi2,pi/2-theta2,plotqty2+abs(lowlim));
    surf(x,y,-z,plotqty2,'FaceColor','interp','EdgeColor','none')
    %make a transparent cube to represent the dielectric
    verts=[-1 -1 0; -1 1 0; 1 1 0; 1 -1 0; -1 -1 1; -1 1 1; 1 1 1; 1
-1 1]*(uplim+abs(lowlim));
    faces=[1 2 3 4; 2 6 7 3; 4 3 7 8; 1 5 8 4; 1 2 6 5; 5 6 7 8];
    patch('Vertices', verts, 'Faces',
faces,'FaceAlpha',0.1,'FaceColor','y');
    hold off
    axis([- (uplim+abs(lowlim)),uplim+abs(lowlim),-
(uplim+abs(lowlim)),uplim+abs(lowlim),...
- (uplim+abs(lowlim)),uplim+abs(lowlim),lowlim,uplim])
    view(82, 8)
    %title('Horiztonal Magnetic Dipole','fontsize',fontsize)
    set(horaxis,'XtickLabel',[],'YtickLabel',[],'ZtickLabel',[])
    %colorbar
    %coordinate system

    line([0,uplim+abs(lowlim)],[0,0],[0,0],'LineWidth',3,'color','g','Marker','>'
,'MarkerSize',10)

    line([0,0],[0,uplim+abs(lowlim)],[0,0],'LineWidth',3,'color','b','Marker','>'
,'MarkerSize',10)

    line([0,0],[0,0],[0,uplim+abs(lowlim)],'LineWidth',3,'color','r','Marker','^'
,'MarkerSize',10)

```

```

%axis equal;

% Directivity for the Vertical Magnetic Dipole
axes(veraxis)
cla
plotqty1=10*log10(D1_ver);
plotqty2=10*log10(D2_ver);

%set limits
plotqty1(plotqty1>uplim)=uplim;
plotqty2(plotqty2>uplim)=uplim;
%uplim=max(max(max(plotqty1,plotqty2)));
plotqty1(plotqty1<lowlim)=lowlim;
plotqty2(plotqty2<lowlim)=lowlim;

[x,y,z]=sph2cart(phi1,pi/2-theta1,plotqty1+abs(lowlim));
surf(x,y,-z,plotqty1,'FaceColor','interp','EdgeColor','none')
hold on
[x,y,z]=sph2cart(phi2,pi/2-theta2,plotqty2+abs(lowlim));
surf(x,y,-z,plotqty2,'FaceColor','interp','EdgeColor','none')
%make a transparent cube to represent the dielectric
verts=[-1 -1 0; -1 1 0; 1 1 0; 1 -1 0; -1 -1 1; -1 1 1; 1 1 1; 1
-1 1]*(uplim+abs(lowlim));
faces=[1 2 3 4; 2 6 7 3; 4 3 7 8; 1 5 8 4; 1 2 6 5; 5 6 7 8];
patch('Vertices', verts, 'Faces',
faces, 'FaceAlpha',0.1, 'FaceColor','y');
hold off
axis([- (uplim+abs(lowlim)),uplim+abs(lowlim),-
(uplim+abs(lowlim)),uplim+abs(lowlim),...
- (uplim+abs(lowlim)),uplim+abs(lowlim),lowlim,uplim])
view(82, 8)
%title('Vertical Magnetic Dipole','fontsize',fontsize)
set(veraxis, 'XtickLabel', [], 'YtickLabel', [], 'ZtickLabel', [])
%colorbar

line([0,uplim+abs(lowlim)],[0,0],[0,0], 'LineWidth',3, 'color','g', 'Marker','>'
, 'MarkerSize',10)

line([0,0],[0,uplim+abs(lowlim)],[0,0], 'LineWidth',3, 'color','b', 'Marker','>'
, 'MarkerSize',10)

line([0,0],[0,0],[0,uplim+abs(lowlim)], 'LineWidth',3, 'color','r', 'Marker','^'
, 'MarkerSize',10)

% Directivity for Cross Coils
axes(comaxis)
cla
plotqty1=10*log10(D1_com);
plotqty2=10*log10(D2_com);

%set limits
plotqty1(plotqty1>uplim)=uplim;
plotqty2(plotqty2>uplim)=uplim;
%uplim=max(max(max(plotqty1,plotqty2)));
plotqty1(plotqty1<lowlim)=lowlim;

```

```

plotqty2(plotqty2<lowlim)=lowlim;

[x,y,z]=sph2cart(phi1,pi/2-theta1,plotqty1+abs(lowlim));
surf(x,y,-z,plotqty1,'FaceColor','interp','EdgeColor','none')
hold on
[x,y,z]=sph2cart(phi2,pi/2-theta2,plotqty2+abs(lowlim));
surf(x,y,-z,plotqty2,'FaceColor','interp','EdgeColor','none')
%make a transparent cube to represent the dielectric
verts=[-1 -1 0; -1 1 0; 1 1 0; 1 -1 0; -1 -1 1; -1 1 1; 1 1 1; 1
-1 1]*(uplim+abs(lowlim));
faces=[1 2 3 4; 2 6 7 3; 4 3 7 8; 1 5 8 4; 1 2 6 5; 5 6 7 8];
patch('Vertices', verts, 'Faces',
faces,'FaceAlpha',0.1,'FaceColor','y');
hold off
axis([-uplim+abs(lowlim),uplim+abs(lowlim),-
(uplim+abs(lowlim)),uplim+abs(lowlim),...
-(uplim+abs(lowlim)),uplim+abs(lowlim),lowlim,uplim])
view(82, 8)
%title('Orthogonal Magnetic Dipoles','fontsize',fontsize)
set(comaxis,'XtickLabel',[],'YtickLabel',[],'ZtickLabel',[])
%colorbar

line([0,uplim+abs(lowlim)],[0,0],[0,0],'LineWidth',3,'color','g','Marker','>',
'MarkerSize',10)

line([0,0],[0,uplim+abs(lowlim)],[0,0],'LineWidth',3,'color','b','Marker','>',
'MarkerSize',10)

line([0,0],[0,0],[0,uplim+abs(lowlim)'],'LineWidth',3,'color','r','Marker','^',
'MarkerSize',10)
    %axis equal;
end

%% Find the maximum directivity and where it occurs
%Horiztonal Dipole
plotqty1=D1_hor;
plotqty2=D2_hor;
MaxD=max(max(max(plotqty2,plotqty1)));
ind=find(plotqty1==MaxD,1);
if isempty(ind)
    ind=find(plotqty2==MaxD,1);
    thetnum=floor(ind/size(plotqty2,1))+1;
    phinum=mod(ind,size(plotqty2,1))+1;
    bestthet=theta2(1,thetnum)*180/pi;
    bestphi=phi2(thetnum,1)*180/pi;
else
    thetnum=floor(ind/size(plotqty1,1))+1;
    phinum=mod(ind,size(plotqty1,1))+1;
    bestthet=theta1(1,thetnum)*180/pi;
    bestphi=phi1(thetnum,1)*180/pi;
end
%state the Max directivity and ratio of radiated power
disp('Horiztonal Dipole')
fprintf('Max Directivity = %.2f dB @\ntheta = %.2f deg,\nphi = %.2f
deg \n',10*log10(MaxD),bestthet,bestphi)

```

```

        fprintf('\nRatio of radiated power in medium 2 / medium 1 = %.2f \n\n', Prad2_hor/Prad1_hor)

        %save these messages for the gui
        set(handles.texthor1, 'string', sprintf('Max Directivity = %.2f dB', 10*log10(MaxD)));
        set(handles.texthor2, 'string', sprintf('@ theta = %.2f deg, phi = %.2f deg', bestthet, bestphi));
        set(handles.texthor3, 'string', sprintf('Ratio of radiated power in medium 2 / medium 1 = %.2f', Prad2_hor/Prad1_hor));

        %Vertical Dipole
        plotqty1=D1_ver;
        plotqty2=D2_ver;
        MaxD=max(max(max(plotqty2, plotqty1)));
        ind=find(plotqty1==MaxD, 1);
        if isempty(ind)
            ind=find(plotqty2==MaxD, 1);
            thetnum=floor(ind/size(plotqty2, 1))+1;
            phinum=mod(ind, size(plotqty2, 1))+1;
            bestthet=theta2(1, thetnum)*180/pi;
            bestphi=phi2(thetnum, 1)*180/pi;
        else
            thetnum=floor(ind/size(plotqty1, 1))+1;
            phinum=mod(ind, size(plotqty1, 1))+1;
            bestthet=theta1(1, thetnum)*180/pi;
            bestphi=phi1(thetnum, 1)*180/pi;
        end
        disp('Vertical Dipole')
        fprintf('Max Directivity = %.2f dB @\ntheta = %.2f deg, \nphi = %.2f deg \n', 10*log10(MaxD), bestthet, bestphi)
        fprintf('\nRatio of radiated power in medium 2 / medium 1 = %.2f \n\n', Prad2_ver/Prad1_ver)

        %save these messages for the gui
        set(handles.textver1, 'string', sprintf('Max Directivity = %.2f dB', 10*log10(MaxD)));
        set(handles.textver2, 'string', sprintf('@ theta = %.2f deg, phi = %.2f deg', bestthet, bestphi));
        set(handles.textver3, 'string', sprintf('Ratio of radiated power in medium 2 / medium 1 = %.2f', Prad2_ver/Prad1_ver));

        %Cross Coils
        plotqty1=D1_com;
        plotqty2=D2_com;
        MaxD=max(max(max(plotqty2, plotqty1)));
        ind=find(plotqty1==MaxD, 1);
        if isempty(ind)
            ind=find(plotqty2==MaxD, 1);
            thetnum=floor(ind/size(plotqty2, 1))+1;
            phinum=mod(ind, size(plotqty2, 1))+1;
            bestthet=theta2(1, thetnum)*180/pi;
            bestphi=phi2(thetnum, 1)*180/pi;
        else
            thetnum=floor(ind/size(plotqty1, 1))+1;

```

```

        phinum=mod(ind,size(plotqty1,1))+1;
        bestthet=thetal(1,thetnum)*180/pi;
        bestphi=phil(thetnum,1)*180/pi;
    end
    %state the Max directivity and ratio of radiated power
    disp('Cross Coils')
    fprintf('Max Directivity = %.2f dB @\ntheta = %.2f deg,\nphi = %.2f
deg \n',10*log10(MaxD),bestthet,bestphi)
    fprintf('\nRatio of radiated power in medium 2 / medium 1 = %.2f \n
\n',Prad2_com/Prad1_com)

    %save these messages for the gui
    set(handles.textcom1,'string',sprintf('Max Directivity = %.2f
dB',10*log10(MaxD)));
    set(handles.textcom2,'string',sprintf('@ theta = %.2f deg, phi =
%.2f deg',bestthet,bestphi));
    set(handles.textcom3,'string',sprintf('Ratio of radiated power in
medium 2 / medium 1 = %.2f',Prad2_com/Prad1_com));
end

end

function [ D1,D2,Prad1,Prad2 ] =
directivity(r,k1,k2,zeta1,zeta2,thetal,theta2,phil,phi2,E_thetal, E_theta2,
E_phil, E_phi2)
%directivity Finds the directivity in spherical coordinates
% This function was intended for calculated the fields above horizontal
% and vertical dipoles from the far-fields. It expects two regions: a top
% and lower region with corresponding theta and phi coordinates.

%r=1;
%radiation intensity:
U1=(real(zeta1)/(2*(abs(zeta1).^2)))*((abs(E_thetal.*exp(j*k1*r)*r).^2)+...
(abs(E_phil.*exp(j*k1*r)*r).^2));

U2=(real(zeta2)/(2*(abs(zeta2).^2)))*((abs(E_theta2.*exp(j*k2*r)*r).^2)+...
(abs(E_phi2.*exp(j*k2*r)*r).^2));

%total power radiated
Prad1=trapz(thetal(1,:),trapz(phil(:,1),sin(thetal).*U1));
Prad2=trapz(theta2(1,:),trapz(phi2(:,1),sin(theta2).*U2));

Prad=Prad1+Prad2;

%directivity
D1=4*pi*U1/Prad;
D2=4*pi*U2/Prad;

end

```